12-2022

The role of MRI in diagnosing autism: a machine learning perspective.

Yaser AbdelRahman ElNakieb
University of Louisville

Recommended Citation

THE ROLE OF MRI IN DIAGNOSING AUTISM: A MACHINE LEARNING PERSPECTIVE

By

Yaser AbdelRahman ElNakieb
B.S. in ECE, 2011

A Dissertation
Submitted to the Graduate School of the
University of Louisville
in Partial Fulfillment of the Requirements
for the Degree of

Doctor of Philosophy
in Interdisciplinary Studies: Specialization in Translational
Bioengineering

Interdisciplinary Studies
University of Louisville
Louisville, Kentucky

December 2022

THE ROLE OF MRI IN DIAGNOSING AUTISM: A MACHINE LEARNING
PERSPECTIVE

By

Yaser AbdelRahman ElNakieb
B.S. in ECE, 2011

Dissertation approved on

November 29, 2022

by the following dissertation Committee:

_____

Dissertation Director
Ayman S. El-Baz, Ph.D.

_____

Guruprasad Giridharan, Ph.D.

_____

Jonathan Kopechek, Ph.D.

_____

Tamer M. A. Mohamed, Ph.D.

_____

Gregory Neal Barnes, M.D., Ph.D.

DEDICATION

To the educator, the researcher, the scientist, the role model, my guide, and my motivator: to the soul of my father, Dr. Abdel Rahman Abdel Rahman ElNakib.

ACKNOWLEDGMENTS

ABSTRACT

THE ROLE OF MRI IN DIAGNOSING AUTISM: A MACHINE LEARNING

PERSPECTIVE

Yaser AbdelRahman ElNakieb

November 29, 2022

There is approximately 1 in every 44 children in the United States suffers from autism spectrum disorder (ASD), a disorder characterized by social and behavioral impairments. Communication difficulties, interpersonal difficulties, and behavioral difficulties are the top common symptoms. Even though symptoms can begin as early as infancy, it may take multiple visits to a pediatric specialist before an accurate diagnosis can be made. In addition, the diagnosis can be subjective, and different specialists may give different scores. There is a growing body of research suggesting differences in brain development and/or environmental and/or genetic factors contribute to autism development, but scientists have yet to identify exactly the pathology of this disorder. ASD can currently be diagnosed by a set of diagnostic evaluations, regarded as the gold standard, such as the Autism Diagnostic Observation Schedule (ADOS) or the Autism Diagnostic Interview-Revised (ADI-R). A team of qualified clinicians is needed for performing the behavioral and communication tests as well as clinical history information, hence a considerable amount of time, effort, and subjective judgment is involved in using these gold-standard diagnostic instruments. In addition to standard observational assessment, recent advancements in neuroimaging and machine learning suggest a rapid and objective alternative, using brain imaging. An investigation of the employment of different imaging modalities, namely Diffusion Tensor Imaging (DTI), and resting state functional MRI (rs-fMRI) for autism

diagnosis is presented in this comprehensive work. A detailed study of the implementation of feature engineering tools to find discriminant insights from different brain imaging modalities, including the use of novel feature representations, and the use of a machine learning framework to assist in the accurate classification of autistic individuals is introduced in this dissertation. Based on three large publicly available datasets, this extensive research highlights different decisions along the pipeline and their impact on diagnostic accuracy. It also identifies potentially impacted brain regions that contribute to an autism diagnosis. Achieving high global state-of-the-art cross-validated accuracy confirms the benefits of feature representation and feature engineering in extracting useful information, as well as the potential benefits of utilizing neuroimaging in the diagnosis of autism. This should enable an early, automated, and more objective personalized diagnosis.

TABLE OF CONTENTS

LIST OF TABLES

LIST OF FIGURES

CHAPTER I

INTRODUCTION

Autism spectrum disorder (ASD), famously known as just autism, is a pervasive neurodevelopmental disorder manifested as three primary characteristics: functioning difficulties with social interaction, communication barriers, and behavioral restrictions and repetitive patterns [1–4]. According to a recent statistic reported by the Centers for Disease Control and Prevention (CDC) in 2021, 1 in 44 U.S. children were diagnosed with autism in 2018. This is a 127% increase from the numbers in 2016, a 155% increase from the numbers in 2010, and a 241% increase since 2000. Figure 1 shows the increase in reported numbers in the US. The annual expenditure, including direct medical and non-medical costs, of autism in 2015 was 265 billion dollars. Those numbers are forecast to increase to 461 billion in 2025 [5]. Identification of co-occurring conditions at the earliest possible stage could lead to better services and earlier interventions that are beneficial to children with ASD.

Despite the lack of a comprehensive understanding of ASD causes, numerous hypotheses and theories have been proposed concerning the etiology of its underlying mechanism. These hypotheses and theories suggest that genes and environmental factors play a significant role in determining ASD's severity [6]. Anatomical abnormalities of the brain [7], functioning of the brain during rest or while performing different tasks [8], or abnormal connectivity of the white matter [9, 10] are hypothesized to be responsible for ASD symptoms.

In order to study different types of abnormalities correlated with ASD, several magnetic resonance imaging (MRI) based modalities have been used, such as: (i) structural MRI (sMRI) for studying anatomical features, (ii) functional MRI (fMRI), either at rest or while performing a task, for studying brain activities, and (iii) diffusion tensor imaging (DTI) for studying brain connectivity.

Autistic symptoms usually begin to develop within the first two years of life. Early ASD manifestations could be found in 12-month infants. However, the average age for diagnosis is around five years [11], [12]. The current gold standard in ASD diagnosis is based on behavior observational tests by clinicians such as the Autism Diagnostic Observation Schedule (ADOS) [13], Autism Diagnostic Interview-Revised (ADI-R) report [14], or Social Responsiveness Scale (SRS), but these approaches usually requires time, training, and can be subjective.

1   Current Autism Diagnosis Techniques

A variety of tests are used by evaluators to determine if young children with possible symptoms of autism are on the autism spectrum, including checklists, observations, interactive tests, and interview questions. Currently approved diagnosis techniques require significant clinical experience, assessing different aspects via a standard
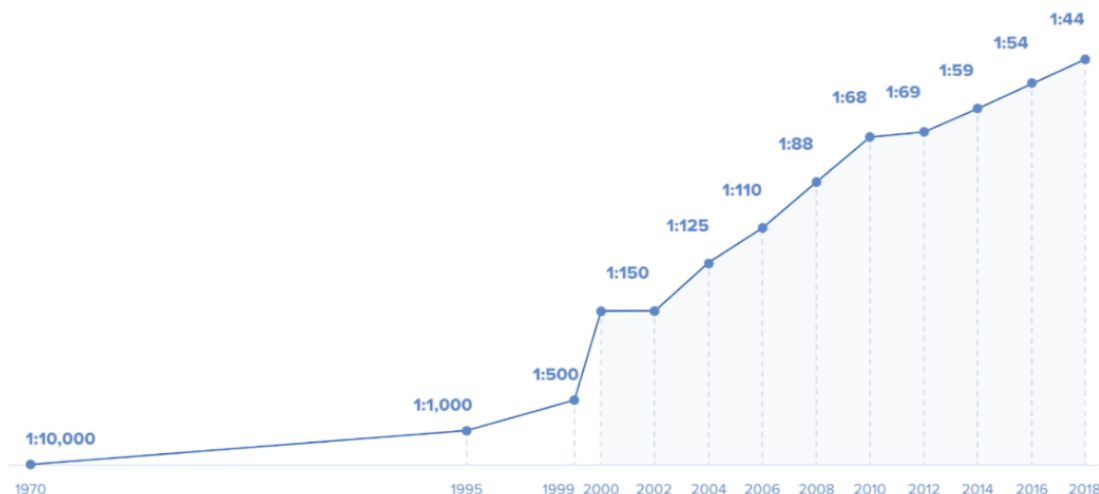
Figure 1. Increase in prevalence in U.S. children diagnosed with autism per surveillance year (horizontal axis).

testing/scoring system, such as the Autism Diagnostic Observation Scale (ADOS), Autism Diagnostic Interview—Revised (ADI-R), Social Receptivity Scale (SRS), Calibrated Severity Scores (CSS), Childhood Autism Rating Scale (CARS), and many others. We introduce the top three diagnostic tools, where the first two are considered the 'gold standard'.

ADOS

The Autism Diagnostic Observation Scale (ADOS) is a standardized diagnostic tool used to determine whether an individual with ASD exhibits social, imaginative, and communication difficulties. As the most prominent indicator of ASD, it focuses on social and communication deficits. Five different ADOS modules exist, depending on the age of the patient, each focusing on a set of tasks specific to this age group. Each module scores a different number of tasks, where individuals suspected of having ASD should undergo standardized assessments of social interaction, play, and imaginative use of materials. The main drawback is that the individual who administers and scores the test must receive special training.

ADI-R

Autism Genetic Research Exchange describes the ADI-R as a parent interview that involves ninety-three items, focusing on the behavior in three domains: social interactions, communication and language, and repetitive behaviors. Additionally, the measure includes other items of relevance to treatment planning, including self-injury and overactivity. The report is basically dependent on the parents' responses rather than direct interactions, and scores are given to each of the three categories. When a child meets or exceeds the specified cutoffs in all three content areas of communi-

cation, social interaction, and patterns of behavior, and the disorder has manifested by 36 months of age, a diagnosis of autism is made.

SRS

The Social Receptivity Scale (SRS) measures the severity of social deficits and symptoms associated with ASD based on a respondent survey. It was designed specifically for use by parents and teachers, after quick training, in 15–20 minutes. Using a quantitative approach, autistic symptoms are measured across the full range of severity that occurs in nature, using a 65-item rating scale, giving an initial rating that works as an indication.

Limitations of Current Techniques

Despite the fact that there is no medical test for autism, evaluators rely on observations, answers from parents, and tests designed to assess a child's skills and behaviors across several developmental domains. Those tests are subjective, can be time-consuming and challenging, with limited accuracy around 80%-85% [15], and clinicians may not always agree with the results of those tests because of some grading biases [16].

A variety of metrics is used to measure autism severity, illustrating the ongoing efforts of clinicians and researchers to identify valid metrics for capturing the severity construct for ASD. As of right now, the gold standard for diagnosing autism spectrum disorders is to conduct a behavioral observational test by a clinician; however, this testing is subjective, time-consuming, and only provides late detection (the child must be at least two years old in order to submit a report).

The levels of autism severity are highly correlated with age, cognitive abilities, and/or language abilities [17]. In light of these correlations, it appears that many measures reflect the developmental characteristics of children, rather than inherent autistic traits, questioning the validity of those measures.

Thus, this is our main **motivation** for developing a neuroimaging-based quantitative objective alternative that can provide a least-subjective evaluation that may help clinicians reach a faster, more reliable diagnosis.

2   Objectives

The main objectives of this dissertation are:

- Present promising ML framework of autism diagnosis, tested on different publicly available datasets: ABIDE, ABIDE-II, and NDAR

- Develop a unified perspective for solving autism diagnosis using different imaging modalities: DTI and fMRI

- Provides a comprehensive overview of different choices along the ML pipeline, filling an important gap in knowledge for the next researchers

- Develop an ML algorithm that preserves feature semantics and is reproducible and scalable

In the next subsections, we will present the main imaging modalities and used tools in the course of the dissertation.

3   Brain Imaging in Autism Diagnosis

A key advantage of MRI is that it offers the best comparison of soft tissue between all image modalities. Therefore, MRI is considered to be the most powerful noninvasive clinical diagnostic tool and the most useful modality for imaging the brain. MRI is an essential non-invasive method in the detection of brain structure, White Matter (WM) integrity, and functional activity [18]. sMRI has been used to describe the morphological brain changes in ASD regarding the shape and volume of different brain regions. DTI provides an assessment of anatomical connections and has shown disorganized micro-structural WM integrity in the autistic population. fMRI relies on the detection of dynamic physiological information from active brain regions. Measuring the change of Blood Oxygenation Level-Dependent (BOLD) signal in various brain states (resting state or task-evoked) can reveal functional architecture abnormalities in the ASD population [19], [20]. The following subsections highlight the differences between the three main MRI modalities.

Structural MRI (sMRI)

sMRI is the most commonly used MRI in any non-research medical setting. When MRI is referenced without a specification, usually sMRI is the one meant. There are several advantages to using MRI for the imaging of the brain, spinal cord, and vascular anatomy; the most important of these is that it is capable of providing exquisite detail of the brain, spinal cord, and vascular anatomy in all three planes, see Figure 2. The relaxation time of tissue can be divided into two categories, T1 and T2. The longitudinal relaxation time (T1) determines the rate at which excited protons return to equilibrium, while the transverse relaxation time (T2) is the time constant that determines how quickly excited protons reach equilibrium or fall out of phase with each other. Accordingly, depending on the selection of the time to echo (TE) and the repetition time (TR), we have can get two types of MRI scans: T1-weighted and T2-weighted MRI. A short TE time and TR time are used in order to produce T1-weighted images, while T2-weighted images are obtained by using longer TE and TR. Each type weighs a different characteristic of the tissue (T1 / T2). sMRI reveals anatomical information of each tissue type, differentiating gray matter (GM), WM, cerebrospinal fluid (CSF), and other structures. The output features are usually shape and morphological and geometric features, such as cortical thickness, surface area, volume, and curvature measures.
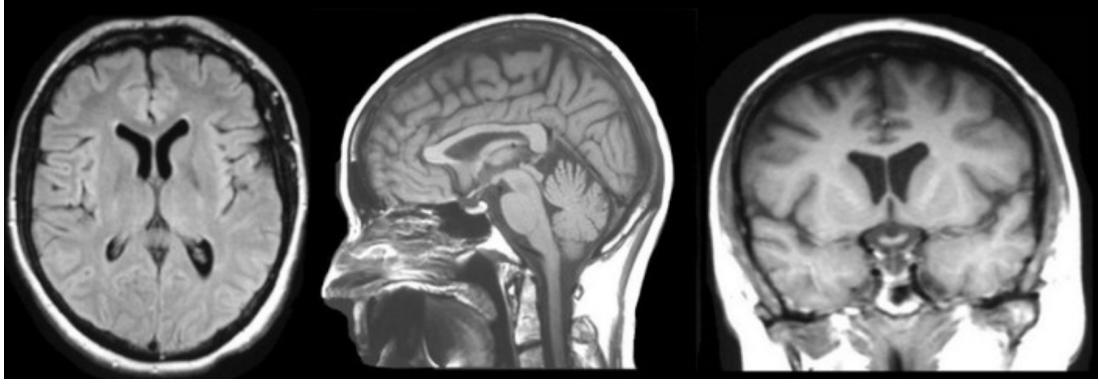
Figure 2. An example of sMRI of the head, showing brain anatomical details in the three planes: axial, sagittal, and coronal.

Functional MRI (fMRI)

fMRI is a technique for studying the activation of brain regions in response to certain stressors as well as identifying brain hemodynamic changes corresponding to changes in mental activity. Using functional imaging, it is possible to identify areas of the brain and the underlying processes that enable a particular cognitive or behavioral function to be performed. It is possible to make inferences about brain function and location based on the type of signal being analyzed. There is still a long way to go before fMRI is widely used in clinical practice.

Functional MRI uses a measure of BOLD signals based on the fact that the greater the metabolic demand of a particular area of the brain while performing a given task, the harder that area works. As metabolic function increases, vessels in a particular brain region may dilate (expand), resulting in greater oxygenated blood flow and a shift in the gradient between highly oxygenated and highly deoxygenated hemoglobin in the capillaries. The scanner is capable of detecting regional changes in this signal since different oxygen levels can be decoded via fMRI. In this way, we can indirectly measure brain activity based on the physiological changes that occur within the brain. This enables researchers to match various spotted neuronal activities with BOLD signals, and invasively learn how the brain is functioning.

Diffusion Tensor Imaging (DTI)

DTI is a non-invasive in-vivo tool based on the measurement of the Brownian motion/ diffusion of water molecules within WM tracts, thus providing a macroscopic picture of WM structure within the imaged voxel. Magnetic gradients in at least 6 non-colinear directions, in addition to a base volume, are used as input for proper DTI construction. As a result, a 3x3 diffusion tensor matrix can be calculated at each voxel, with each element representing diffusion across one direction (xx/ xy/ ... etc.)

$$D = \begin{bmatrix} D_{x,x} & D_{x,y} & D_{x,z} \\ D_{y,x} & D_{y,y} & D_{y,z} \\ D_{z,x} & D_{z,y} & D_{z,z} \end{bmatrix}$$

5

(a) Tensor eigenvectors   (b) Tensor eigenvalues
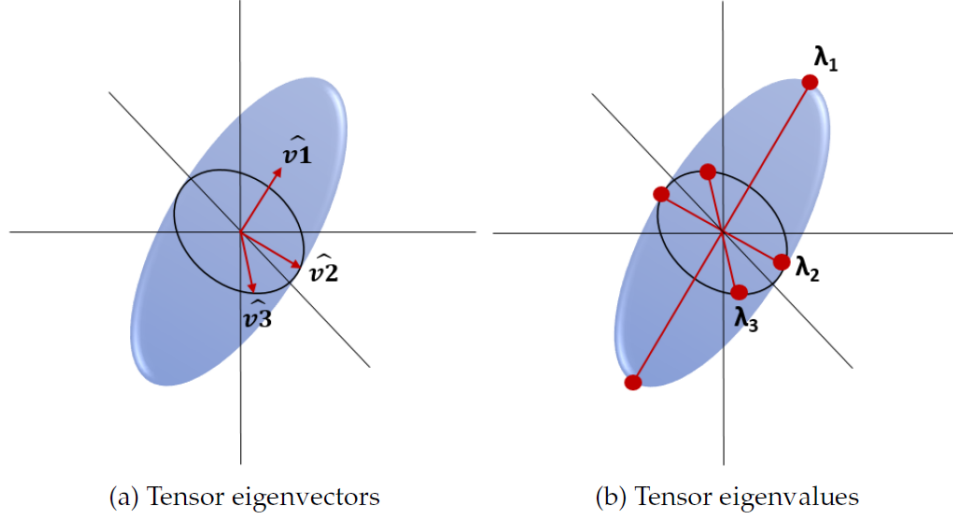
Figure 3. Graphical representation of diffusion tensor using the ellipsoid model using three eigenvectors that define the orientation of the ellipsoid in 3D, and three eigenvalues that define the principal axes values of the ellipsoid.

To find the principal diffusion directions and strength, the 3 eigenvalues λ_1, λ_2 and λ_3 and their corresponding eigenvectors v_1, v_2 and v_3 are calculated, where the eigenvector corresponding to the largest eigenvalue is the principle diffusion direction (i.e, diffusion in across the fiber), while the other two eigenvectors correspond to the radial diffusion directions (i.e, diffusion perpendicular to the fiber) [21]. A special case is an isotropic medium, where the diffusion ellipsoid takes the shape of a sphere because $\lambda_1 = \lambda_2 = \lambda_3$. While in the case of an anisotropic medium, the diffusion is represented as an ellipsoid as shown pointing in the v_1 direction with λ_1. Figure 3 illustrates the resulting representation. In addition, another representation is DTI tractography, where major tracts or bundles from a region of interest (ROI) can be tracked, and 3D color-coded maps can be visualized, with each color representing a different direction (x / y / z) of fiber crossing, see Figure 4. The most important DTI metrics are Mean Diffusivity (MD) and Fractional Anisotropy (FA). MD measures the overall amount of diffusion and is related to cellular density. FA captures the directional changes of diffusion and represents the degree of alignment of WM tracts and cellular structure, ranging from 0 (random or isotropic) to 1 (unidirectional or anisotropic). Other parameters include Axial Diffusivity (AD) and Radial Diffusivity (RD). AD measures the diffusion in a direction parallel to WM tracts and represents axon integrity, whereas RD is the perpendicular diffusion and is related to myelin integrity [22], [23], [24].

WM tracts are composed of bundles of axons that carry the communication signals between brain regions. Alteration in synaptogenesis was reported in the ASD population caused by dysmaturation of myelination. Myelin alteration leads to changes in axonal fiber density, caliber, and homogeneity with subsequent impairment of WM microstructural organization and integrity [25], [26], [20].
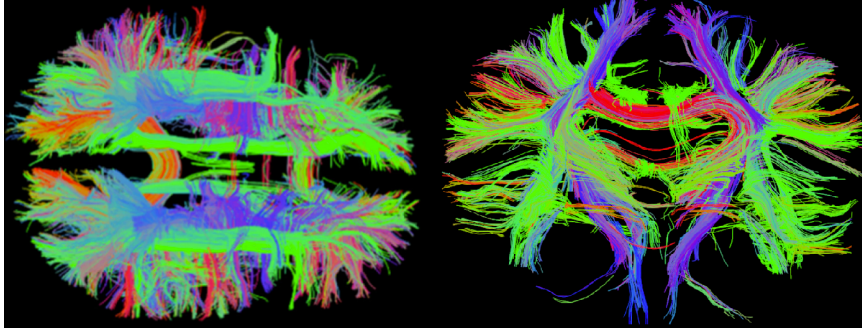
Figure 4. An example of DTI tractography of the WM tracts.

4 Computer Aided Diagnosis (CAD) using Machine Learning (ML)

Early and appropriate diagnosis is crucial to help limit the deterioration of the condition, and to improve prognostic outcomes [27], [28], [29]. Computer-aided algorithms are introduced to help clinicians reach early better diagnoses. A CAD usually consists of three major stages: feature extraction, feature reduction, and classification. Feature extraction is closely related to the type of medical data uses, for each data modality there exists different feature extraction methods, and different data representations. After the appropriate data representation and feature extraction, which is a crucial step, many improvements and algorithms still exist for feature reduction and machine learning parts. The next subsection will introduce the basic notions and types of both feature reduction and machine learning stages.

Dimensionality Reduction: importance and techniques

Due to the high dimensionality of the feature space in medical CAD systems, a major component of any ML algorithm is the provision of the appropriate reduction technique. Bellman [30] introduced the term 'curse of dimensionality to describe the problem of exponential complexity resulting from the addition of new dimensions to feature space, commonly defined as $p >> n$ problem. MRI imaging research and medical data are commonly affected by this phenomenon, with extremely huge feature space, which may result in over-fitting. There are several ways to reduce the number of features, such as principal component analysis (PCA), linear discriminant analysis (LDA), or autoencoders [31–33]. Due to the fact that these methods do not preserve the semantics of the original feature space, it is typically difficult to identify what clinical findings underlie such classification results. This, in turn, makes them less useful for actual use by physicians to provide them with more information or to better understand the pathological abnormalities underlying each autistic brain, and thus are less attractive and less practical.

Several methods are introduced for efficient feature selection, rather than feature reduction, and most of them incorporate filtering techniques. In the following subsections, we will introduce some of the feature selections used in this dissertation.

Kernel F-score feature selection is a simple univariate filtering method, that uses F-score, to select a subset of features. The scoring function is calculated using

7

one-way ANOVA F-test, which returns an array of scores, one for each feature $X[:, i]$ of the input X. Based on this FS algorithm, the first K features with the highest scores in X are retained. The significance of a large score indicates that there is no equality in the means of the K groups, suggesting providing 'distinctive' information. F-score can be measured as the ratio between the "between group variance" to the "within group variance".

$$F = \frac{between\ group\ variance}{within\ group\ variance}$$

The use of F-score values for medical datasets with high dimensional feature space was validated to be of beneficial use [34].

Signal to noise (s2n) ratio filtering is another simple filtering method to select a subset of features [35]. S2n is a one-sided metric, that analyzes the difference between the desired signal (such as class labels) and the background noise for a particular feature. The concept of this ratio originated from electrical engineering, however, in the field of machine learning, it has been also applied to medical data [36, 37]. This approach ranks each feature according to a ratio of the absolute difference between the means of the two classes and their variances.

The metric is calculated as

$$s2n(X_i, Y) = \frac{abs(\mu(y_+) - \mu(y_-))}{var(y_+) + var(y_-)} \tag{1}$$

where X_i is the feature vector for each feature i in input X, and Y is class label, $\mu(y_+)$ is the mean value for class y_+ vectors, and $var(y_+)$ is the variance for this class.

Recursive feature elimination (RFE) is a popular feature reduction method that is based on ranking the set of features based on their importance. There is a distinction between ranking and selecting features; nevertheless, they are closely related, and sometimes one is accomplished by the other. It is often the case that the removal of lower-ranked features is followed by the ranking of features, such as by information gain, in the recursive feature selection process. The RFE method is designed to improve generalization performance by removing less important features that will have the least effect on training errors [38]. This is done by employing a classifier as a kernel, assigning weights to features (coefficients or feature importance of the model), ranking the features, and recursively eliminating a small number of features each step.

In the first step, the classifier is trained on the initial set of features (all) in order to establish their importance. After the current set of features has been pruned, the least important features are removed. Iteratively repeating this procedure on the pruned set leads to the ultimate selection of the desired number of features, or reaching the stopping number of features to keep. In the latter case, the number of features to be selected can be determined, instead of preset, based on the change in performance metric.

The performance of the RFE depends on the estimator (kernel) used for training at each step. Many kernels are used in literature, including the most commonly used

supported vector machine (SVM) [39]. Another common variant of the RFE is the RFE with cross-validation (RFE-CV), where the performance at each step is determined based on the cross-validated metric (accuracy, ...etc.) on testing subsets, where data splitting is done in a similar manner to k-fold cross validation. A major benefit of RFE-CV is avoiding over-fitting, in the price of requiring k-folds computations, which translates into more training time.

Machine learning (ML) techniques

ML is a field of knowledge that refers to the imitation of the way in which humans think and solve problems using artificial learning mechanisms. ML is a basic part of AI. During the process of ML, a large number of data points are presented to a machine in order to aid it in making predictions, finding patterns, or categorizing the data. There are three major types of ML: supervised, unsupervised, and reinforcement learning. Supervised learning refers to data classification based on supervision (i.e., through labeled input-output pairs; each pair contains an input associated with its desired ground truth output). Classification of a disease, with labels for training subset to train the model, and using labels of testing subset for evaluation, is an example of supervised learning. On the other hand, unsupervised learning does not depend on supervision (labeled input-output pairs) to perform data categorization. Instead, the patterns of the input data are used to efficiently categorize the data. The third type, reinforcement learning, gives a positive negative reward, instead of knowing the ultimate/ true labels. Learning by reinforcement is the most similar type of machine learning to how humans learn.

Classification, which is the focus of this work, is an example of supervised learning. The list of classifiers is so long, including SVM, random forests (RF), logistic regression (LR), artificial neural networks (ANN), and many others. On top of ML, deep learning has gained a lot of popularity and potential applications in several medical applications. The most popular deep learning networks are convolutional neural networks (CNNs). Unlike traditional neural networks, CNNs are composed of many convolutional and fully connected layers that perform both feature extraction and classification. CNNs outperform traditional algorithms when it comes to image recognition, yet it is computationally expensive and is usually hard to interpret.

Throughout this dissertation, various machine learning algorithms are utilized, and here we present the concepts of some of the used classifiers:

- K-Nearest Neighbor (KNN):
  KNN is a classification algorithm where data points are assigned to one of K groups based on their proximity to the nearest data points, in terms of some distance metric, which offers an indication of how likely it is that they will be assigned to that group. The parameter 'K' needs to be specified in advance, as well as the distance metric. This classifier is highly impacted by data preprocessing and normalization steps.

- Naïve Bayes:
  As the name suggests, Naive Bayes utilizes the Bayes theorem as well as a

posterior probability to determine the posterior likelihood, which is used to classify the unstructured data. This approach makes the naive assumption that the predictors are independent, which might not be the case.

- Logistic Regression (LR):
  In practical terms, LR is a regression model utilizing the powers of regression to do classification and has done so exceedingly well for several decades now, staying among the most popular models for a long time to come. It is highly utilized in medical applications since its ease of explainability, identifying the quantitative contributions of individual predictors.

- Random Forest (RF):
  Random forest is based on decision trees, applying an ensemble of multiple decision trees. Using fewer features on each individual tree, the trees are then built using bagging (i.e. combining multiple bootstrap datasets with replacement, which are nothing more than sampling records with replacement). This ensures a reduced variance, making it more generalizable to the new dataset. The main disadvantage is its sensitivity to outlier data, which can degrade the performance fast.

- Support Vector Machines (SVM):
  SVM is an increasingly popular classifier that is suitable for spaces with a high degree of dimensionality, particularly when the number of dimensions exceeds the number of samples. An SVM algorithm seeks to find a hyperplane in the N-dimensional feature space that distinguishes the data points in a distinct manner. The characteristics of finding such a hyperplane is greatly dependent on the choice of the SVM kernel, which is a special important function of the SVM. As a result of the kernel conversion, the experimental data set is transformed into a spatially higher dimensional space where the algorithm constructs a hyperplane dividing the data set into classes based on its spatial distribution.

- Passive Aggressive classifier:
  The algorithm is called as it involves two different mechanisms: 1) Passive: the model should be left in place if the prediction turned out to be accurate. Therefore, the data in the example are not sufficient to cause any changes to the model. 2) Aggressive: make changes to the model if the prediction is inaccurate. Hence, it may be possible to correct the model by making some changes.

- XGBoost:
  Extreme gradient boosting (XGBoost) is an open-source library that provides a framework for regularizing gradient boosting. A prediction score for XGBoost is calculated using gradient boosting, which is an ensemble learning approach that combines the outputs from several decision trees.

- Artificial Neural Networks (ANN):
  ANN, so named because they are designed to simulate the human brain, are suitable for large and complex datasets. The building blocks, nodes, similar

to neurons, are mapped together as multiple layers to the multiple inputs, in order to generate the target output. Each node can approximate any continuous function on its direct input. A first (random) mapping is performed; then, the related weights are iteratively self-adjusted to fine-tune to the appropriate output for all data points. NN is widely successful in computer vision, natural language processing, speech recognition, and many other applications.

Performance Measures

To measure the performance of ML components, different metrics are used to evaluate autism diagnosis. In the following, we will provide a brief overview of these metrics.

Let TP indicate true positive, TN indicate true negative, FN denotes false negative, and FP denotes false positive. The following performance metrics are defined as follows:

- Specificity: $\frac{TN}{FP+TN}$

- Sensitivity (recall): $\frac{TP}{TP+FN}$

- Accuracy: $\frac{TP+TN}{TP+TN+FP+FN}$

- F1-score: $\frac{2*Precision*Recall}{Precision+Recall} = \frac{2*TP}{2*TP+FP+FN}$

- Precision: $\frac{TP}{TP+FP}$

- AUC is the area under the curve of the receiver operating characteristics (ROC). AUC is between 0 and 1. The closer the AUC to 1, the better the performance.

5 Dissertation Organization

In this dissertation, six chapters are included. Below are some remarks that summarize the contents of each chapter:

Chapter II: This chapter reviews recent publications which utilize ML methods to help predict or identify ASD based on MRI data. The chapter reviews recent advancements toward an understanding of ASD using DTI and fMRI imaging modalities. This literature overview is helpful to stress the unique strengths of this dissertation work.

Chapter III: This chapter introduces an ML framework for autism diagnosis using DTI. The chapter introduces a new feature representation inspired by functional MRI. It also applies the proposed framework on NDAR, a publicly available dataset, to a study of 263 subjects. The main advantage of this dataset is that some subjects also have other imaging modalities and even genomics information.

Chapter IV: This chapter introduces an enhanced, more sophisticated version, of an ML framework for autism diagnosis using DTI. Tested on a newer publicly available dataset (ABIDE-II), it provides more detailed experiments, and the work was able to achieve better classification accuracy.

Chapter V: This chapter presents an ML framework based on resting-state fMRI for the autism diagnosis. The chapter provides a comprehensive experimentation

overview of different preprocessing strategies, the use of different atlases, and introduces a new feature representation, and compares it with the conventional representation.

Chapter VI concludes the work and outlines the future work.

CHAPTER II

AUTISM COMPUTER AIDED DIAGNOSIS: A SURVEY

The use of brain imaging, specifically magnetic resonance imaging (MRI), has proven capable of assisting in the fast, objective, and early identification of autism spectrum disorders. In recent years, Artificial Intelligence (AI) and Machine Learning (ML) tools have made significant advancements in both the diagnosis and early detection of autism spectrum disorder. The purpose of this chapter is to review the role of machine learning (ML) in the diagnosis and detection of autism using the two MRI modalities: Diffusion Tensor Imaging (DTI) and function magnetic resonance imaging (fMRI), that will be used in this dissertation. The survey also provides an overview of the major findings that correlate DTI and fMRI to autism phenotype. Based on the findings in this chapter, it should be clear that computer-aided diagnosis (CAD) is useful for early, subjective ASD detection and diagnosis. In the future, we expect that AI solutions will be used in healthcare settings. This study should pave the road towards such employment for ASD detection.

Although different MRI modalities have shown promise in distinguishing ASD individuals from healthy controls (typically developed, TD), MRI studies seem inconsistent and non-replicable [18]. The need for neuroimaging biomarkers remains an ongoing clinical challenge. Several CAD systems have been widely applied to integrate multimodal MRI with AI. ML is a subfield within AI. In neuroimaging, ML is widely used in medical image analysis through extracting informative features and constructing the best fitting algorithm to provide the desired output [12], [40]. The most frequently selected features for ASD include morphological features (shape, volume, texture), and spatial relationship features. These features are computed to study developmental brain abnormalities and can be applied to improve the diagnosis, classify subtypes, and degree of severity of ASD [41], [42].

The availability of large datasets, including those from the Autism Brain Imaging Data Exchange (ABIDE), led to an increase in publications combining ML with different neuroimaging biomarkers. These studies aim to reduce subjectivity and to establish a more objective data-driven method for identification, classification, and prognosis of ASD children [12].

In this chapter, we aimed to review the publications predicting or identifying ASD based on MRI using ML methods. DTI studies since 2011 will be presented. There is a great increase in the number of publications based on functional imaging (fMRI). Here, we will focus on recent fMRI studies in the last five years. Manual search is done using electronic databases in PubMed and Google Scholar for articles and papers published in English until July 2022, using search terms as follows: (autism or autism spectrum disorders or ASD) and (diffusion tensor imaging or DTI) AND (functional magnetic resonance imaging, fMRI, task-based fMRI, T-fMRI, resting state fMRI,

rs-fMR, or BOLD) and (artificial intelligence, AI, machine learning, ML, deep learning, or DL) and (detection, diagnosis, or findings). The eligibility criteria included original research articles, published, accepted for publication, or available online in English. Age- or sex-based studies were included. Case reports, or review articles, including narrative, systematic reviews, and meta-analyses, were excluded from data extraction but were used as reference searches. Studies compared a group of ASD individuals with a group of typically developed controls are included. Yet, studies conducted on the comparison of ASD with other neuro-developmental, cognitive, or psychiatric disorders such as Attention-Deficit Hyperactive Disorder (ADHD) were excluded. Given that this review is designed to look at DTI and fMRI studies based on ML findings, ML algorithms with neuroimaging data were used as a biomarker in differentiating ASD individuals from typically developed controls. In addition, other imaging modalities such as structural MRI, MR spectroscopy, or positron emission tomography were excluded as well.

1 Diffusion Tensor Imaging (DTI)

DTI has drawn a lot of attention over the last two decades as it allows the analysis of the structural connectivity of the brain white matter (WM) [43]. Although a lot of information could be revealed from the axonal organization, conventional MRI techniques were not capable of capturing this information due to limited resolution and contrast. Fortunately, this has been achievable using DTI, which is characterized by its diffusion anisotropy contrast that reveals information about axonal orientation. DTI is based on the diffusion of water molecules, which is easier in the direction of the axonal bundles compared to the perpendicular direction, making it feasible to determine axonal direction. In DTI, the diffusion of water molecules is measured along six predetermined directions, from which the diffusion along any arbitrary direction can be calculated. This is mathematically represented by a 3×3 matrix, called the diffusion tensor [44], usually interpreted graphically as an ellipsoid. Several features can be extracted from the diffusion tensor, most importantly, fractional anisotropy (FA), axial diffusivity (AD), radial diffusivity (RD), and mean diffusivity (MD) [45]. Those measured parameters provide information about WM micro-structure and connectivity [46]. Other features derived from those measurements, such as trace, skewness, rotational invariance, and others, characterize different aspects of diffusivity in WM tracts [47].

ASD findings using DTI

With the aim of analyzing WM connectivity, many studies were introduced to investigate different DTI metrics, such as FA, MD, AD, RD, skewness, etc. There have been many studies that have demonstrated reduced FA and increased MD in widely distributed brain regions of people with autism spectrum disorders.

Several studies [48–57] have examined WM in people with ASD using DTI, comparing their WM microstructure with that of TD individuals. Barnea-Goraly and colleagues [48] found that certain WM areas had reduced FA in ASD, when taking

into consideration IQ, age, and gender. The WM tracts they identified were located in brain regions known to be associated with social cognition e.g., temporoparietal junction, superior temporal sulcus, ventromedial prefrontal cortex, fusiform gyrus, and anterior cingulate gyrus. While the aforementioned study [48] did not report any ASD-related alterations in MD, the work of Alexander et al. [49] found significant differences in MD as well as FA. Specifically, MD was increased in callosal WM, while FA was reduced, for individuals with ASD as compared to TD subjects. Higher MD and RD with reduced FA in autistic subjects was reported by [50]. Another study [51] examining the frontal lobe WM reported lower FA values and a higher diffusion coefficient in ASD.

The structural integrity of WM was examined using DTI [52], comparing ASD and TD groups with correction for age and IQ, and also without. The individuals with ASD were found to have significantly higher MD generally in cerebral and cerebellar WM, regardless of whether the correction was performed or not. The authors also noted decreased FA in ASD within the superior and inferior longitudinal fasciculi bilaterally, and in the left corona radiata; however, this decrease almost disappeared after corrected for age and IQ. From this, they inferred that the kurtosis of fractional anisotropy distribution is greater in ASD. Travers et al. [53] presented a comprehensive review of 48 studies that were carried out from 2004 to 2012 for the purpose of studying the WM integrity of ASD using DTI. The review found consistent results among these studies in that ASD cases on average exhibited reduced WM integrity compared to TD individuals, indicated by lower FA and increased MD across multiple brain regions. The findings were more consistent in some regions with respect to others, especially in the cingulum and corpus callosum. Vasa and colleagues [56] reviewed some of the current structural and functional connectivity ASD data to examine the "disrupted connectivity" theory. They identified many confounding factors in the literature that could have affected the conclusions and highlighted the conflicting results. Kuno et al. [57] examined correlations between DTI parameters (FA, MD, AD, R) and scores on the Autism-spectrum Quotient (AQ). They focused on WM tracts that were known from previous studies to be altered in obsessive-compulsive disorder (OCD) patients with autistic traits. Their results suggested that the variations in WM features may be explained partially by autistic traits in OCD patients.

Many studies have shown reduced FA and increased MD in widespread WM tracts and brain regions of the ASD population when compared to TD controls, denoting reduced WM integrity. The most commonly involved tracts are long-range association fibers that directly and indirectly connect the brain regions responsible for social cognition and verbal communication. Those tracts include the superior longitudinal fasciculus, occipitofrontal fasciculus, arcuate fasciculus, uncinate fasciculus, inferior longitudinal fasciculus, and cingulum. [11, 58–60]. A study by Jung et al., 2019 [58] revealed the correlation between impaired connectivity at the occipital cortex in ASD boys with the core symptoms and clinical outcomes of ASD. A significant negative correlation was found between tract length (left cingulum cingulate gyrus and right uncinate fasciculus) and the total score of the Social Communication Questionnaire (SCQ).

Valenti [61] presented a comprehensive review of several published articles that

used DTI in the evaluation of Corpus Callosum (CC) integrity in ASD. They found a significant difference in DTI and tractography findings between the ASD group and healthy controls, indicating both micro and macrostructure alterations in CC. In addition, those structural alterations are correlated with socio-communicative deficits. Shukla et al. 2013 found increased RD and reduced FA in CC and Internal Capsule (IC). Others have shown altered IC connectivity with the correlation of DTI changes with the core ASD symptoms [62], [63], [64].

A study focused on language-related tracts (arcuate fasciculus) to differentiate ASD patients from non-ASD individuals with a developmental language disorder has found a significant reduction in FA of the arcuate fasciculus in ASD individuals [65]. Moreover, other studies reported age-related differences in the widespread WM microstructure of the ASD population when compared to healthy controls. For example, in [66], [67] have found increased FA in autistic infants and toddlers, while indices decreased in elder autistic children. This was attributed to better tract coherence and alignment in infancy. Other studies have shown the opposite as there was a significant positive correlation of FA with increasing age of autistic children, while MD and RD measures showed a significant negative correlation with age [68], [69]. They suggested that neurodevelopmental maturation of WM trajectories with increased age is associated with changes in diffusivity parameters.

Apart from using DTI biomarkers alone, several imaging-based ML studies have been applied to overcome the limitations found in DTI studies alone. DTI lacks a full description of crossing WM trajectories. Despite the sensitivity of DTI metrics to capture microstructural changes, DTI is less specific to other WM disorders affecting myelination and axonal density [70]. In addition, there is still limited integration between clinical and imaging biomarkers. The need for informative data relevant to diagnosis and treatment decisions is challenging. Therefore, ML has been developed to aid the identification and classification of ASD children using clinical, behavioral, and imaging biomarkers [20].

DTI-based ML Classification

Several ML studies based on DTI metrics were performed by applying different features obtained using different algorithms for image processing. For example, Ingalhalikar et al. [71] study of 45 autistic subjects and 30 TDs, DTI-based features were extracted like FA and MD metrics in each ROI to classify ASD patients and controls by learning the pattern of the disease. Also, they correlated the degree of ASD with a clinical score to each subject to aid in the diagnosis, using SVM for classification, manifesting a diagnostic potential when the authors split ASD to language impaired and non-language impaired groups, achieving an accuracy up to 80%. Li H et al. [72] used brain connectivity network features obtained from DTI to identify faulty subnetworks to distinguish ASD subjects from TD group. The detection was done by SVM- recursive feature elimination (RFE) algorithm. Jin Y et al. [73] used features extracted from ROI-based WM connectivity and DTI metrics, such as FA, MD, and fiber length. A multi-kernel SVM was used for the discrimination of ASD 6-month high-risk infants from low-risk infants.

Zhang et al. [74] used whole brain fiber clustering analysis with multi-fiber tractography, FA, and MD features. An SVM classifier was used to distinguish ASD from TDs. Qin et al. [75] used graph theory to analyze the topology of the WM network of ASD preschool children. Edges and nodes were defined as FA and 90 brain regions respectively. They found disturbed topology of the structural networks of ASD subjects as compared to TDs. Payabvash [70] used features extracted from edge density imaging (EDI) as well as from conventional DTI metrics such as FA, MD, and RD. Variable ML classifiers were used to discriminate ASD children from TDs. The best accuracy was achieved with the EDI-based random forest model. Saad et al. [76] used DTI-based connectivity features with graph theory to classify ASD and TDs. The classification was performed by an SVM and a linear discriminant analysis (LDA). The principal component analysis (PCA) approach was used to reduce noisy features. Better accuracy was obtained with SVM and 2 PCA features.

In one study of 75 subjects, [71] showed a diagnostic predictive capability, with 80% accuracy, based on FA and MD. Another study that aimed to provide a classification of autism, performed on 73 subjects used the shape of WM tracts to achieve an accuracy up to 75% [77]. In [55], a sample of 38 infants from the Infant Brain Imaging Study (IBIS) were used for the diagnosis of autism using spherical harmonics, where WM connectivity integrity was analyzed.

Aside from classical analysis studies, plenty employed ML techniques for ASD classification. The whole ABIDE-I fMRI dataset was tested with a refined deep learning model that was introduced by Heinsfeld et al [33] that exceeded the previous state-of-the-art performance, achieving 70% accuracy. Khosla [78] presented another deep learning algorithm using a volumetric convolutional neural network that fits non-linear predictive models on 3D resting state fMRI (rs-fMRI) input and recorded a classification accuracy up to 73% on ABIDE-I rs-fMRI data.

Other hybrid studies combined DTI features with features extracted either from fMRI or structural MRI (sMRI). For example, An et al. [79] used Region to region fiber connectivity DTI features and ROI-based Functional connectivity (FC) features from fMRI to validate connectivity patterns and then classify ASD subgroups using multi-view expectation maximization formulation (mv-EM). In [80], authors proposed a framework exploiting features from both sMRI and fMRI, applied on 185 subjects from the National Database for Autism Research (NDAR), achieving 81% accuracy fusing both modalities. Deshpande et al. [81] used FA and FC values with a Multi-variate autoregressive model (MVAR). They investigated the differences between brain regions that may underpin the theory of mind in young ASD patients and TDs. The classification was done by an SVM classifier. Crimi A et al. [82] used structural and functional connectivity features with a constrained multivariate auto-regressive model (CMAR) that allows fusing the structural connectivity with the information from the functional time series, to represent effective brain connectivity. The classification between ASD subjects and TDs was performed by an SVM classifier. D'Souza NS et al. [83] used phenotypic measures of rs-MRI connectivity and DTI tractography features with multimodal graph convolutional network (M-GCN) to extract predictive biomarkers from both ASD individuals and TDs. Irimia et al. [84] used structural morphometric features cortical thickness, volume, area,

and mean curvature as well as connectivity features to distinguish ASD individuals from TDs. Moreover, they distinguished ASD males and females. The used classifier was an SVM model. Eill et al. [85] combined the anatomical features (surface area, mean curvature, cortical thickness, volume, and local gyrification index), DTI metrics (FA, MD, RD, AD), and ROI-based FC matrices. They applied a conditional random forest algorithm (CRF) to assess the role of each modality and explore the more informative one in diagnostic prediction. The use of combined variables achieved higher accuracy (92.5%), and rs-fMRI connectivity variables provided better performance than other anatomical modalities in the classification of ASD individuals from TDs. Table 1 summarized the results of the discussed covered papers

Table 1. Summary of DTI based ML classification

Article	Dataset	Number		Age	Feature selection	Classifier	Accuracy
		ASD	TD				
An et al. 2010 [79] DTI+ fMRI	Clinical	n.s.	n.s.	n.s.	-DTI: Regional fiber connectivity -fMRI: ROI-based FC	Multi-view Expectation Maximization formulation. (mv-EM)	Max Error mv-EM: 8.55
Ingalhalikar et al. 2011 [71]	Clinical	45	30	10.5±2.5	FA, MD	SVM	80%
Li et al., 2012 [72]	Clinical, simulated	10	10	7-14	-Brain connectivity network	SVM + RFE	100%
Deshpande et al. 2013 [81] DTI+ fMRI	Clinical	15	15	21.1±0.9	-FA values -FC values	MVAR SVM	95.9%
Jin et al., 2015 [73]	NDAR	40	40	6-months	-FA, MD, Fiber length	Multikernel SVM	76%
Crimi et al. 2017 [82] sMRI+ DTI	ABIDE-II	31	23	n.s.	-Structural and FC matrix	-SVM	- sMRI: 60.57% -fMRI: 72.32%
Zhang et al., 2018 [74]	Clinical	70	79	11.0±2.6	-WM fiberclusters -FA, MD	SVM	78.3%
Irimia et al., 2018 [84] sMRI+ DTI	Clinical	110	83	12.74	-Structural: cortical thickness, volume, area, and mean curvature. -Connectomic: Connectivity density	SVM	74.09 - 94.82%
Payabvash 2019 [70]	Clinical	14	33	8.9±2.7	- Edge density imaging (EDI) - FA, MD, RD	-Naive Bayes -RF -SVM	75.3% in EDI using RF
Saad et al., 2019 [76]	USC	51	41	n.s.	- Graph theory-based features	-SVM	75%
Eill et al., 2019 [85] sMRI+ DTI+ fMRI	Clinical	46	47	13.63± 2.81	-Anatomical: cortical features -DTI metrics: (FA, MD, AD, RD). -ROI- based FC matrices.	- CRF	-67% per modality separately. -92.5 % combined
D'Souza et al., 2021 [83] DTI + rs-fMRI	Clinical	57	275	n.s.	-Phenotypic measures of rs-fMRI. -DTI tractography	-M-GCN	—

2 Functional MRI

ASD findings using fMRI

Functional neuroimaging is used to investigate the functional connectivity and activity of brain regions. Electroencephalography (EEG) has been used as a basic method to record electrical activities of the brain from the scalp with a high temporal resolution (in milliseconds) [86]. fMRI detects brain activity by measuring the associated variations in Blood Oxygenation Level-Dependent spontaneous signals (BOLD) in response to various stimuli [87]. It is a four-dimensional technique (4D) that captures a three-dimensional brain volume (3D) repeatedly over a period of time. This technique has a high spatial resolution (in millimeters) but a low temporal resolution [88]. This could be explained by the time limitations of fMRI that cannot record the fast dynamics of brain activities and the slow response of the brain hemodynamic system, thus requiring multiple scans over time. Moreover, fMRI is sensitive to motion artifacts [89]. fMRI-based techniques include two broad categories: event-related or task-based (T-fMRI) and resting-state (rs-fMRI). Task-based (T-fMRI) measures brain function after performing specific tasks, while (rs-fMRI) measures brain function in the absence of task demands.

Task-based (T-fMRI)

Task-based protocols employ paradigms that map the core behavioral symptoms of ASD patients, namely, facial emotional recognition, response to social stimuli, and reward behavior [11]. Other tasks include motor, visual processing, language, auditory, and executive functions. Social communication skills are supported by a distributed brain network within different brain regions collectively named "social brain" [90]. Many T-fMRI studies have notably demonstrated atypical activity in social brain regions among ASD individuals during social tasks (primarily hypoactivation). Social communication deficits in ASD include variable manifestations like impaired recognition of faces, making inferences about others' intentions, and diminished social responsiveness. In addition to reduced attention to social cues, human voices, and biological motions [11,90,91].

A Study that examined the activity of social brain regions in response to the visual perception of generic faces showed hypoactivation in the fusiform gyrus and amygdala among ASD children. These regions are responsible for such tasks. However, similar activation was found in ASD patients as well as TD controls when the faces were familiar [92]. Another study employed a task to distinguish between attention to biological motions (eye gaze, walking, hand, or mouth movements) versus mechanical motions (clock or wheel). This study revealed reduced activation of the superior temporal sulcus and ventrolateral prefrontal cortex in ASD children than in TD controls. The study clarified that ASD children are easily distracted by non-facial stimuli and cannot fixate on faces to the same degree as normal children [93]. Investigating brain activity in response to cognition of facial expressions, such as sad

facies (visual tasks), revealed increased activation in the amygdala, ventral prefrontal cortex, and striatum in the adolescent ASD group compared to the control group [94].

Regarding the response to reward or positive feedback behavior, ASD children are less responsive than normal children. Normally, reward activates the visual striatum region and engages the frontostriatal network [11]. A study employed a social reward task like a smiling face or a momentary reward task as gold coins. ASD boys showed non-activated visual striatum, while it was activated in TD boys [95]. Moreover, a study comparing the response of both ASD boys and girls, revealed more activation in the lateral frontal cortex and insula of ASD girls, denoting that suppressed reward center activation is a distinctive feature of ASD boys [96].

A meta-analysis of fMRI studies was proposed by Philip et al. [97]. They reviewed T-fMRI studies that investigated the functional brain response to auditory and language-related tasks. They revealed reduced activation in clusters of brain regions in ASD children, adolescents, and adults compared to TD controls. Those regions are both superior temporal gyri, the right pyramids of the cerebellar vermis, and the left middle cingulate gyrus. The superior temporal gyrus is activated with receptive language, so reduced activation in response to spoken language denotes the underlying verbal communication difficulties in ASD individuals. On the other hand, relative over-activation in ASD adults more than in controls was found in the posterior cingulate gyrus, the motor cortex, and the cerebellar declive. The exact cause of increased activation in ASD groups was not clear; this may be suggested by the use of atypical language processing strategies [97].

Resting-state (rs-fMRI)

The complexity and different varieties of fMRI tasks, in addition to the unique social skills and intellectual condition of ASD children, can limit some task-based experiments. Another point is the difficulty of tasks with potential language barriers that preclude some children particularly infants from participation [11, 98].

rs-fMRI is a promising alternative to T-fMRI. The technique is especially suitable for infants and toddlers, and whenever task performance itself is in question. It helps examine functional brain connectivity in absence of task performance. The total time of the examination is about 5-6 minutes. The participants just lay in the MRI scanner closing their eyes or fixing on a cross-hair [98].

Several rs-fMRI studies aim to explore large-scale resting brain networks (RBNs). Those are organized brain regions that show cortical synchronization patterns with coherent spontaneous fluctuations in neural activity during rest [99]. RBNs include default mode network, dorsal and ventral attention network, salient network, visual network, and sensorimotor networks [99].

It was found that the most common region with altered brain connectivity is the default mode network (DMN). It gets activated during the resting state. Whereas, it gets less activated on the engagement of cognitively-demanding tasks [100]. DMN is a large-scale network composed mainly of the posterior cingulate gyrus, precuneus, and medial prefrontal cortex. It has shown reduced connectivity in ASD patients

compared with TD controls [101], [100], [102]. The dorsal attention network (DAN) is located in the intraparietal sulcus and frontal eye field. This network is activated to reorient the attention towards relevant stimuli. Sun et al. [99] have shown increased functional connectivity in the superficial temporal gyrus and cerebellum indicating the presence of circuit connections between DAN and cerebellum. The ventral attention network (VAN) also has been studied by SUN [99]. They found increased connectivity in the insula which is a critical region in VAN responsible for social emotions. The salience network is another RSN that has been examined. It is composed primarily of the dorsal anterior cingulate cortex and the anterior insula. It is linked with the detection and filtering of salient stimuli [11]. Additionally, a study by Wang et al. [103] has investigated the functional connectivity of sensory networks in autistic children including auditory, visual, and sensorimotor networks. They found increased functional connectivity in all networks in ASD children and was correlated with the severity of social impairment of the children.

Disrupted Connectivity theories

Other several networks have been examined by rs-fMRI and have provided support to the theory of "brain hypoconnectivity" in ASD. Long-range reduced brain connectivity was found in the superior temporal region of autistic individuals when compared with TD controls [104]. Uddin et al. [105] have observed a reduction in functional connectivity in this network with 83% accuracy in differentiating autistic children from TD controls. Based on a multivariate autoregressive model, an algorithm based on a ML algorithm for analyzing functional connectivity in ASD subjects was used in a previous study [106]. In that study, it was found that people with ASDs have reduced functional connectivity, which supports the hypothesis that autism is characterized by a deficit in functional connectivity or 'underconnectivity'.

In accordance with the underconnectivity theory [107], cognitive disorders manifest themselves in reduced synchronized brain activity during integrative processing tasks, such as the synthesis of a sentence from a set of words. There is evidence in [106], and [108] for the hypothesis of underconnectivity. Similarly, there was lower functional connectivity in the superior parietal and visuospatial regions of ASD when compared to TD [109]. In another study by [110], there was reduced connectivity between the temporal and frontal cortex, but no global abnormalities were found. In [111], abnormalities were reported in functional networks, which were more evident in networks related to social information processing.

In addition, other studies have observed underconnectivity in latero-basal subregion of the amygdala, interhemispheric connectivity in sensorimotor and occipital cortices, and in connections between anterior and posterior cingulate gyrus and precuneus [109]. Overconnectivity has been also observed in some studies, they found increased connectivity in some areas as frontal, temporal, and occipital regions ([112], [113], [102]). Kleinhans and his colleagues [114] have observed areas of overconnectivity within the amygdala (superficial and centro-medial subregions). However, the latero-basal subregion showed underconnectivity, this region stands for

the presentation and severity of ASD symptoms. The mixed pattern or the inconsistent over- and un-der-connectivity can be attributed to the small sample size used in these studies, phenotypic heterogeneity among ASD individuals, or an adjustment mechanism by the brain to by-pass the under-connected regions [11, 98].

Nevertheless, brain networks associated with ASDs exhibit both under-connectivity and over-connectivity [111, 115]. Unlike previous studies, ASD has not only reported results that indicated brain underconnectivity but also increased brain connectivity in some areas when compared to healthy controls [115]. In the latter study, functional connectivity patterns were analyzed, specifically interhemispheric connectivity analysis, and it was found that ASD subjects had both under- and over-connectivity. Furthermore, the presence of altered connectivity was verified in [116]. The subjects with ASD displayed both under- and over-connectivity between different brain regions. Furthermore, a study by [117] identified hyperconnectivity in severely socially challenged autistic children.

fMRI based ML Classification

Recent progress in ML algorithms combined with fMRI techniques is established for the diagnosis of ASD and has shown promising results. For example, Abraham et al. [118] used features selected from ROI-based resting-state FC matrices to differentiate ASD from TDs. They used an SVM classifier and found an increase in the predictive power with the increase in participant numbers. Emerson et al. [119] used extracted features from ROI-based resting state-FC matrices for the prediction of ASD in high-risk 6-month infants, based on cor-related brain metrics with 24-month ASD-related behaviors. They achieved 96.6% classification accuracy of ASD individuals at 24 months. The classification was performed by an SVM classifier. Guo et al. [120] used ROI-based resting state-FC matrices with deep neural networks with feature selection (DNN-FS) to select the most relevant features from FCs related to ASD from the default mode to identify ASD individuals from TDs. Jahedi [121] obtained ROI-based FC features as biomarkers to identify ASD patients from TDs. Combined use of conditional random forest (CRF) and random forest classifiers achieved the best prediction accuracy.

Kam et al. [122] used extracted features from seed-based FC matrices with Discriminative restricted Boltzmann machines (DRBM) to identify dominant FCs to differentiate ASD from TDs. An ensemble classifier was applied and obtained a high accuracy with multiple clusters using hierarchical-level clustering of networks. Sadeghi et al. [123] used features from ROI-based FC nodal matrices to extract local and global parameters of brain networks to identify ASD from TDs. Multiple classifiers were used but SVM showed superiority to other classifiers. Subbaraju et al. [124] used extracted features from ROI-based resting state-FC matrices with spatial feature-based detection method (SFM) to extract the most discriminative blood oxygenation level-dependent (BOLD) signals. An SVM classifier was used in the classification of ASD individuals versus TDs. Tejwani et al. [125] used extracted features from ROI-based enhancing FC variability across brain regions to distinguish between ASD subjects and TDs. They used SVM, RF, Naïve Bayes, and multi-layer percep-

tion algorithms for classification. Heinsfeld et al. [33] used extracted features from ROI-based FC matrices with DNN algorithm. The proposed method achieved better accuracy than SVM and RF classifiers in classifying ASD and control subjects. Bi et al. [126] used ROI-based FC features to differentiate between autistic individuals and TDs. They applied a random SVM cluster and achieved high classification accuracy.

Fredo et al. [127] used features extracted from ROI-based FC matrices to classify ASD individuals and TDs. The detection was done by CRF. Li et al. [128] conducted a 2-stage pipeline method, composed of DNN and prediction distribution analysis, to investigate its accuracy in classifying two datasets of ASD and TD subjects. They extracted features from ROI-based FC matrices from both resting-state and task-fMRI. Bernas et al. [129] extracted temporal neurodynamic fMRI biomarkers for ASD diagnosis with Wavelet coherence maps. The detection was done by an SVM classifier. Bhaumik et al. [130] used features extracted from ROI-based FC matrices for the prediction and diagnosis of ASD subjects versus TDs. The detection was done by an SVM and partial least square regression (PLS) algorithms. Dekhil et al. [131] used power spectral densities as extracted features to classify ASD individuals and TDs. An SVM was used and achieved high di-agnostic accuracy and prediction of clinical phenotypes. Xiao et al. [132] used the extracted time courses of each subject with NN algorithms. The extracted features are inputted into a stacked autoencoder (SAE) and then into a subsequent softmax classifier for the identification of school-aged ASD children from TD school-aged children. Yang et al. [133] used features extracted from ROI-based FC matrices to classify ASD and TD subjects. The detection was performed by SVM, LR, and Ridge classifiers. They found that accuracy is improved with combined classifiers. Wang et al. [134] used extracted features from ROI-based FC matrices to classify ASD and TD subjects. In [135], they used an SVM recursive feature model to achieve a high classification accuracy of ASD and TD individuals on both global and across-sites datasets. They also used extracted features from ROI-based FC matrices to identify ASD subjects and TDs. An SVM-recursive feature model and a stacked sparse auto-encoder (SSAE) were used to eliminate some meaningless features to enable the SSAE to extract insightful features.

Aghdam et al. [136] used extracted features from Fast Fourier transformation with the CNN method in order to classify ASD subjects and TDs. Huang et al. [137] used extracted features from rs-fMRI multiple group-sparse networks. They used an SVM classifier in distinguishing ASD individuals. Jun et al. [138] used extracted features from rs-fMRI local functional characteristics based on the estimated likelihood of ROI by Hidden Markov Models (HMMs) to identify meaningful information for ASD detection. The detection was performed by an SVM classifier. Eslami et al. [139] used extracted features from ROI-based FC matrices with ASD-DiagNet in order to classify ASD and TD subjects and the proposed method achieved high classification accuracy. Mostafa et al. [140] extracted features from ROI-based FC matrices and then the eigenvalues of the Laplacian matrix of the brain network with a sequential feature selection algorithm. Linear Discriminant Analysis (LDA) was used to classify ASD and TD subjects. Song et al. [141] used extracted features from community pattern analysis of FC to classify the ASD population and TDs, in addition to the

prediction of the clinical class of ASD individuals. The detection was performed by LDA. Spera et al. [142] used extracted features from ROI-based FC matrices to classify ASD and TD subjects. They selected a homogenous cohort of young ASD males to lessen the impact of confounding factors. The detection was used by linear kernel SVM. Tang et al. [143] used extracted features from ROI-based FC from DMN and whole brain with Joint symmetrical non-negative matrix factorization (JSNMF).

An SVM classifier was used to classify ASD and TD subjects. Yamagata et al. [144] used extracted features from ROI-based FC matrices with a multivariate ML approach. A Sparse Logistic Regression (SLR) classifier was used to classify pairs of ASD patients and their unaffected siblings from pairs of TDs and their siblings according to the endophenotype. Chaitra et al. [145] used extracted features from ROI-based FC matrices to classify ASD patients and controls. They employed a Recursive-Cluster-Elimination SVM algorithm. Fan et al. [146] used extracted features from maps based on estimated likelihood values of ROI by HMM to identify ASD individuals from TDs. The detection was performed by an SVM classifier. Liu et al. [147] employed the elastic network method to extract features from ROI-based FC matrices to distinguish ASD individuals from TDs. They obtained high classification accuracy using SVM classifier in the automatic diagnosis of ASD than LASSO and RR algorithms. Hu et al. [148] utilized extracted features from ROI-based FC matrices with a fully connected neural network (FCNN) model in the classification of ASD population versus TDs. Sherkatghanad et al. [149] used extracted features from ROI-based FC matrices to classify ASD individuals and TDs using a CNN model. CNN model is computationally less intensive as it uses fewer parameters than state-of-the-art methods and can be used in prescreening of ASD patients. Thomas et al. [150] used the temporal statistics of rs-fMRI data with 3D-CNN to classify ASD individuals. The classification was also performed by an SVM model on the same dataset. The best classification accuracy obtained by the SVM algorithm was 66%, while 3D-CNN achieved 64%, denoting that 3D-CNN could not learn additional information in classifying ASD and TDs. Jiao et al. [151] utilized extracted features from ROI-based FC matrices with the CapsNET method to classify ASD individuals and TDs. Moreover, they stratified ASD subjects into groups based on distinct FC measures. Liu et al. [152] used the extracted features from ROI-based FC matrices with an elastic network method to classify ASD individuals versus TDs.

Liu et al. [153] utilized the extracted dynamic features from ROI-based FC matrices with a multi-task feature selection method. A multi-kernel SVM classifier was used to classify ASD individuals versus TDs. Zhang et al. [154] utilized the rs-fMRI dataset of ASD subjects and TDs with fast entropy method which includes approximate entropy (ApEn) and sample entropy (SampEn). The SVM classifier was used to diagnose ASD. Ronicko et al. [155] used extracted features from ROI- based FC matrices with partial and full correlation methods. Classification of ASD individuals and TDs was built by different models namely, SVM, RF, Oblique RF, and CNN. Khan et al. [156] analyzed the extracted features from ROI-based FC matrices with a Teacher Student neural network-based feature selection method. Different classifiers were used in classifying ASD and TD subjects such as SVM, RF, LR, Decision trees, and linear discriminant classifiers. Reiter et al. [157] used extracted features

from ROI-based FC matrices of ASD subjects and TDs. RF classifier was used to investigate the effect of heterogeneity of ASD sample on classification accuracy. They found that the most homogeneous samples achieved better RF classifier performance. Devika & Oruganti [158] utilized extracted data from FC matrices to distinguish ASD and TD subjects. The classification was performed by an SVM model. Ahammed et al. [159] used the extracted features from ROI-based FC matrices with Bag of features extraction (BoF) method. The SVM was used as a classifier for identifying ASD and TD subjects. Ahammed et al. [160] used the extracted features from ROI-based FC matrices. They applied a DarkASDNet method to classify ASD and TD subjects. Graña & Silva [161] utilized the extracted features from ROI-based FC matrices of ASD subjects and TDs using 9 different classifiers. They explored the impact of choices during building up the ML pipelines on the predictive performance. They found that the selection of some feature extraction methods can strengthen the classifier performance, such as the classical principal component analysis (PCA) and factor analysis (FA). Al-Hiyali et al. [162] used the temporal dynamic features from default mode network regions (DMN) with several deep learning models for the diagnosis and classification of ASD. SVM and K-nearest neighbors (KNN) were used for ASD classification and the KNN achieved the highest classification accuracy. Pominova et al. [163] utilized extracted features of FC matrices and full-size MRI series with 3D convolutional autoencoders method. To classify ASD and TD subjects, the SVM classifier was used. Yin et al. [164] used extracted features from ROI-based FC matrices with graph theory and autoencoders to distinguish ASD subjects from TDs. SVM, K-nearest neighbor (KNN), and DNN algorithms were used for classification. Chu et al. [165] used extracted features from ROI-based FC network regions with multi-scale graph convolutional network (GCN) to classify ASD patients and TDs by learning the distinctive FC features. Yang et al. [166] used extracted features from FC matrices to distinguish ASD individuals from TDs. they used different classifiers as LR, KSVM, DNN, and supervised learning classifiers, among them, the KSVM achieved the best classification accuracy. Table 2 summarized the results of the discussed covered papers.

Table 2. Summary of fMRI-based ML classification

Article	Dataset	Number		Age	Feature selection	Classifier	Accuracy
		ASD	TD				
Abraham et al. 2017 [118] rs-fMRI	ABIDE	403	468	n.s.	ROI-based FC matrices.	SVM	67%
Emerson et al. 2017 [119] fMRI	Clinical	11 high risk infants	48	6-24 months	ROI- based FC matrices.	SVM	96.6%
Guo et al. 2017 [120] rs-fMRI	ABIDE I	55	55	12.7 ± 2.4	ROI-based FC matrices.	DNN-FS	86.36%
Jahedi 2017 [121] fcMRI	ABIDE	126	126	17.3±6.0	ROI-based FC matrices	-Conditional random forest (CRF) -RF	92.7%
Kam et al. 2017 [122] rs-fMRI	ABIDE	119	144	<20	Seed-based FC	DRBM	-Single cluster 67.42% -Multiple cluster 80.82%
Sadeghi et al. 2017 [123] rs- fMRI	ABIDE	31	29	20.49 ± 6.16	ROI-based FC nodal matrices	SVM	92%
Subbaraju et al. 2017 [124] rs-fMRI	ABIDE PCP	505	530	6.5-58	ROI-based FC matrices	SVM	78.6%-95%
Tejwani et al. 2017 [125] rs-fMRI	ABIDE	147	146	n.s.	ROI-based FC matrices	SVM, RF-Naïve Bayes, multilayer perception algorithm	65%
Heinsfeld et al. 2018 [33] rs-fMRI	ABIDE I	505	530	Site-specific	ROI-based FC matrices	DNN	70%
Bi et al. 2018 [126] rs-fMRI	ABIDE	45	39	13.4 ± 2.4	ROI-based FC	Random SVM cluster	96.15%
Fredo et al. 2018 [127] rs- fMRI	ABIDE I, II	160	160	12.16±2.76	FC matrix	CRF	65%
Li X et al. 2018 [128] T-fMRI+rs-fMRI	T-fMRI Clinical rs-fMRI ABIDE I	82 41	48 54	n.s.	—	2-stage pipeline (DNN+ Prediction distribution analysis)	T-fMRI 87.1% fMRI 85%
Bernas et al. 2018 [129] rs-fMRI	ABIDE	24	39	15.5±1.0	Wavelet coherence maps	SVM	86.7%
Bhaumik et al, 2018 [130] rs-fMRI	ABIDE	167	205	13.4±5.1	ROI-based FC	-SVM PLS	62%
Dekhil et al. 2018 [131] rs- fMRI	NDAR	123	160	12.9±3	Power spectral densities	SVM	91%
Xiao et al. 2018 [132] fMRI	ABIDE	42	42	9.78±1.5	Time courses of networks	SAE -NN	87.2%
Yang et al. 2019 [133] rs-fMRI	ABIDE	505	530	6-64	ROI-based FC	SVM, LR, Ridge	71.98% with Ridge
Wang et al. 2019 [134] rs- fMRI	ABIDE I, II	255	276	Site-specific	ROI-based FC	SVM recursive feature	90.6%
Wang et al. 2019 [135] rs- fMRI	ABIDE	501	533	n.s.	ROI-based FC	SVM recursive feature SSAE	93.59%
Aghdam et al. 2019 [136] rs- fMRI	ABIDE I, II	210	249	5-10	Fast Fourier transformation	CNN	70.5%
Huang et al. 2019 [137] rs- fMRI	ABIDE	45	47	11.1±2.3	Multiple group-sparse networks	SVM	79.4%
Jun et al. 2019 [138] rs-fMRI	ABIDE	121	171	14.4±5.8	maps based on estimated likelihood of ROI by HMM	SVM	84.6%
Eslami et al. 2019 [139] rs- fMRI	ABIDE I	505	530	Site-specific	ROI-based FC	ASD-DiagNet	70.3%

Summary of fMRI-based ML classification (cont'd)

Article	Dataset	Number		Age	Feature selection	Classifier	Accuracy
		ASD	TD				
Mostafa et al. 2019 [140] rs- fMRI	ABIDE I	403	468	Site-specific	The eigenvalues of the Laplacian matrix of brain network	LDA	77.7%
Song et al. 2019 [141] rs-fMRI	ABIDE	119	116	Site-specific	Community pattern analysis of FC	LDA	85.16% for in-site, ~75.00% for multisite
Spera et al. 2019 [142] rs-fMRI	ABIDE	102	88	6.5-13	ROI-based FC	Linear Kernel SVM	71%
Tang et al. 2019 [143] rs-fMRI	ABIDE	42	37	n.s.	ROI-based FC from DMN	SVM JSNMF	AUC= 62.6
Yamagata et al. 2019 [144] rs- fMRI	Clinical	15	45	28.3±6.1	ROI-based FC	SLR Multivariate ML	75%
Chaitra et al. 2020 [145] fMRI	ABIDE	432	556	n.s.	ROI-based FC	Recursive-Cluster-Elimination SVM	70.1%
Fan G et al. 2020 [146]	ABIDE	145	157	16.4±6.5	Estimated likelihood values of ROI by HMM Maps	SVM + two-group cross-location HMM	74.9%
Liu et al. 2020 [147]	ABIDE	506	548	16.6±8.1	ROI-based FC	SVM elastic network method	76.8%
Hu et al. 2020 [148]	ABIDE	403	468	n.s.	ROI-based FC	FCNN	69.8%
Sherkatghanad et al. 2020 [149]	ABIDE I	505	530	Site-specific	ROI-based FC	CNN	70.2%
Thomas et al. 2020 [150]	ABIDE 1 and II	620	542	5-64 Median=13	Nine Summary measures	-3D-CNN - SVM	64%
Jiao et al. 2020 [151]	ABIDE I	505	530	n.s..	ROI-based FC	CapsNET	71%
Liu et al. 2020 [152]	ABIDE	250	218	Center specific	ROI-based FC matrix	Elastic Net	83.33%
Liu et al. 2020 [153]	ABIDE I	403	468	17.07± 7.95	Dnaymic FC	Multi-kernel SVM	76.8%
Zhang et al. 2020 [154]	ABIDE I	21	26	25.3± 6.3	ApEn and SampEn	SVM	AUC= 62
Ronicko et al. 2020 [155]	ABIDE I, II	300	300	11.87±2.8	Partial and full correlation ROI-based FC matrix	RF, SVM, ORF, NN	70.3%
Khan et al. 2020 [156]	ABIDE	505	530	Site-specific	ROI-based FC matrix	SVM, RF, LR, Decision Trees, and Linear Discriminant classifier	82%
Reiter et al. 2021 [157]	ABIDE	306	350	6-18	ROI-based FC matrix	RF	73.75%
Devika, et al. 2021 [158]	ABIDE II	23	15	n.s.	FC matrix	SVM	80.76%
Ahammed et al. 2021 [159]	ABIDE I	19	19	15-35	Bag of features extraction (BoF)	SVM	81%
Ahammed et al. 2021 [160]	ABIDE I	79	105	15.25±6.58	ROI-based FC matrix of 3D-fMRI	DarkASDNet	94.7%
Graña & Silva 2021 [161]	ABIDE	408	476	Site-specific	FC matrix	9 classifiers	Best median AUC=0.767
Al-Hiyali et al. 2021 [162]	ABIDE	41	41	n.s.	Default mode network regions (DMN)	-SVM - K-nearest neighbors (KNN)	85.9% with KNN
Pominova et al. 2021 [163]	ABIDE II	184	168	10.15±2.98	FC matrices	3D convolutional autoencoders	—
Yin et al. 2021 [164]	ABIDE I	403	468	n.s.	ROI-based FC matrix	Autoencoders CNN DNN	79.2%
Chu et al. 2022 [165]	ABIDE	79	105	14.51±6.23	FC network regions	multi-scale GCN	0.795
Yang et al. 2022 [166]	ABIDE I	403	468	6-58	FC matrix	LR, SVM, DNN	69.43%

3 Limitations of Current Approaches

After reviewing the key accomplishment in literature towards autism diagnosis, we conclude a number of limitations that indicate the need for more work:

- Limited explainability: Many high-performing models completely relied on black-box modules, such as CNN and DNN, which is less desirable in the medical field. Clinicians do not trust these models because, while they are successful at classifying, they often lack any clinical context, therefore, they are not trusted for their judgments.

- CAD systems designed utilizing task-based fMRI are not suited to use for diagnosing children of early age, as they may introduce additional biases.

- There were many studies that included small clinical datasets, making it difficult to replicate and improve upon those methodologies, with limited power of a study.

- Not much work is present on the crucial feature representation, reduction, and feature engineering techniques, despite their effect on any ML framework.

- Little effort is done comparing different preprocessing strategies and explaining the reasons behind each choice. From a research point of view, it is more important to provide a thorough study answering questions than just some distinct results.

In this dissertation, we aim to land up with outlining some of these limitations and developing a unified framework for autism diagnosis using ML that is explainable, expandable, and scalable.

CHAPTER III

USING DTI FOR AUTISM DIAGNOSIS: INTRODUCING A NOVEL FEATURE REPRESENTATION

The aim of this chapter is to present our automated computer-aided diagnostic (CAD) system for the accurate identification of autism based on the connectivity of the white matter (WM) tracts. To achieve this goal, two levels of analysis are provided for local and global scores using diffusion tensor imaging (DTI) data. While most of the previous work relied on sMRI and/or fMRI, the focus of our work is using DTI. A local analysis using Johns Hopkins WM areas' atlas is exploited for DTI atlas-based segmentation. Furthermore, WM integrity is examined by extracting the most notable features representing WM connectivity from DTI. Interactions of WM features between different areas in the brain, demonstrating correlations between WM areas were used, and feature selection among those associations was made. Finally, a LOSO classifier is employed to yield a final per-subject decision. The proposed system was tested on a large dataset of 263 subjects from NDAR database with their Autism Diagnostic Observation Schedule (ADOS) scores and diagnosis (141 typically developed: 66 males, and 75 females, and 122 autistics: 66 males, and 56 females), with ages ranging from 96 to 215 months, achieving an overall accuracy of 73%. In addition to this achieved global accuracy, diagnostically-important brain areas were identified, allowing for a better understanding of ASD-related brain abnormalities, which is considered an essential step towards developing early personalized treatment plans for children with autism. The work in this chapter was published partially in © 2020 IEEE, from [167].

1 Introduction

Previous neurobiological studies investigated connections between ASD and underlying structure, trying to describe brain abnormalities associated with autism traits. Since the emergence of MRI, plenty of studies appeared to investigate connections between ASD and underlying brain features, either shape and volume features using structural MRI [7], or white matter (WM) diffusivity [49] anomalies using DTI, while others performed correlations of ASD with either task based or resting state functionality [48] using functional MRI (fMRI). In this work, we will introduce our DTI-based algorithm for assessing ASD with the help of ABIDE-II dataset.

DTI is gaining rising popularity over the past couple of decades, especially for brain-related disorders, as it provides a non-invasive way of characterizing the connective tracts inside the brain between different areas. It quantifies the diffusion patterns inside the white matter (WM). White matter mainly consists of axons of neurons (nerve fibers), and with the human brain containing hundreds of billions

of neurons, the structure of WM is truly complex. The WM represents the axonal fibers carrying neural signals between various brain regions and between the brain and spinal cord through the brainstem. The organization of such a complex network contains a wealth of information, still, current resolution for conventional MRI technologies cannot capture such small details that are typically less than a micrometer to only few micrometers. Yet, DTI provides diffusion measures that gives information about the tractography of the brain. DTI's most used parameters [45] include fractional anisotropy (FA), mean diffusivity (MD), and sometimes also "radial" and "axial" diffusivities. These parameters actually describe the diffusion of water inside the brain, and since water diffusion is restricted outside of fiber tracts, this translates into indirect information of micro-structure and connectivity of WM [46]. Additionally, some derived features are also used to characterize other diffusion measures in WM tracts, such as tensor trace, skewness, rotational invariance, and many others [47]. Abounding previous literature noted WM abnormalities associated with autism, often as differences in WM micro-architecture across some local brain areas. For instance, differences in FA values were reported by Wolff et.al. [168] between ASD and typically developed (TD) infants. In autism, numerous studies suggest abnormal development of neural networks that manifest themselves as abnormalities of brain shape, functionality, and/ or connectivity. As concluded from similar investigations reviewed in chapter II, neither the under-connectivity nor the over-connectivity of the brain hypothesis can successfully describe the deviations of the ASD population alone [169]. Despite the numerous efforts to detect autism-related variations using imaging, there is no robust, effective CAD system that is able to both diagnose autism and place them within a severity spectrum. This is what originated the idea of using DTI in order to develop an extensively automated diagnosis system that can help clinicians identify subtypes of the disorder and develop personalized treatment plans for individuals with autism. The rest of this chapter will be organized as follows: section2 will describe all materials and methods used, section3 will provide the achieved experimental results, while section4 will present the discussion of the results.

2   Materials and Methods

The primary objective of this chapter is to extract informative local white matter features for each brain area that can be used to discriminate an autism diagnosis. Fusing the results of those local associations would help obtain an accurate global diagnostic decision per subject. The framework mainly consists of three stages: first, a preprocessing step is carried out to reduce imaging artifacts and eliminate non-brain tissues. The second stage is feature calculation, extraction, and selection, including the use of an atlas-based segmentation technique to allocate features for each area. The third stage is a classification step that is used for obtaining the final diagnosis, as well as identifying specific brain areas that offer the best help to differentiate ASD from neurotypical. Details of the proposed framework as well as experimental results are discussed in the next sections.

White Matter Connectivity Analysis:

For each subject, the white matter was studied using diffusion tensor imaging (DTI) information. In DTI, a 3×3 diffusion tensor describes the diffusion of water within the volume of tissue contained in each voxel. To find the principal diffusion directions, the 3 eigenvalues λ_1, λ_2, and λ_3 and their corresponding eigenvectors v_1, v_2 and v_3 are calculated, where the eigenvector corresponding to the largest eigenvalue is the principle diffusion direction (i.e, diffusion across the fiber) while the other two eigenvectors correspond to the radial diffusion directions (i.e, diffusion perpendicular to the fiber) as illustrated in Figure 3 [21].

A special case is an isotropic medium, where the diffusion ellipsoid takes the shape of a sphere where $\lambda_1 = \lambda_2 = \lambda_3$. In the case of an anisotropic medium, the diffusion is represented as an ellipsoid as shown pointing in the v_1 direction of λ_1. There are six output features obtained from DTI that are the most commonly used anisotropy measurements describing white matter connectivity:

1. Fractional Anisotropy (FA): The most widely used measurement of anisotropy, a scalar value between 0 and 1 that determines the diffusion integrity. As FA approaches 0, the diffusion is considered to be isotropic while higher values mean that the diffusion tends to be in a uniform direction (i.e, the principal eigenvector direction) [21, 170].

2. Mean diffusivity (MD): Average diffusivity within a voxel, integrated over all directions, independent of the direction. $MD = \frac{1}{3}(\lambda_1 + \lambda_2 + \lambda_3)$.

3. Axial diffusivity (AD): Diffusivity in the direction of the major axis of the diffusion ellipsoid, $AD = \lambda_1$.

4. , 5. Radial diffusivity in the direction of the minor axes of the diffusion ellipsoid: λ_2 and λ_3 .

6. Skewness: a 3rd order measurement characterizing the shape (oblate or prolate) of the diffusion tensor, which is not captured by FA or other lower order measurements [47]. $Skewness = \frac{(\lambda_1 - MD)^3 + (\lambda_2 - MD)^3 + (\lambda_3 - MD)^3}{3}$.

In the work of this chapter, FSL toolbox `https://fsl.fmrib.ox.ac.uk` was used for DTI computation. The eddy current correction [171] and brain extraction using BET algorithm [172, 173] were applied prior to calculating the diffusion tensor. Fig. 5 shows an example of the tensor visualization.

The calculated features are then aggregated over the 48 local regions defined by Johns Hopkins WM atlas parcellation [174] using DTI-TK software. The atlas-based segmentation task is elaborated in the next subsection. Finally, the rest of the proposed algorithm is implemented in Matlab.

Brain parcellation into local brain areas:

After calculating the above metrics at each voxel, it is useful to aggregate them by region according to an appropriate brain parcellation. An atlas-based segmentation
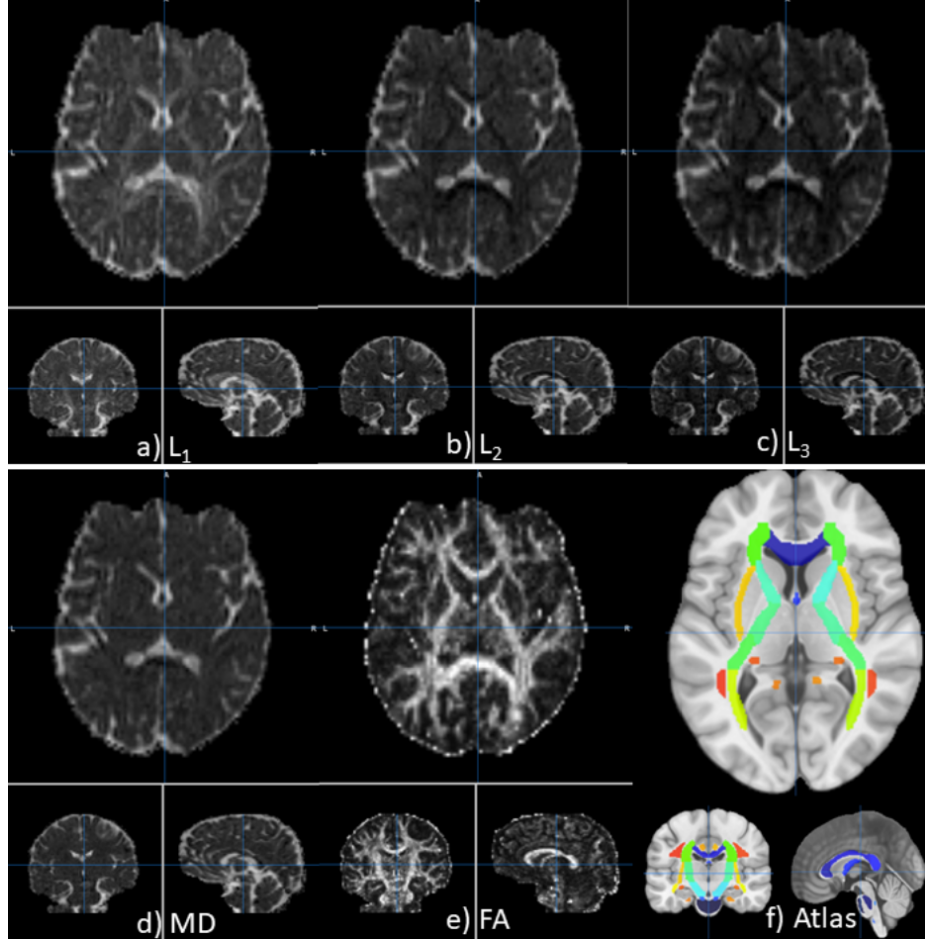
Figure 5. Example of extracted features from one subject DTI brain, (a) Axial diffusivity λ_1 , (b) Radial diffusion λ_2, (c) Radial diffusion λ_3, (d) Mean Diffusivity MD, (e) Fractional Anisotropy FA, (f) Labeled WM areas of John Hopkins Atlas, each color identifies here different WM area.

approach is adopted, where we treat the area's segmentation problem as a registration task. In this step, Johns Hopkins WM atlas [174] along with its labeled areas are used. John Hopkins is an ICBM coordinate-based WM atlas that defines 48 brain areas that were hand segmented from 81 different subjects. A registration from the MNI atlas space to each subject's space using DTI-TK software [175] is performed, as it supports interoperability with FSL. After atlas-subject registration, an affine transformation is applied to JHU atlas labels, providing WM areas masks for each subject. Thus, we can get local features for each WM area that are used at the local classification level. Fig. 6 shows the entire diagnosis pipeline. The main advantage of this technique is that it is scalable, automated, and has high accuracy.

Feature selection:

The above-mentioned procedures provide 6 features (FA, MD, λ_1, λ_2, λ_3, and Skewness) for each voxel, per each subject. All of those are raw values per voxel, some
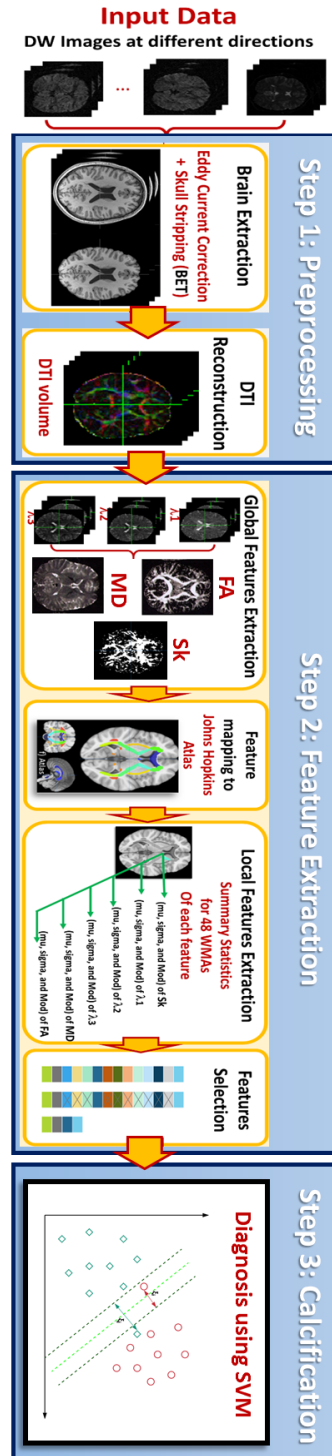
Figure 6. DTI experiment pipeline, where the brain is extracted, preprocessed, features calculated, atlas-based segmentation performed, and selected features are incorporated for final classifiers.
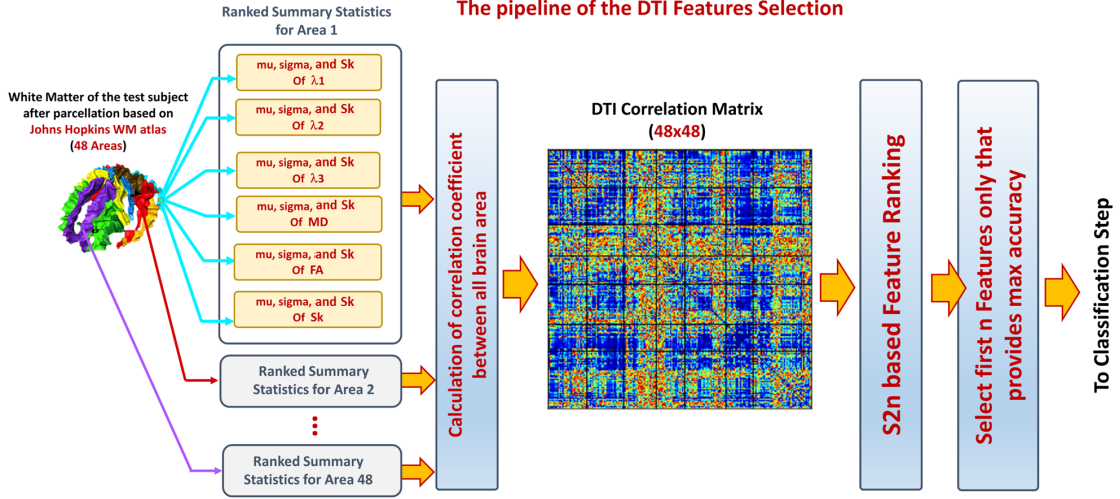
Figure 7. DTI feature extraction procedure

vectors are tens of thousand in length per area. To provide a compact representation, we calculate short summary statistics vectors (mean $[\mu]$, standard deviation $[\sigma]$, and skewness $[E(x - \mu)^3/\sigma^3]$) for each area. Then, we concatenate those summary statistics resulting in a feature vector of length 18 per each area (6 feature types $\times$ 3 summary statistic vector length). Instead of using those direct features, we derive new ones capturing the implicit relationships between different brain areas' values, calculated as the correlation between the feature vectors of each two areas. We reduce this huge feature space(48×48 per subject), relative to the sample size (263 subjects), by extracting only the important discriminatory features, to build our diagnosis algorithm. For this purpose, we used a simple filtering method known as the signal-to-noise ratio (s2n) filter [35]. In this method, we rank each feature based on a score representing the ratio between the absolute difference of the means of the two classes and their variance. Fig. 7 illustrates the adopted feature selection technique. Then, we use only the highest-ranking features in the next steps.

ASD Diagnosis

Having pairwise correlated the DTI metrics of WM regions, each of the resulting features, i.e. each region pair, was used separately to distinguish between ASD and TD subjects on the global level. The contribution to the diagnostic accuracy of each feature incorporated into the classifier is shown, highlighting those that were most relevant to autism. A number of classifiers from diverse classifier algorithms were tested, including Support Vector Machine, k-Nearest Neighbor (KNN), decision trees, neural networks (NN), and deep NN with auto-encoders. Experiments found the best performance in terms of cross-validated accuracy and processing time for Support Vector Machine (SVM). Linear SVM classifiers were used on each classification level, taking correlation features as inputs and producing a normalized score (0–1) indicating the confidence that a subject is autistic given the WM areas for which information was provided. Of course, not all areas are expected to contribute significantly to the de-

cision between ASD and TD, so only the first n features are used for classification, where n is determined empirically. Algorithm 1 shows the steps of the implemented technique, and Fig. 6 shows the pipeline of the entire diagnostic framework.

Algorithm 1 DTI-based ASD diagnosis system

 1: ∀ **dwMRI subject's data** :
 2:     1. run preprocessing modules:
 3:         i) Eddy Current Correction
 4:         ii) Apply brain mask generated by Brain Extraction Tool
 5:     2. Feature Calculations:
 6:         i) Use FSL to calculate DTI Tensor, scale units, calculate $\lambda_1, \lambda_2, \lambda_3$, FA, MD, SK volumes
 7:         ii) Register DTI MNI space IIT Human Brain Atlas to each subject using DTI-TK
 8:         iii) Apply resulted transformation on the JHU atlas labels
 9:         iv) Use registered labels to extract features per each WM area
10:         v) Calculate summary statistics (μ, σ, *Skwns*) for each area for each feature, rank feature values across the different 48 brain areas, get feature vector.
11:         vi) Calculate correlations between feature vectors of each two areas
12:         vii) Use s2n filter to rank correlation-features
13:     3. Classification:
14:         i) iterate on n from 1 to 250.
15:         ii) Feed first n ranked ordered feature for all subjects to an SVM classifier
16:         iii) Give a final diagnosis for each subject, whether TD or ASD
17: **End**.

---

3   Experimental Results

Data for this experiment were obtained from the National Database for Autism Research (NDAR) [176]. De-identified diffusion MRI data were accessed, comprising 263 subjects (131 females and 132 males). Of these, 122 had a diagnosis of ASD, confirmed with ADOS, while the other 141 individuals did not have any pervasive developmental disorder. The subjects were between 8 and 18 years of age at the time of MRI acquisition. Table 2 shows the summary age/sex proportions of the used subjects.

To ensure system robustness, we used leave-one-subject-out (LOSO) cross validation at all runs. For each WM area, overall accuracy, sensitivity, and specificity were calculated. Obtaining a subject's global diagnostic decision is a two-step procedure. First, features are ranked based on the s2n score, then iteratively first n is fed to the next step, with n starting from 1 to 250. Selected features are concatenated, and SVM classifiers are used to make a decision about whether ASD or TD based on the concatenated feature vector, providing a single global decision per subject. The optimal classifier achieved an overall diagnostic accuracy of 73%, 70% sensitivity, and

Table 2. Age Summary Table of the 263 NDAR subjects used in this chapter, showing sex counts (M: male, F: female), age at scan in years (when available).

	ASD Group (n=122) M = 66, F=56	TD Group (n=141) M = 66, F = 75
count	122	102
mean	12.74	13
std	2.86	2.96
min	8	8.08
max	17.9	17.92

Table 3. Top ten pairs of white matter areas whose feature-vector correlations provide separability with the highest rank according to s2n filter. Regions represented in both hemispheres are annotated with L (left) or R (right) if only one hemisphere is involved, or with B (bilateral) otherwise.

Rank	Area 1	Area 2
1	Superior longitudinal fasciculus R	Anterior corona radiata R
2	Body of corpus callosum	Genu of corpus callosum
3	Superior longitudinal fasciculus R	Sagittal stratum
4	Tapetum L	Middle cerebellar peduncle
5	Splenium of corpus callosum	Middle cerebellar peduncle
6	External capsule L	Middle cerebellar peduncle
7	Cingulum L	Corticospinal tract R
8	Stria terminalis R	Superior corona radiata L
9–10	Superior longitudinal fasciculus L	Posterior corona radiata B

76% specificity. This performance was achieved using $n = 79$ correlations. The most significant of these region pairs are listed in Table 3.

4   Chapter Discussion

The most important regional correlations for distinguishing ASD from control (Table 3) are a diverse group, but they fall into five categories. First is the middle cerebellar peduncle (mcp) as it correlates with the splenium of the corpus callosum, the left external capsule (ec), and the left tapetum. The uncinate fasciculus is a fiber pathway through the ec, which links the ventral frontal cortex, in particular Brodmann areas 11 and 47, with the temporal pole [177]. Commissural fibers of the left temporal pole, and of the temporal lobe in general, pass through the left tapetum on their way to or from the splenium. The mcp on the other hand carries signals from the cerebral cortex and subcortical regions, via the pontine nuclei, into the cerebellar cortex.

Next are correlations between the superior longitudinal fasciculus (SLF) on the right hemisphere with ipsilateral sagittal striatum (SS) and anterior corona radiata (CR), and between SLF in the left hemisphere with bilateral posterior CR. The SLF is

a bidirectional pathway along the anterior-posterior direction through which different lobes communicate with each other [178]. Thalamocortical fibers pass through the SS and CR, where they intermingle with callosal axons [179]. In this category as well as the first, we see in ASD a difference in the microstructure of cortico-cortical pathways *relative to* pathways linking the cerebral cortex with outside regions.

Output from the left motor cortex passes through the corticospinal tract on the opposite side. Communication between left motor and premotor areas meanwhile makes use of pathways through the left cingulum. The middle segment of the cingulum would be involved in particular; however, the atlas used in this chapter does not parcellate the cingulum further, so we were only able to identify altered correlation between the left cingulum as a whole and the right corticospinal tract. Still, this once again suggests changes in a cortical area's connectivity with elsewhere in the cortex *vis-à-vis* regions outside the cortex.

The superior CR contains sensorimotor fibers of the posterior frontal/anterior parietal cortex. The microstructure of this region by itself has been found to differ between ASD and typically developing children [180]. The stria terminalis contains efferent fibers from the amygdala, which terminate in several nuclei of the hypothalamus and regulate the stress response. We might hypothesize that the increased stress response seen in ASD [181] is normal hypothalamic activation triggered by abnormal sensory processing. While the differences in the superior CR found by Pryweller and colleagues [180] were more pronounced in the left hemisphere, statistical testing did not find this significant. Nor was there any significant distinction between superior CR and other sensory processing pathways they investigated; all showed increased apparent diffusivity in ASD. It is not clear why in this study the left superior CR, relative to stria terminalis, particularly stood out.

Differences in the microstructure of the genu and body of the corpus callosum relative to each other are harder to interpret, given that they are complementary parts of the same structure, containing commissural fibers from distinct regions of the cortex. It may be of significance that the sections of the corpus callosum develop at different gestational ages. The axons forming the genu grow first, starting in the twelfth or thirteenth week of gestation, followed by the body and splenium in anterior-posterior order, and finally the rostrum [182]. Could this be a clue to pinpointing the developmental stage at which the propensity for developing ASD originates?

There remain several challenges to address and potential enhancements to be made with regard to this system. In particular, while the LOSO approach is an efficient means to maximize the data available for machine learning and still obtain reasonable estimates of classification accuracy, testing on an independent data set is necessary to demonstrate the classifier's ability to generalize. Also, analysis of clinical and cognitive-behavioral data, beyond the diagnosis of ASD or non-ASD, is needed to map the affected brain to specific ASD symptoms. The differences in regional correlations we have found so far will be useful for constructing testable hypotheses in that regard. Though many registration tools were tested on the bulk of the data set, a WM area parcellation tailored to the individual (e.g., using tractography) could lead to better feature extraction and hence improved performance.

The next step for our CAD implementation will be to incorporate different imaging

modalities, such as structural or functional MRI. In this way, the CAD system will be able to relate WM microstructure with brain shape (e.g., cortical folding), and structural connectivity with functional connectivity. Expanding the feature space in this way might enhance classification accuracy and provide a better understanding of symptoms and personalized diagnosis.

CHAPTER IV

THE ROLE OF DTI IN AUTISM DIAGNOSIS: A COMPREHENSIVE APPROACH

This chapter provides a thorough study of implementing feature engineering tools to find discriminant insights from brain imaging of WM connectivity and using a ML framework for the accurate classification of autistic individuals. The work highlights important findings of impacted brain areas that contribute to autism diagnosis and presents promising accuracy results. We verified our proposed framework on a large publicly available DTI dataset of 225 subjects from the Autism Brain Imaging Data Exchange - II (ABIDE-II) initiative, achieving a high global balanced accuracy over the five sites up to 99% with 5-fold cross-validation. The data used was slightly unbalanced, including 125 autistic subjects, and 100 typically developed (TD) ones. The achieved balanced accuracy of the proposed technique is the highest in the literature, which elucidates the importance of feature engineering steps involved in extracting useful knowledge, and the promising potential of adopting neuroimaging for autism diagnosis. The work in this chapter was published partially in [10].

1 Background

Up till now, most of the published work towards classification used ABIDEI, and very few used newer ABIDEII data [78, 127, 183, 184]. One study used one site of ABIDE-II only (San Diego State University cohort), and employed both fMRI and DTI imaging modalities using connectome features, accomplishing an accuracy of 72% [82]. We emphasize that the need of using more than one modality implicates added cost and visits' scanning time. Another key contribution of this work is finding a best-fit dimensionality reduction technique. Having a very large feature space (p) with limited sample space, subjects in our case (n), is commonly known as the curse of dimensionality [30], which causes increased complexity of the models that easily results in overfitting, with less learning captured by the model. This phenomenon is very common with MRI imaging and medical data where we have piles of data fields for a few patients and sometimes is not handled correctly. While the standard way to handle those data is by exploiting some sort of feature reduction algorithms, such as linear discriminant analysis (LDA) [32], principal component analysis (PCA) [31], or auto-encoders [33]. The common shortcoming is that they usually do not keep the interpretation of the original feature in the new feature space, making it hard to explain clinical connections for any classification decision, making it less attractive for practical medical use. The feature reduction method needs to help clinicians make an informative decision, and aid in understanding the pathological abnormalities of the brain of autistic subjects. Our work investigates the recursive feature elimination

(RFE) technique, which recursively eliminates the least contributing features to classification till ending with the best subset. We extensively carried out a plethora of experiments to reach a near-optimal configuration that led to the best classification validated on our dataset.

Despite the numerous studies of autism-related changes in white matter integrity, the objective of this work is to implement a comprehensive ML-CAD system that, besides its ability to classify ASD vs TD subjects, identifies brain areas correlated with autism, and was validated on a big publicly available dataset, using DTI data. The proposed algorithm employed a thorough feature selection using recursive feature elimination with cross-validation (RFE-CV) using four different kernels (SVM with the linear kernel (LSVM), random forest (RF), logistic regression (LR): either with l_1-norm (LR1), or LR with l_2-norm (LR2)), and performed hyper-parameter optimization on eight different classification techniques. The best candidate configurations were validated using random splits of different k-folds cross-validation to identify the global ML model alongside the global imaging bio-markers associated with ASD. Our main motivation behind this work is to present a reliable system that can help physicians better understand individuals with autism allowing earlier and more personalized treatment plans. The rest of this chapter is organized as follows: section 2 presents the details of the pipeline of the proposed algorithm, while the experimental results are introduced in section 3 for ABIDE-II diffusion MRI data. Finally, section 4 provides a discussion and conclusions of the chapter.

2   Materials and Methods

A visualization of the pipeline of the whole framework is presented in Fig. 8. It starts with pre-processing of each subject's input volumes, then DTI parameters calculations, feature extraction, and mapping to a WM atlas to get local features, then using two different feature representations to be used in feature selection and classification steps. The following subsections provide details of those multi-stage processes until reaching a final diagnosis.

Data used

The study in this chapter utilized DTI data from Autism Brain Imaging Data Exchange (ABIDE) II dataset. ABIDE-II is a recent publicly available dataset, that aggregates MRI data (sMRI, fMRI, and DTI) for autism studies across different multiple sites. ABIDE-II contains data from around 19 sites, for more than 1000 subjects, half of which are autistic individuals. Working on a publicly available dataset facilitates replicating results and increases the reliability of our findings. ABIDE-II is considered a large dataset, which increases the power of our study. We selected datasets that involved DTI data, which were 6 datasets: namely: Barrow Neurological Institute (BNI), NYU Langone Medical Center 1 (NYU1), NYU Langone Medical Center sample 2 (NYU2), San Diego State University (SDSU), Institut Pasteur and Robert Debré Hospital (IP), and Trinity Centre for Health Sciences (TCD). IP DTI data bvals (diffusion gradient strength per volume values) and bvecs (diffusion gradi-

ent directions per volume values) were missing a value, so we excluded it, and used the remaining five sites. Those five sites originally had 284 subjects with DTI imaging data, and ended with 225 subjects of them after cleaning, on which we applied the steps of our pipeline as we will elaborate on the next subsections.

Pre-processing

Input image preparation

After deciding which sites to work on, we downloaded its available data which came organized as folders labeled by subject ID containing imaging data. We located subjects that have DTI data, copying the image nii file along with its bvals and bvecs to the working directory to be pre-processed.

Skull stripping

The goal of skull stripping step is to remove non-brain tissues (eg: skull, scalp, dura, ..) from the image volumes, extracting only the brain. This automated process was implemented using the brain extraction tool (BET) algorithm [172] from FSL tools, generating the binary masks and using default parameters with a fractional intensity threshold of 0.25.

Eddy current correction

Eddy currents are induced currents due to gradient fields in the x, y, and z directions, that result in visible image artifacts, that usually blur the boundaries between gray and white matter. Diffusion-weighted imaging is usually affected by this phenomenon and eddy current correction step is commonly implemented. For this purpose, we used the eddy current correction tool available through FSL [171] to correct for both common artifacts: adjust for induced currents, and also for subject movement during the scan across sections.

Feature Calculation

After having the diffusion-weighted volumes cleaned of non-brain tissues and common artifacts, we run DTI calculations to get DTI diffusion tensor, its eigenvalues, and other metrics. For each voxel, diffusion can be represented by a 3 by 3 tensor, that describes the diffusion pattern at each point, in the 3D space. From this tensor, more common metrics, namely eigenvalues, are used to represent the magnitude of diffusion along 3 major perpendicular directions of its eigenvectors. The largest eigenvalue, λ_1, along with its eigenvector v_1 represent the magnitude and direction of the primary direction of diffusion (along the fiber tract), while the other two represent radial diffusion perpendicular to the main one [21]. Other derived metrics, such as fractional anisotropy, mean diffusivity, skewness, and many other are commonly used to represent other characteristics of the diffusion. Similar to the previous chapter, we included the following six metrics to describe our white matter micro-architecture:

Table 4. Demographics Summary Table of the 225 subjects used in this chapter, showing sex counts (M: male, F: female), age at scan in years, and full-scale IQ (FIQ).

	ASD Group(n=125) M=104, F=21		TD Group (n=100) M=76, F=24	
	AGE	**FIQ**	**AGE**	**FIQ**
count	125	119	100	74
mean	11.91763	102.02521	16.41717	111.90541
std	5.302605	18.251753	8.994877	15.341026
min	5.128	49	5.887	71
max	34.76	143	46.6	144

i) Fractional anisotropy (FA), ii) Mean diffusivity (MD), iii) Axial diffusivity λ_1, iv) Radial diffusion λ_2 , v) Radial diffusion λ_3 , and vi) Tensor skewness $TSkew$. For the first five features, dtifit tool, part of FSL package, was used to calculate the diffusion tensors along with eigen values, eigen vectors, FA, and MD. Tensor skewness (Tskew) was calculated using Matlab 2021a, as it was not provided through the previous tool. At this point, each subject is represented by six volumes, each comprising hundreds of thousands of raw voxel values.

Data cleaning

In the previous parts of the pipeline, some subjects failed during volume sizes validation/ BET/ DTI calculations/ or regional feature extraction, either with an error in the prepossessing or yielding a non-complete brain, identified by having more zero values "blanks" than it should. Excluding those subjects from further processing, we ended up with 225 subjects that will be used for the rest of this chapter. Summary of demographics for all subjects used in this study: age, full-scale IQ, and gender, are provided in Table 4.

Atlas-based segmentation

Having each subject represented by its six-volumes per voxel features, now we need to assign those features to local brain areas. For this purpose, the white matter atlas ICBM-DTI-81 defined by Johns Hopkins University [174], is used. JHU ICBM-DTI-81 WM atlas uses ICBM coordinates and defines 48 white matter areas. Those areas were originally hand-segmented from an average diffusion MRI tensors of different 81 subjects. To locate local anatomical regions in each subject space, we implemented an atlas-based segmentation approach, where we performed atlas registration for area localization. Registration from the atlas space to subject's space was performed in two iterations, a rigid transformation then an affine transformation. The objective of the rigid registration in the first iteration is just to find an initial alignment, not changing size or shape, that will be used for next step. Then, an affine transformation is found to improve upon the initial estimation providing a higher degree of freedom for a more generic linear transformation that enables object's size and shape to be adjusted.

This two-step registration task was implemented using DTI-TK software [175], both using normalized mutual information measures with $4mm \times 4mm \times 4mm$ sampling distance and 1% tolerance. DTI-TK also enables interoperability with FSL software used in preprocessing. The found transformation was then applied to atlas labels, hence providing WM areas masks at each subject space. Those masks were used to define local features for those 48 areas. This segmentation technique provides a fast automated solution, enabling easy application to new subjects or datasets, with less error.

Feature representation

At this point, each subject is represented by six features per 48 areas. Each of those features is a per-voxel raw feature, and their length, in tens of thousands, varies between areas. The first step is to convert those raw features into a better representation with the goal of reducing the number while keeping the most important aspects capturing underlying information. For this purpose, we replaced per-voxel features of each area with three summary statistics of the underlying distribution, namely, mean(μ), standard deviation (σ), and skewness (sk), where μ aims to capture central tendency, σ capturing dispersion of values around this mean, and sk to measure of the asymmetry of the data around this mean. At the end of this step, our feature matrix F, for each subject i, can be represented as a 48 by 18 matrix as follows:

$$F_i = \begin{bmatrix} \mu_{FA_1} & \sigma_{FA_1} & sk_{FA_1} & \cdots & sk_{Tskew_1} \\ \mu_{FA_2} & \sigma_{FA_2} & sk_{FA_2} & \cdots & sk_{Tskew_2} \\ \vdots & \vdots & \vdots & \ddots & \vdots \\ \mu_{FA_{48}} & \sigma_{FA_{48}} & sk_{FA_{48}} & \cdots & sk_{Tskew_{48}} \end{bmatrix}$$

where F_i is the feature matrix for subject i using the first feature representation described above. Each element in this matrix is a summary statistic (baseline: μ/ σ / sk) for one of the six features (subscript: FA/ MD/ ..Tskew) for an area from 1 to 48 (sub-subscript index).

Feature engineering

Instead of directly using per-area summary statistics features, we developed an enhanced representation that captures latent relative relationships between brain areas. We calculated the Pearson correlation coefficient between each pair of brain areas l, m, and use this correlation matrix as our feature matrix. So, for each subject i, $\rho_{l,m} = corr(F_i(l, :), F_i(m, :))$ Although this step increased the number of features per subject slightly [from 48*18 = 864 to (48 * 47 / 2)=1128], it helped in boosting the performance of the classification, as we will see in the results. This novel representation, using interactions, is considered a key contribution that helped in improving the performance. The new second feature matrix F_{2_i} for subject i is now represented

by:

$$F_{2\_i} = \begin{bmatrix} \rho_{1,1} & \rho_{1,2} & \cdots & \rho_{1,48} \\ \rho_{2,1} & \rho_{2,2} & \cdots & \rho_{2,48} \\ \vdots & \vdots & \ddots & \vdots \\ \rho_{48,1} & \rho_{48,2} & \cdots & \rho_{48,48} \end{bmatrix}$$

where each element in this matrix $\rho_{i,j}$ is a correlation between the summary statistics vectors of the two areas i, j. We highlight that only the upper triangle (U) of this new feature matrix (or lower L, because of symmetry), is used in subsequent steps, as the rest is redundant because of symmetry. Serializing those 1128 features, we can represent the final feature matrix, for all of 225 subjects, as $\hat{F}$, with size 225×1128, where each row is the concatenated calculated correlations for one subject. Fig. 8.b illustrate those steps. In addition to the data matrix, we have another column vector y denoting the labels of each subject, whether ASD ($y_i=1$) or TD ($y_i=0$).

$$y = \begin{bmatrix} y_1, & y_2, & y_3, & \cdots, & y_{225} \end{bmatrix}$$

Feature reduction: RFE-CV

The feature space (1128 correlations) is quite large relative to our sample size (225 subjects). As we discussed earlier, the number of features relative to number of subjects needs to be reduced, keeping the most informative feature. While many feature reduction techniques, such as linear discriminant analysis, principal component analysis, or autoencoders, can perform this task, they transform the feature space into a new one that does not preserve the meanings of the original features. Building classification systems based on those new ambiguous features would sophisticate the ability to understand any clinical reasoning of classification results. Hence, making it less beneficial and reasonable to physicians in generating an informative decision, or understanding the underlying pathological abnormalities of an autistic brain. We employed the recursive feature elimination (RFE) technique, where only a subset on features is selected. RFE is a feature selection algorithm based on feature ranking with recursive feature elimination. The principle behind RFE is fitting a classification model, ranking the features by the model's scoring, then eliminating the weakest features recursively to find the optimal number of features to be selected. Cross-validation is used with RFE (RFE-CV), where data is split into k-folds, the score features based on different data subsets, then select the best scoring across the k-folds. The target optimization scoring metric (whether accuracy, balanced accuracy, f1, weighted f1, precision, recall, ...) can be specified, and we used here balanced accuracy with k=10 folds for optimization. The algorithm then finds the optimal n significant features to be selected that maximize the average classification performance according to the target metric [185, 186]. To find the best architecture of RFE-CV that best fits our problem, we tested four types of RFE-CV classifiers as kernels, namely linear SVM (LSVM), Random Forest (RF), Logistic Regression (LR) with l_1-norm (LR1), and LR with l_2-norm (LR2), on the two feature representation we have (original summary statistics F_i of 225×864 and correlations F_{2_i} of 225×1128).
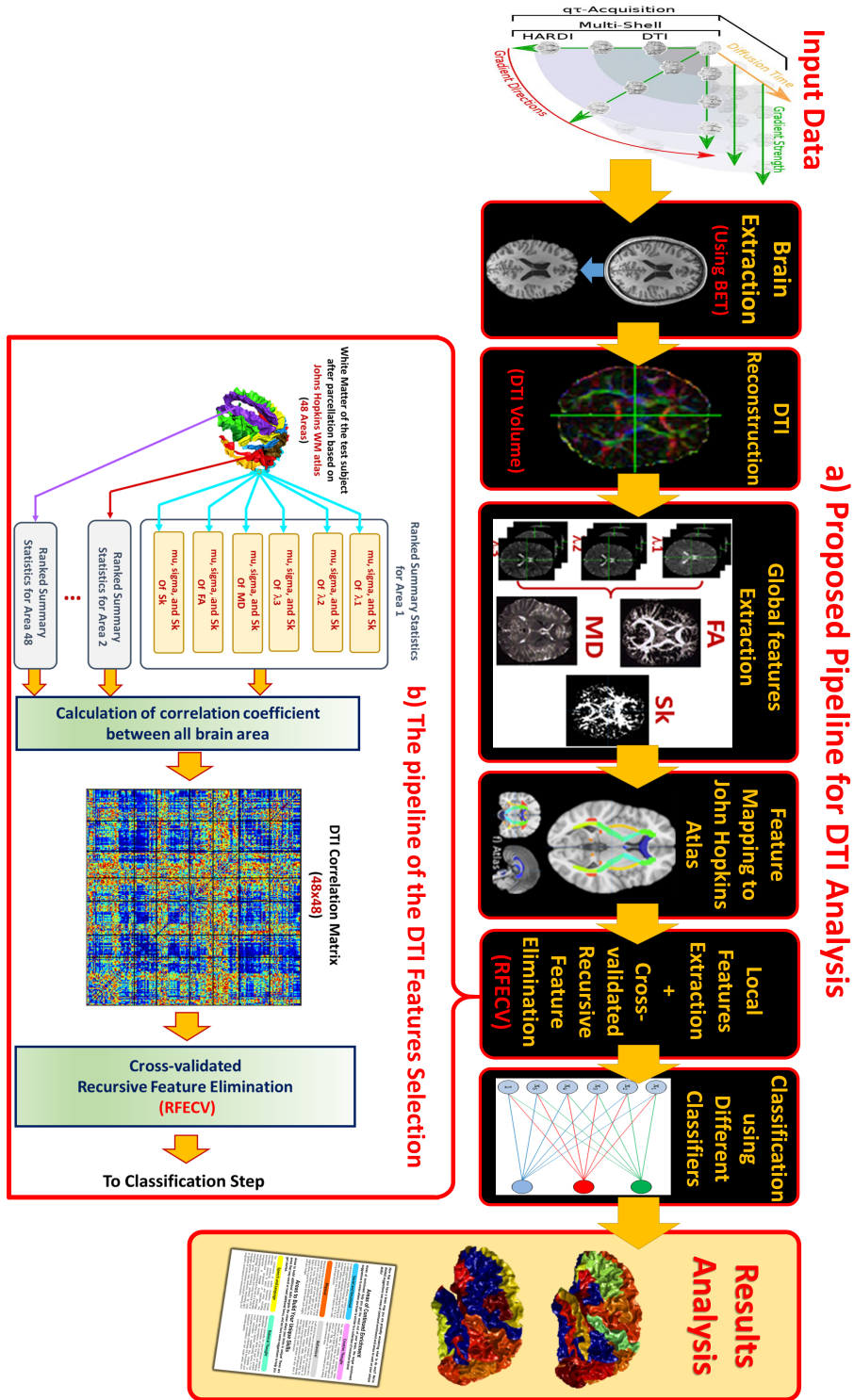
Figure 8. a) Pipeline of the DTI-diagnosis algorithm, b) Usage of new derived feature representation $\hat{F}$ and feature selection before classification.

Thus, we got estimates using four different models, each selecting features according to its classifier independently, and providing average cross-validated scores for 10-folds, then we evaluate the performance of eight models to select which model to use for further processing.

Classification

After having n selected features for each of 8 models, representing the top prominent features for distinguishing autistic brains, we set up a system of machine learning classifiers. We tested eight different classifier types, and performed hyper-parameter optimization for each one to end up with the best parameters-classifier model, in terms of accuracy. We included both linear and non-linear classifiers to test both types of relationships between the two classes. The set of used classifiers are: 1) Linear SVM (LSVM), 2) Logistic Regression (LR), 3) Passive Aggressive classifier (PAGG), 4) SVM with Radial-basis kernel (RBF-SVM), 5) Gaussian Naive Bayes (GNB), 6) Random Forest (RF), 7) XGboost (XGB), and 8) Neural Networks (NN). 1-3 are linear classifiers, while the rest are non-linear ones. 6-7 are ensemble-based classifiers, and for NN we included both shallow and deep configurations in our hyper-parameters search. For hyper-parameter optimization, after we selected only n features according to the previous RFE-CV step, we tested a set of different parameters with different ranges for each classifier. For this purpose, the input data is split into five folds, to determine the best performance according to the average across those 5-folds. So, for each classifier, using selected features only: i) split data into 5-folds, use 4 for training and one for testing each time, and for each parameter configuration, store the performance of the classifier for each fold. ii) balanced accuracy scoring is used to decide on the best configuration. iii) the best-performing classifier is selected, and the hyperparameters along with its maximum average cross-validated score, and also standard deviation over folds, are highlighted. Table 5 show the set of used hyper-parameters in the search associated with each classifier and their ranges. Algorithm 2 illustrates a step-by-step guide of the fully implemented algorithm, and Fig. 6 summarizes a graphical illustration of the pipeline of the entire system.

3 Results

As discussed in the data subsection, ABIDE-II dataset [187] was used for testing and validation of the above-mentioned methodology. ABIDE-II [187] which provides hundreds of subjects' brain imaging data (structural MRI, functional MRI, and DTI) to enhance the research in Autism Spectrum Disorder (ASD). DTI data used are only from the five sites: (IP, NYU1, NYU2, TCD, and SDSU. Diffusion-weighted MRI (dwMRI) scans for a total of 225 subjects are used: 125 ASDs and 100 TDs, with age, ranges between 5.128 years and 46.6 years.

The four types of RFE-CV kernels (LSVM, LR1, LR2, and RF) were used to select features from the two different representations (summary statistics F, and correlations $\hat{F}$), and those features were used to train and test eight types of classifiers (LSVM, LR, PAGG, RBFSVM, GNB, RF, XGB, and NN). The hyper-parameter optimization

Table 5. Used hyper-parameters values in cross-validated Grid search. Names between parentheses are parameter names in the ML package.

Classifier	Hyper-parameter	Range/ Values
1) LSVM	Regularization (C)	0.1, 1, 5, 10
	Loss Function (loss)	L1, L2
	Penalization strategy (penalty)	squared_hinge, hinge
2) LR	Penalization strategy (penalty)	L1, L2 elastic
	Regularization (C)	0.1, 1, 5, 10
	solver algorithm (solver)	newton-cg, lbfgs, liblinear, sag, saga
3) PassiveAgressive	Regularization (C)	0.1, 1, 5, 10
	N idle iteration before stop (n_iter_no_change)	1, 5, 10
4) Nonlinear-SVM	Regularization (C)	0.1, 1, 5, 10
	kernel used (kernel)	rbf, poly, sigmoid
	polynomial kernel degree (degree)	2-6
	Kernel coefficient (gamma)	scale, auto
	Independent term in kernel function (coef0)	0.0, 0.01, 0.1, 1, 5, 10, 50, 100
5) GNB	default parameters	priors=None, var_smoothing=1e-09
6) RF	number of features to consider when looking for the best split (max_features)	auto, sqrt, log2
	number of trees in the forest (n_estimators)	50, 100, 200, 500, 1000
	function to measure the quality of a split (criterion)	gini, entropy
	bootstrap samples when building trees (bootstrap)	True, False
	min # of samples required to split an internal node (min_samples)	1, 2, 5, 10
7) XGB	Which booster to use (booster)	gbtree, gblinear, dart
	Learning rate (learning_rate)	0.001, 0.01, 0.1, 0.3, 0.5, 1
	Min loss reduction required to make a further partition on a leaf node (gamma)	0, 0.1, 0.5, 1, 1.5, 2, 5, 20, 50, 100
	Min sum of instance weight needed in a child (min_child_weight)	0.1, 0.5, 1, 5, 10
	subsample ratio of columns when constructing each tree (colsample_bytree)	0.6, 0.8, 1.0
	L2 regularization term on weights (lambda)	0, 0.001, 0.5, 1, 10
	L1 regularization term on weights (alpha)	0, 0.001, 0.5, 1, 10
8) NN	hidden layer sizes (hidden_layer_sizes)	(150,100,50,), (100,50,25,), (100,)
	Activation function (activation)	tanh, relu, logistic
	solver used for weight optimization (solver)	lbfgs, sgd, adam
	L2 regularization penalty (alpha)	0.0001, 0.001, 0.01, 0.05, 0.1, 0.5
	initial learning rate (learning_rate)	constant, adaptive
	Exponential decay rate for estimates of first moment vector in adam (beta_1)	0, 0.001, 0.01, 0.1, 0.3, 0.5, 0.9
	Exponential decay rate for estimates of second moment vector in adam (beta_2)	0, 0.001, 0.01, 0.1, 0.3, 0.5, 0.9

step is carried out for each combination of [feature-RFECV kernel-classifier], using grid search over the list of hyper-parameters on Table 5, with 5-fold cross-validation, with the help of GridSearchCV scikit learn toolkit. The aim of this search to identify the best RFE-CV kernel in terms of accuracy, to be used for the final classification/-validation stage. Based on the results of those 64 sets of combinations, we identify which setting best suits our data, then we investigate it with more validations, changing the splits and varying the number of folds.

Table 6 and Table 7 show the full details of this round of experiments, for both feature representations: summary statistics F and correlations $\hat{F}$ respectively. We notice in Table 7 that using correlations features, the non-linear kernel fails fast to provide representative features, in comparison to the linear SVM kernel, while we don not see this obvious degradation in the F representation. Both LR1 and LR2 kernels almost failed to provide representative features in terms of accuracy results (accuracy 60%), while RF kernel provide us with moderate results (mostly above 70%), LSVM was the one we are searching for, achieving accuracies up to 99% with $\hat{F}$ features. More importantly, we highlight that using our novel feature representation $\hat{F}$, we were able to achieve this boost in classification results ($\tilde{6}$%). To show which types of features were more representative, we show the histogram of occurrence of each type of summary statistics appearing in selected features from F with LSVM RFE-CV using in Fig. 9. The figure illustrates the efficacy of adding *SK* feature

Table 6. 5-fold Accuracy Results ± standard deviations for each recursive feature elimination (RFE) kernel, and each machine learning (ML) classifier, for the first feature representation (summary statistics) F.

ML Classifier	L1 LR-RFE	L2 LR-RFE	L-SVM RFE	Rf RFE
L-SVM	0.873 ± 0.042	0.873 ± 0.042	0.932 ± 0.034	0.551 ± 0.058
Pagg	0.871 ± 0.014	0.871 ± 0.014	0.903 ± 0.043	0.572 ± 0.048
LR	0.870 ± 0.036	0.870 ± 0.036	0.910 ± 0.051	0.581 ± 0.056
XGB	0.861 ± 0.029	0.861 ± 0.029	0.904 ± 0.063	0.630 ± 0.08
GNB	0.695 ± 0.055	0.695 ± 0.055	0.664 ± 0.084	0.592 ± 0.043
SVC	0.880 ± 0.013	0.880 ± 0.013	0.926 ± 0.026	0.591 ± 0.026
RF	0.672 ± 0.037	0.672 ± 0.037	0.703 ± 0.021	0.612 ± 0.065
NN	0.885 ± 0.014	0.885 ± 0.014	0.915 ± 0.032	0.611 ± 0.067

Table 7. 5-fold Accuracy Results ± standard deviations for each recursive feature elimination (RFE) kernel, and each machine learning (ML) classifier, for the second feature representation (correlations) $\hat{F}$.

ML Classifier	L1 LR-RFE	L2 LR-RFE	L-SVM RFE	Rf RFE
L-SVM	0.613 ± 0.071	0.598 ± 0.039	0.999 ± 0.002	0.736 ± 0.083
Pagg	0.615 ± 0.095	0.555 ± 0.073	0.990 ± 0.02	0.709 ± 0.02
LR	0.617 ± 0.074	0.602 ± 0.037	0.995 ± 0.01	0.749 ± 0.063
XGB	0.623 ± 0.071	0.617 ± 0.029	0.985 ± 0.02	0.738 ± 0.03
GNB	0.603 ± 0.055	0.590 ± 0.037	0.723 ± 0.037	0.723 ± 0.049
SVC	0.633 ± 0.059	0.607 ± 0.042	0.999 ± 0.003	0.746 ± 0.036
RF	0.600 ± 0.062	0.606 ± 0.038	0.648 ± 0.017	0.685 ± 0.044
NN	0.639 ± 0.087	0.610 ± 0.035	0.999 ± 0.002	0.773 ± 0.044

which appeared as important as the common FA metric, and points out the choice of skewness as a relevant summary statistic.

Following these results, we will only use LSVM RFE-CV kernel, with $\hat{F}$ representation (correlations) for further investigations, as it shows better performance. We will fix the hyper-parameters of the eight classifiers to the ones we previously found on the first set of experiments (Table 8), and randomly re-split different settings of k-fold cross-validation, with k = [2, 4, 5, 10], to test whether the achieved performance highly dependent on the split and/or the subjects of the previous experiment, and see the effect of changing the proportion of train/test on the results.

Table 9 show the final diagnostic accuracies of our proposed framework, using our novel feature representation with the help of RFE-CV with LSVM kernel, and Table 10 show the area under the curve for each of the classifiers across different k-folds. Without a new optimization, using the same settings, and on new sets of random splits, our innovative algorithm was still able to provide up to 99% accuracy, which clearly manifests the strength of the presented algorithm.

Table 8. Best chosen hyper-parameters (of the best kernel: LSVM) found to optimize performance on the set of tested classifiers

Classifier	Hyper-parameters
L-SVM	{'penalty': 'l2', 'loss': 'hinge', 'C': 1}
Pagg	{'n_iter_no_change': 5, 'C': 0.1}
LR	{'solver': 'newton-cg', 'penalty': 'none', 'C': 0.1}
XGB	{'reg_lambda': 0.001, 'reg_alpha': 0, 'min_child_weight': 10, 'learning_rate': 1, 'gamma': 0.1, 'colsample_bytree': 0.6, 'booster': 'gblinear'}
GNB	defaults
SVC	{'kernel': 'poly', 'gamma': 'scale', 'degree': 3, 'coef0': 5, 'C': 0.1}
RF	{'n_estimators': 50, 'min_samples_split': 2, 'min_samples_leaf': 0.1, 'max_features': 'sqrt', 'criterion': 'entropy', 'bootstrap': False}
NN	{'solver': 'adam', 'learning_rate': 'adaptive', 'hidden_layer_sizes': (100,), 'beta_2': 0.5, 'beta_1': 0.5, 'alpha': 0.0001, 'activation': 'logistic'}

Table 9. Mean Accuracy $\pm$ standard deviation across the k- folds, with k = 2, 4, 5, 10.

	k=2	k=4	k=5	k=10
LSVM	0.92 ± 0.018	0.991 ± 0.015	0.999 ± 0.002	0.999 ± 0.002
pagg	0.893 ± 0.018	0.951 ± 0.037	0.96 ± 0.026	0.982 ± 0.03
LR	0.902 ± 0.0	0.964 ± 0.018	0.978 ± 0.02	0.991 ± 0.018
XGB	0.556 ± 0.011	0.604 ± 0.021	0.591 ± 0.041	0.609 ± 0.119
GNB	0.644 ± 0.025	0.618 ± 0.079	0.613 ± 0.08	0.684 ± 0.133
RBF-SVM	0.511 ± 0.038	0.529 ± 0.021	0.573 ± 0.022	0.582 ± 0.076
RF	0.609 ± 0.02	0.591 ± 0.04	0.591 ± 0.05	0.596 ± 0.054
NN	0.871 ± 0.004	0.969 ± 0.019	0.973 ± 0.026	0.964 ± 0.034

Table 10. Calculated Area Under the Curve for each classifier across the k-folds, with k = 2, 4, 5, 10.

	k=2	k=4	k=5	k=10
LSVM	0.919	0.991	0.999	0.999
pagg	0.891	0.948	0.959	0.982
LR	0.9	0.962	0.977	0.991
XGB	0.543	0.593	0.583	0.606
GNB	0.644	0.618	0.608	0.683
RBF-SVM	0.509	0.529	0.565	0.575
RF	0.571	0.549	0.548	0.552
NN	0.873	0.969	0.975	0.963
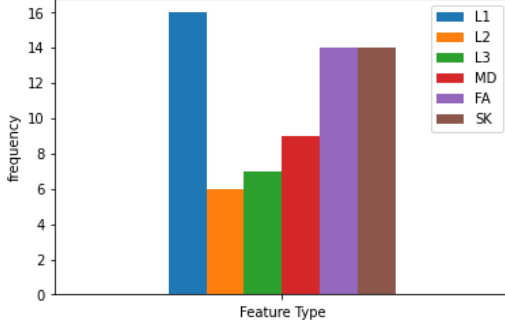
(a) Feature type occurrences histogram
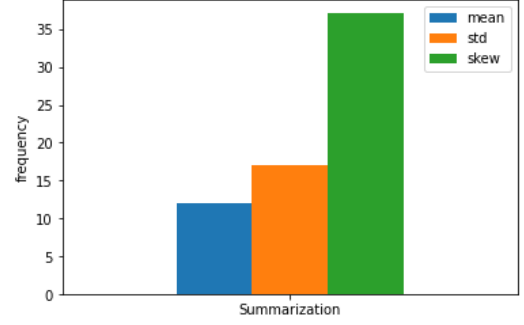
(b) Summary Statistics occurrences histogram

Figure 9. Histogram of types of selected summary statistics features.

Table 11. Top 12 WM brain area pairs which feature correlations where highly ranked through RFE-CV selection. L or R at the end for Left or Right hemispheres respectively.

Retrolenticular Part Of Internal Capsule L	&	Fornix Cres/ Stria Terminalis
Anterior Limb Of Internal Capsule L	&	Uncinate Fasciculus R
Body Of Corpus Callosum	&	Tapetum L
Corticospinal Tract R	&	Posterior Corona Radiata R
Posterior Limb Of Internal Capsule R	&	Retrolenticular Part Of Internal Capsule R
External Capsule R	&	Tapetum L
Middle Cerebellar Peduncle	&	Inferior Cerebellar Peduncle R
Anterior Limb Of Internal Capsule R	&	Tapetum R
Middle Cerebellar Peduncle	&	Cingulum Cingulate Gyrus L
Anterior Limb Of Internal Capsule R	&	Fornix Cres /StriaTerminalis R
Inferior Cerebellar Peduncle R	&	Retrolenticular Part Of Internal Capsule R
Cingulum Hippocampus L	&	Superior Fronto-occipital Fasciculus R

Fig. 10 illustrate the importance of top selected features by our RFE-CV LSVM kernel. The bars in blue on the left indicate high negative correlation importance with our positive class (autism), while the ones in dark orange on the right indicate a positive importance coefficient. The longer the bars, the higher the coefficient indicating more importance for features of this brain-area pair. Table 11 list the name of the top twelve feature pairs as ranked by our selection algorithm for easier identification. We can see that most of those brain areas already appear in literature as correlating with ASD phenotype. We already see some areas appear more than once in the top 12 pairs, we will discuss the importance of the highlighted brain areas in the following section, discussion.
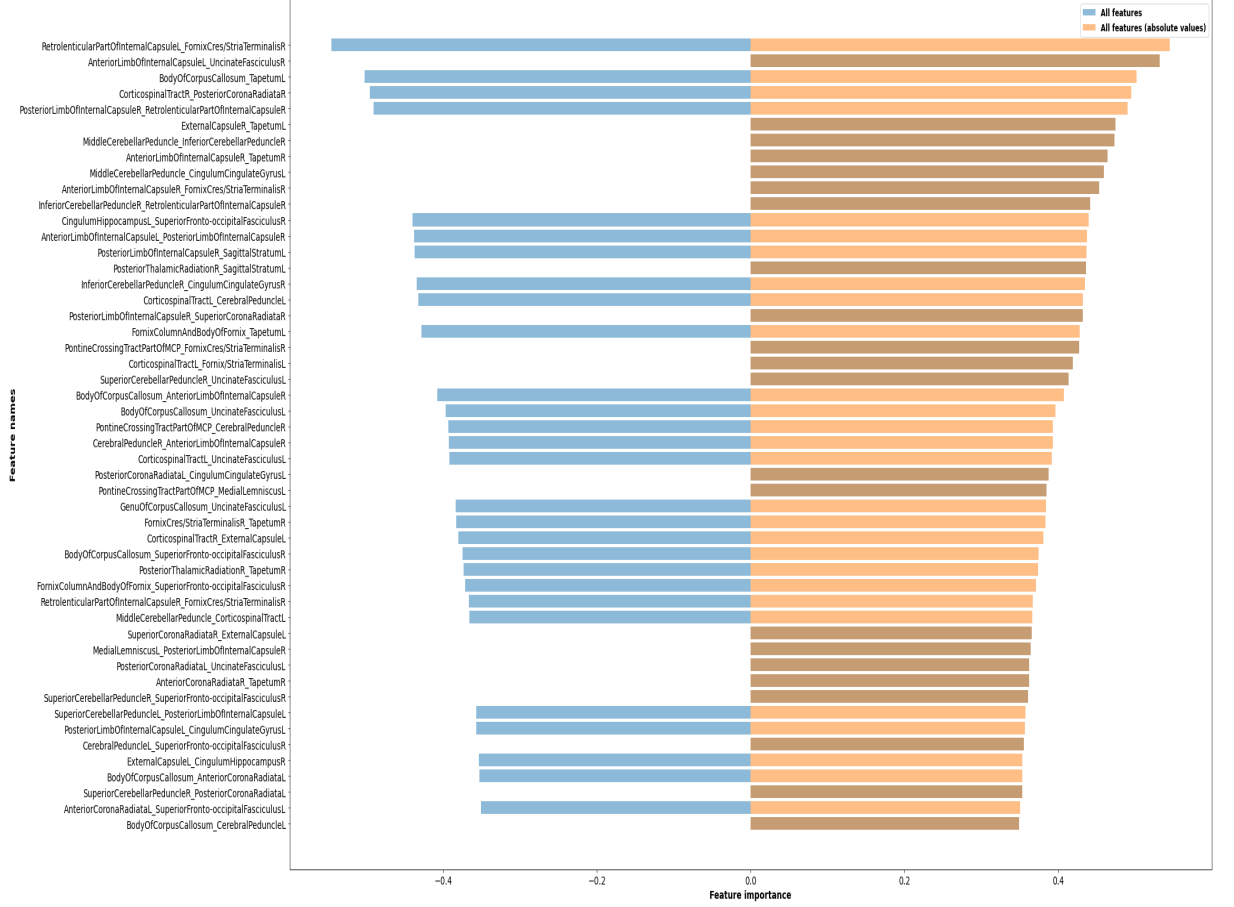
Figure 10. Sorted coefficient of importance for top 50 selected features of area-pairs correlations.

4   Chapter Discussion

The proposed technique adopted in this study introduced a novel feature representation applied on a large number of subjects, obtained from a publicly available dataset. We performed extensive experimentation to validate the results introduces in this chapter, as well as pave the path for developing new frameworks that may benefit from our novel algorithm. In addition to the achieved promising results, in terms of high cross-validated balanced accuracy, we introduced the notion of interaction between brain areas' micro-connectivity and its viability of reaching a better classification of autism. More importantly, we identified the brain-area pairs that mostly contributed to reaching the final decision.

We highlight that those identified brain areas in Table 11 align with the corpus of findings from previous literature studying autism impairments. The uncinate fasciculus (uc) is a fiber pathway through the external capsule (ec), which links the ventral frontal cortex, in particular Brodmann areas 11 and 47, with the temporal pole, and differences in it was revealed in [177, 188]. On the other hand, the middle cerebellar peduncle (mcp) carries signals from the cerebral cortex and subcortical

regions, via the pontine nuclei, into the cerebellar cortex. The internal capsule (ic) microstructure was found to undergo an atypical developmental trajectory in autistic patients, manifested as increased connectivity from childhood to adulthood [62]. All parts cited in this study of the ic are involved in autism [62–64, 189, 190], and DTI changes have been correlated with autistic behaviors including inattention, self-injury, repetitive behaviors, and social deficits. In general, all white matter tracts identified here (Table 11, Fig. 10) connect cortical (sensory motor cortex, frontal/occipital lobes, cingulate) and subcortical regions (thalamus, hippocampus, cerebellum), thereby contributing to deficits (inattention, self-injury, repetitive behaviors, motor, social, memory, emotional regulation, and sensory impairments) found in autistic individuals [62–64]. Shukla et. al [190] identified reduced FA and increased RD in ic and corpus callosum (cc) in children with autism. They also spotted increased MD in the anterior and posterior limbs of ic. Significant differences in the AD of the stria terminalis (st) were reported by Yamagata et. al. [191] between ASD and TD individuals. Reduced FA and increased RD of st were also reported in [188], and higher AD of st in TD children was noted in [64]. Differences in middle, inferior, and superior cerebellar peduncle [190, 192–194], and corpus callosum [64, 190, 192, 195] were also reported on those previous studies.

The tapetum WM is part of the splenuim fibers around cc, providing connectivity between the temporal lobe, and was found to play a role in different mental disorders [196]. Reduced FA, increased RD, and decreased AD of the tapetum in ASD. Abnormalities in the corticospinal tract, corona radiata, external capsule, cingulum cingulate cyrus, cingulum hippocampus, and superior fronto-occipital fasciculus were noted in previous studies [46, 52, 60, 63, 70, 167, 188, 189, 194, 197, 198]. We stress that our findings are for brain regions' interactions with others, following the idea of disrupted connectivity introduced by Vasa et al, and work normally done in functional MRI experiments. In [56], Vasa et al. reviewed some of the current structural and functional connectivity ASD data to examine the "disrupted connectivity" theory. They identified and highlighted many confounding factors in the literature that could have affected this conclusion.

Algorithm 2 Diffusion Tensor Autism Diagnosis Algorithm

1: ∀ **subject's data files: (NII+bval+bvec)** :
2:     1. Check for errors, check bval and bvec files.
3:     2. run pre-processing modules:
4:         i) Run skull stripping using brain extraction tool (BET).
5:         ii) Run FSL's eddy current correction tool.
6:         iii) Register the DTI IIT Human Brain Atlas to each subject space using DTI-TK tool, save transformations.
7:         iv) Recheck for any generated errors or deformations.
8:     3. Feature Calculations:
9:         i) Use FSL to calculate DTI Tensor, scale units, calculate RDs, AD, FA, MD, Tskew volumes.
10:         ii) Apply resulted transformation on the JHU atlas labels to generate masks.
11:         iv) Use registered masks to extract each feature for each WM region
12:         v) Calculate summary statistics (μ, σ, Sk) for each area for each feature (λ_1,λ_2,λ_3,FA,MD, Tskew), rank feature values across the different 48 brain areas, get a concatenated feature vector (3*6). Create a feature matrix F to be used as a first variant of the input data matrix X.
13:         vi) Calculate correlations between feature vectors of each two areas. To create a feature matrix F_2.
14:         vii) From F_2: remove redundant correlations (L and diagonal) and concatenate U to create $\hat{F}$ to be used as a second variant of the input data matrix X.
15: 4. RFECV Feature Selection: for each feature representation, and for each RFE-CV kernel:
16:     i) Split input data X, labels y into k folds. Each time use one fold as X_{test}, y_{test}, rest as X_{train}, y_{train}.
17:     ii) Train the classifier using each X_{train}, y_{train}.
18:     iii) Get the balanced accuracy score of the trained classifier using X_{test}, y_{test}.
19:     iv) Calculate the cross validated score and sort features based on importance.
20:     v) Remove the least important features from X matrices, and repeat the steps from i) to v) until only one feature exist.
21:     vi) Determine the n features that provided the best cross validated score along with its hyper-parameters to be used for each of the kernel.
22: 5. Classification:
23:     ∀ classifier, for each configuration of hyper-parameters:
24:     i) Split reduced X_{select}, with n selected features, into k folds, along with y.
25:     ii) Calculate the cross validated score for each hyper-parameter's configuration.
26:     iii) Determine best hyper-parameters configuration in terms of score, for each classifier.
27:     iii) Find best classifier/parameters, along with its used n features.

CHAPTER V

THE ROLE OF RS-FMRI IN AUTISM DIAGNOSIS: A COMPREHENSIVE FRAMEWORK

Recent advancements in neuroimaging and machine learning suggest a rapid and objective alternative, using brain imaging. On top of the used imaging modalities, fMRI is considered the most promising technology. A detailed study of the implementation of feature engineering tools to find discriminant insights from functional brain imaging, using both a conventional feature representation and a novel dynamic connectivity representation, and the use of a machine learning framework to assist in the accurate classification of autistic individuals is presented in this chapter. Based on a large publicly available dataset, this extensive research highlights different decisions along the pipeline and their impact on diagnostic accuracy. It also identifies potentially impacted brain regions that contribute to an autism diagnosis. A large publicly available dataset of 884 subjects from the Autism Brain Imaging Data Exchange I (ABIDE-I) initiative was used to validate our proposed framework, achieving a global balanced accuracy of 98% with 5-fold cross-validation, and proving the potential of the proposed feature representation. As a result of this comprehensive study, we achieve state-of-the-art accuracy, confirming the benefits of feature representation and feature engineering in extracting useful information, as well as the potential benefits of utilizing neuroimaging in the diagnosis of autism.

1   Background

In this chapter, we utilize fMRI to provide an understanding of assessing autism. There are two major types of experiments used to analyze the fMRI modality in order to study functional activation anomalies in the brain (i) resting state fMRI (rs-fMRI) and (ii) task-based fMRI [199]. In task-based functional MRI, the subject performs a particular task, such as: (1) figures [109], (2) facial expressions [94], (3) rewards [200], or (4) other specific tasks, then the brain activity is analyzed. In resting fMRI, brain activity, in terms of blood-oxygen-level-dependent (BOLD) signal is captured while the subject is at rest. Since connectivity patterns reveal the resting state, they have proven to be beneficial in diagnosing mental disorders, such as Alzheimer's disease [201] and schizophrenia [202]. As an example, a high degree of accuracy was achieved in diagnosing schizophrenia using the approaches described in [202]. There is evidence that the functional connectivity between major networks as well as the functional connectivity within individual networks is altered in ASD, as demonstrated by numerous studies [81, 203]. Due to autism's heterogeneous nature, brain connectivity can vary widely among individuals with the disorder, making classification of the condition difficult. The design of less-sensitive functional

connectivity feature that is less affected by age, sex, and designs of the resting-state scan, and studying its correlation with autism is a hot research area [204], emerging into two popular brain connectivity representations: the conventional, more popular, static functional connectivity (FC), and the newer dynamic functional connectivity (dFC) representations. Those functional connectivity metrics are believed to capture different internal states of the brain while in rest [205]. The static FC is a matrix obtained by calculating the Pearson cross-correlation coefficient of the BOLD signals across pairs of pre-defined brain areas. Following statistical analysis and depending on whether one examines local or global networks, there is evidence of both under- and over-connectivity in autism in the majority of the literature [204]. As most of the literature implies temporally stationary functional networks in resting state, dynamic, or time-varying, changes to functional connectivity that occur during brain scanning are not sufficiently considered by static FC. Newer studies suggest periodically changing spatial patterns of functional networks. To capture those dynamic connectivity patterns, multiple computational strategies were used to find dFC that consider such temporal fluctuations of functional connectivity [206]. dFC analyses allow identifying not only common brain states but also transitions between them. The most commonly used approach for dFC computation is sliding window techniques [207], while other approaches include clustering methods, dynamic connectivity regression, time-frequency analysis, wavelet transforms [208], dynamic connectivity detection, and time series models [206,209]. As the characteristics of autism vary from individual to individual in terms of symptoms and severity, a more personalized approach to predicting and analyzing the behavior and functional capabilities of each autistic subject has become increasingly necessary. Consequently, we can create a treatment plan that is tailored specifically to the needs of each autistic individual.

This work uses both a static FC matrix, as well as a novel dFC approach to investigate the role of rs-fMRI in the diagnosis of autism in a large cohort of 884 subjects, testing different processing and machine learning pipelines. The main limitation of the previous works is that each only gives a limited perspective on the bolts of an efficient CAD system. This work presents a unified framework that addresses the following:

- The impact of using different atlases, including the automated anatomical labeling (AAL) and Talairach and Tournoux (TT) atlases.

- The effect using different preprocessing strategies

- The effectiveness of using our novel dFC, in comparison to using conventional static FC.

- The dimensionality reduction problem using two-stage feature selection, with four types of kernels.

- The role of the classification strategy, investigating six different classifiers.

- The ability to highlight the importance of each of the previous choices on the overall performance.

Table 12. Demographics Summary Table of the 884 subjects used in this chapter, showing sex counts (M: male, F: female), age at scan in years, and full-scale IQ (FIQ).

	ASD Group (n=408) M = 358, F=50		TD Group (n=476) M = 388, F = 88	
	AGE	**FIQ**	**AGE**	**FIQ**
count	408	379	476	442
mean	17.69	106.19	16.79	111.28
std	8.93	17.01	7.35	12.48
min	7	41	6.47	73
max	64	148	56.2	146

The remainder of this chapter is organized as follows: section 2 describes the entire methodology of feature representation, pre-processing, and diagnostic classification. We present the various results on the ABIDE-I rs-fMRI in section 3. Finally, the discussion and conclusion are presented in section 4.

2 Materials and Methods

In this work, the Autism Brain Imaging Data Exchange I (ABIDE I) dataset is used [210], which is a publicly available repository collected from 17 different sites, with rs-fMRI, sMRI imaging modalities (`http://fcon_1000.projects.nitrc.org/indi/abide/abide_I.html`). Table 12 provides the summary of the 884 subjects' demographics: age in years, label, Full-scale IQ, and gender. The full demographics as well as the scanning parameters of the functional MRI are available on the dataset website. The parameters include the type of scanner, the scanning protocol, repetition time (TR), echo time (TE), flipping angle, and experiment duration for resting state fMRI.

Preprocessing

Functional MRI data were preprocessed according to the standard configurable pipeline for the analysis of connectomes (C-PAC) [211]. Preprocessing pipeline includes performing slice timing correction, motion realignment, skull stripping, and intensity normalization in this order. 24 motion parameters are used as regressors to overcome the subject's motion-related confounding variables. Additionally, five more from white matter and CSF mean levels are regressed to eliminate their effects. Then, one of four different preprocessing strategies is applied for filtration and signal correction. The main difference between those strategies is whether global signal correction (inclusion of global mean signal in nuisance regression) was made and whether filtration (band-pass filtering after global signal correction) was performed. Those four strategies are denoted as: *filt_global*, *filt_noglobal*, *nofilt_global*, and *filt_noglobal*. Lastly, structural MRI data, after skull stripping, segmentation, normalization, and registration to the standard MNI-152 space, is used for registration of the corresponding fMRI volumes
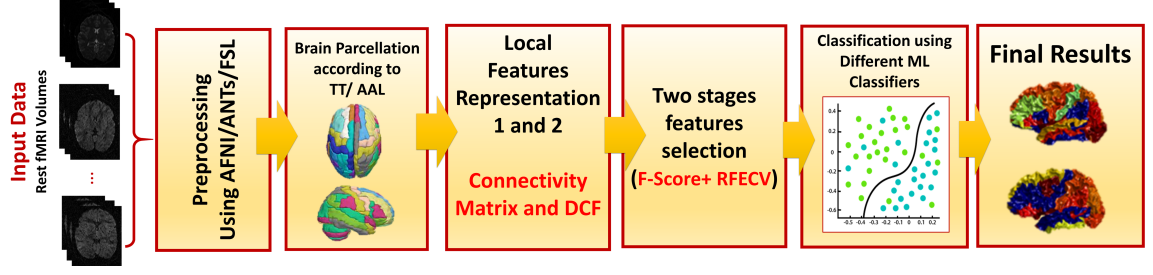
Figure 11. Illustration of the full steps of the adopted framework

to the same space after those preprocessing steps. For each of the four strategies, we will have different outputs.

Different brain regions are identified on the registered data using a standard atlas parcellation. Two atlases were used and investigated in this work: AAL atlas, defining 116 brain regions, and TT atlas, defining 97 different regions using Brodmann areas labeling.

After preprocessing, each subject is now represented by an average BOLD signal (time series, length varying by site based on total scanning time) for each brain region, and we have *eight* datasets, one for each (strategy/ atlas). The next step is to convert it to a more meaningful representation that captures functional connectivity and is less dependent on the subject's differences. Figure 11 illustrates the end-to-end pipeline of our proposed classification algorithm.

Feature Representation

For the purpose of studying the coherence between different areas of the brain, two different feature representations were used to examine functional connectivity. First, the most famous and commonly used static FC matrix, where the correlation between the full duration of the activation courses is used as a measure of functional connectivity. The reason behind this selection is that it captures the intrinsic functional network of the brain.

The static functional connectivity matrix FC is constructed as the Pearson correlation coefficient (ρ) between each pair of the $(A = 116 \,|\, 97\,)$ areas in the atlas. The effective output feature size is $(A \times (A - 1) \div 2)$, because of symmetry, resulting in a total of 884×6670 for AAL, or 884×4656 for TT, feature matrices. Figure 12 illustrates the pipeline of this adopted feature representation.

The second feature representation introduced in this work is an enhanced version of dynamic functional connectivity, dFC, where temporal dynamics are considered in correlation calculation. The calculation starts with multiplying a shorter Gaussian sliding window with width w with each time signal, to calculate pair correlation, with an overlapping step size s. Following the literature, [209], a Gaussian window of size $w = 21TR$, $\sigma = 3TR$ and a step size of $s = 1$ were used, where TR is the fMRI repetition time, typically 1500 - 2000 ms depending on the scanning site. Hence, for each pair of brain regions of length L, an M correlations are calculated, where $M = ||(L - w)/s||$. Following hypotheses of under-connectivity and
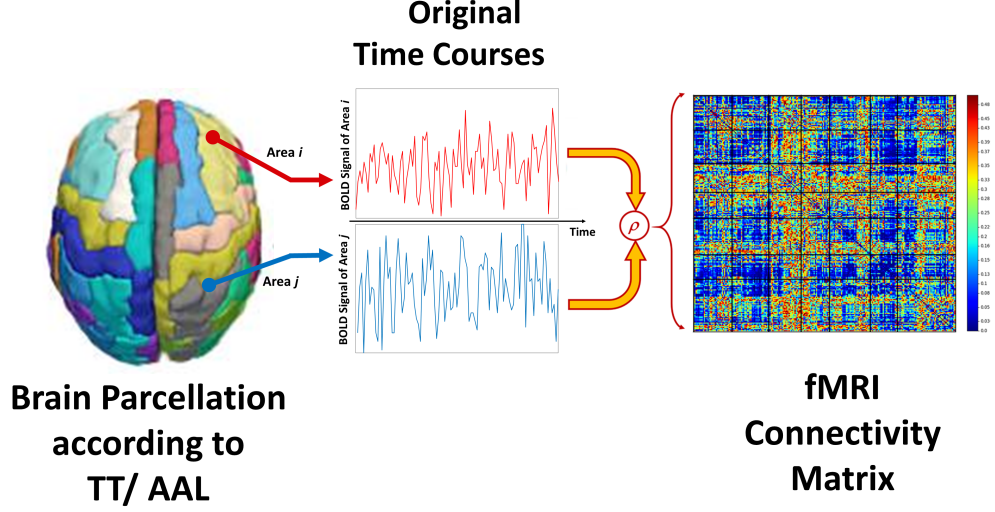
Figure 12. Visual diagram of the calculations of the static functional connectivity FC representation

over-connectivity differences between functional activation of autistic and typically developed brain, a quantification using both the percentage of strong correlations n_{st} and the percentage of weak/no correlation n_{wk} are used to represent over- and under-connectivity between each brain areas, where $n_{st} = \frac{1}{M} \sum_M \mathbb{1} \quad : if \quad \rho_{ij} \geq 0.8$, and $n_{wk} = \frac{1}{M} \sum_M \mathbb{1} \quad : if \quad \rho_{ij} \leq 0.25$. This creates two metrics for each pair of regions identifying the existence of under- and over-connectivities, yielding a double size dFC feature matrices in comparison to the FC. representation. Figure 13 illustrates the pipeline of the second proposed feature representation in this chapter. At this step, we have 16 different inputs, one for each (strategy/ atlas/ feature representation) combination.

Feature Selection

Since the feature space, for both representations, is large, there is an urge for the employment of a feature reduction technique to address the curse of dimensionality problem. Since the employed feature reduction shall preserve the semantics of original features, many famous techniques such as principal component analysis (PCA), factor analysis (FA), or linear discriminant analysis (LDA) may not be suitable, as it creates a newly transformed feature space that makes it hard to extrapolate the meaning of any following clinical classification, or underlying functional abnormalities of autistic individuals. Two cascaded feature selection stages are used: a simple univariate selector followed by a more sophisticated recursive feature elimination (RFE) with cross-validation (RFE-CV), to select the best subset of features.

The univariate selector is a fast way that aims to initially reduce the feature space to make the second stage computationally efficient. It computes the ANOVA F-value score for each feature to select the top proportion accordingly, using GenericUnivariateSelect from Sklearn. Following it, a recursive feature elimination eliminates weak
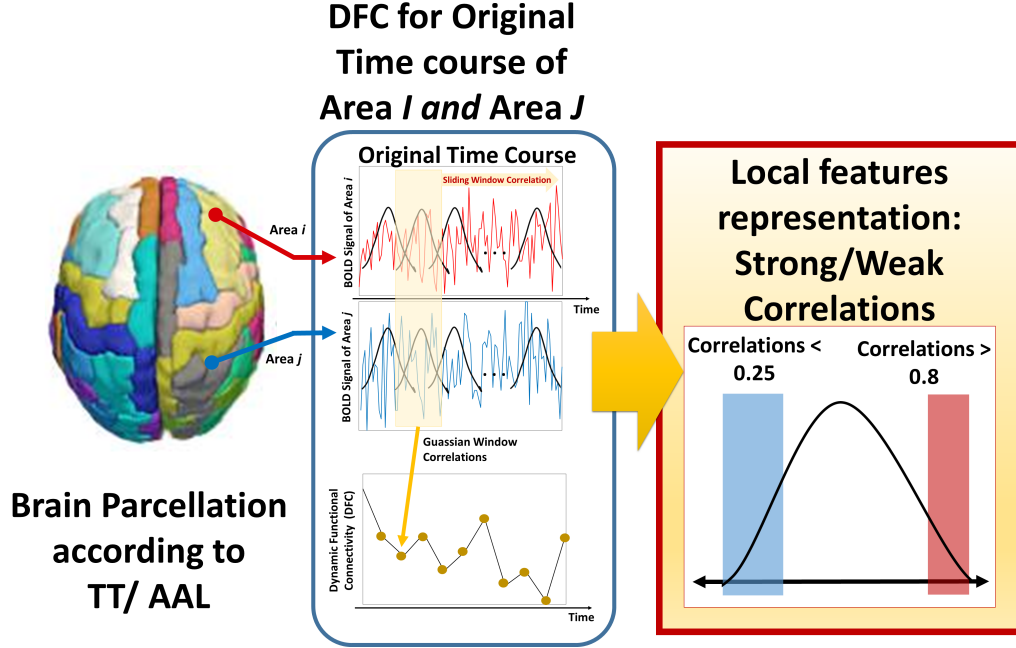
Figure 13. Visual diagram of the calculations of the dynamic functional connectivity *dFC* representation

features until a specified number of features is reached by fitting a kernel classifier and removing the weakest features. By eliminating dependencies and collinearities, RFE attempts to achieve a better understanding of the model. Cross-validation aims to score the strength of features on the test subset, other than the training folds data used in training the kernel, to mitigate over-fitting. The step of the eliminated features, scoring metric, kernel type, and the number of folds are all parameters of choice. Here, a step size of 2 features (for faster elimination, yet small enough for a good performance), k=5 folds (common 5-fold cross-validation), and balanced accuracy was chosen. Four different classifiers were tested as FS kernel, namely linear support vector machine (lsvm), logistic regression (lr), random forest (rf), and light gradient boost machine (lgbm) [185,186], to investigate different feature-relationships. The two-stage feature selection is applied to each dataset/feature representation to find the best *n* features that provided the best cross-validated score. Next, the performance of the sixteen models was evaluated on a set of machine learning classifiers to select which model to use for further processing. The code for the whole previous steps, starting from data download, processing, and feature calculations, is publicly available on [212].

Machine Learning

In order to learn how to classify autistic brains, we set up a system of different machine learning classifiers from the set of *n* features selected for each of 16 data representations. We evaluated six different classifier types and optimized their hyperparameters in order to establish the most accurate parameter classifier model. Those classifiers,

including linear and non-linear ones, are: i) lsvm; ii) lr; iii) rf; iv) lgbm; v) neural networks (nn); and vi) radial-basis function SVM (svm). The different types would test different relations between the two feature classes, with the first two being linear estimators. The cross-validated random search was used for hyper-parameter optimization for each of the six classifiers, with k=5 folds, optimizing for a balanced accuracy score on each test fold to get the best parameters on the hyper-search space. Accordingly, these steps were followed for each classifier, for each dataset using only the selected features: Split data into k-folds, train four and test one each round, and record the performance of the classifier for each round on the test subset for each parameter configuration. The classifier with the best performance is selected, together with hyperparameters as well as its maximum average cross-validated score, as well as the standard deviation over folds.

3   Results

Running the explained experimental pipeline on a cluster of 16 high-performance computers, we were able to collect detailed results. In tables 18 to 33, 16 sub-tables of cross-validated test scores are shown, one table for each feature_representation/ atlas/ strategy, with mean ± standard deviation across folds for each best hyper-parameters for each feature selection kernel (column) and machine learning classifier (row). Here, we highlight what was the best choice for each stage, in addition to the power of this choice, and the best accuracy achieved accordingly.

Significance of data representation

In order to test the significance of the configuration of choice, we logged all model scores, for each of the five test fold, labeled for 1) feat: (two) FC or dFC, 2) atls: (two) TT or AAL, 3) preprocessing strategy: (four) filt_global, etc., 4) feature selection kernel of the RFE-CV: (four), and 5) machine learning classifier (six). Thus, the labeled table would contain up to 1920 results. Three-factor ANOVA with the calculation of the sum of squares (SS) for the factors, was used to test the effect of the major three factors pre-machine learning: feature representation, atlas, and preprocessing. Full interactions were tested (Table 13), before removing non-significant factors (Table 14), yet the sum of squares that each factor accounted for did not change due to the nature of Type III sum of squares. In the following part, the effect of each factor is discussed. It is important to note that all configurations (for feature selection, classifier, ...etc) were considered here, not only high-performing ones, which would be seen as having lower mean accuracy. For each factor, we aim here to study the effect of it comparatively not just quantify its performance, especially as the experiments are paired: less-performing configurations would appear in both groups.

Table 13. Multifactorial (3-way) ANOVA results. Feat denotes feature representation, Atls denotes the used atlas, and Strat is one of the four preprocessing strategies. sum_sq, df, F, PR are standard result names of sum of squares, degree of freedom, F_score, and p_value of this F_score, for each factor.

	sum_sq	df	F	PR(>F)
C(Feat, Sum)	0.941852	1.0	163.004715	7.364232e-36
C(Strat, Sum)	0.177957	3.0	10.266230	1.053597e-06
C(Atls, Sum)	0.149164	1.0	25.815521	4.129224e-07
C(Feat, Sum):C(Strat, Sum)	0.117433	3.0	6.774646	1.528091e-04
C(Feat, Sum):C(Atls, Sum)	0.013784	1.0	2.385576	1.226282e-01
C(Strat, Sum):C(Atls, Sum)	0.034962	3.0	2.016924	1.095533e-01
C(Feat, Sum):C(Strat, Sum):C(Atls, Sum)	0.084563	3.0	4.878417	2.210611e-03

Table 14. Multifactorial (3-way) ANOVA test results after removing insignificant interactions

	sum_sq	df	F	PR(>F)
C(Feat, Sum)	0.936316	1.0	160.682470	2.134089e-35
C(Filt, Sum)	0.179172	3.0	10.249322	1.078933e-06
C(Atls, Sum)	0.148105	1.0	25.416432	5.062110e-07
C(Feat, Sum):C(Filt, Sum)	0.117208	3.0	6.704737	1.686921e-04

Preprocessing pipeline:

The choice of the preprocessing strategy (whether to perform global signal correction, and whether to apply band-pass filtering) has a significant effect on the classification performance ($p \simeq 10^{-06}$). From Table 14, with $F = 10$, we can see that the effect of this factor, although significant, is less important than the other factors. While the difference between the overall mean accuracy for [filt_noglobal, nofilt_global, nofilt_noglobal] is less than 0.2%, the mean **filt_global** accuracy is higher 2.5%. See Table15 for the summarized results across strategy selection. Another important aspect when analyzing the full results listed in tables 18 to 33, is that although the max performance was NOT accompanied with **filt_global** strategy, the scores were slightly higher across other models of the strategy.

Atlas use:

In the second level of importance comes the used atlas in brain parcellation (TT or AAL), with $F = 25.5$. The choice of the atlas also has a significant effect on the classification performance ($p \simeq 4 \times 10^{-07}$) as we can see in from the ANOVA tables. The mean average performance is 2% higher in favor for the *AAL* atlas. This gives an important indication that the more granular the atlas is (116 areas in comparison to 97 areas), the more informative the features we have (the mean BOLD signal), which leads to better accuracy results. See Table 16 for the summarized results across atlas use.

Table 15. Average per- preprocessing strategy accuracy (per 480 results each cell)

Filt Strategy	Average Score
filt_global	0.774994
filt_noglobal	0.750322
nofilt_global	0.752618
nofilt_noglobal	0.755514

Table 16. Average per-Atlas accuracy (per 960 results in each cell)

Atls	Average Score
AAL	0.767138
TT	0.749713

Table 17. Average per-feature representation accuracy (per 960 results in each cell)

Feat	Average Score
FC	0.736319
dFC	0.78093

Dynamic connectivity:

As clearly seen in Table 13 and Table 14, the proposed new feature representation has the biggest effect on the target (accuracy score). This is demonstrated with a high f_value of $F \simeq 160$ and a highly significant probability of $p \simeq 2 \times 10^{-35}$. On average, the dynamic functional connectivity representation we proposed scored an accuracy 5% higher than the conventional functional connectivity (Table 17). The results represent a key finding of the body of the presented comprehensive experiments in this work.

Model results

The following 16 tables, show the 5-fold cross-validated accuracy results for each atlas/ feature representation combination. Tables 18, 19, 20, 21 shows the results of different strategies for *dFC* representation on AAL atlas, while Tables 22, 23, 24, 25 shows the results on TT atlas. Similarly, Tables 26, 27, 28, 29 shows the results of different strategies for the conventional *FC* representation on AAL atlas, while Tables 30, 31, 32, 33 shows the results TT atlas. Tables 34 and 35 give cross-sectional summaries across ML and FS used. We can see a trend in performance, with (dFC/ AAL) is the best performing in general, then (dFC/ TT), (FC/ AAL), and (FC/ TT) having the least scores.

In terms of average scores, as shown in the previous tables, **lsvm** kernel of the feature selection was the best performing, and *rf* was the worst. Both **lsvm** and **lr** classifiers performed the best on average, while rf and lgbm came at the end. The top balanced accuracy achieved was **98%** for lsvm feature selection, lsvm classifier, nofilt_global preprocessing, AAL atlas, and dFC feature representation. This model

Table 18. Average ± standard deviation across the 5 folds of each best model for each feature-selection (column) / classifier (row) pair, for filt_global settings, AAL atlas, and Dynamic connectivity (dFC).

	lgbm	rf	lr	lsvm
lr	0.82 ± 0.01	0.86 ± 0.02	0.90 ± 0.04	0.91 ± 0.02
lsvm	0.81 ± 0.02	0.84 ± 0.03	0.89 ± 0.03	0.91 ± 0.02
rf	0.77 ± 0.04	0.65 ± 0.02	0.65 ± 0.02	0.65 ± 0.02
svm	0.82 ± 0.01	0.84 ± 0.03	0.88 ± 0.03	0.91 ± 0.03
nn	0.82 ± 0.02	0.83 ± 0.04	0.86 ± 0.05	0.90 ± 0.02
lgbm	0.82 ± 0.02	0.67 ± 0.03	0.65 ± 0.03	0.66 ± 0.05

Table 19. Average ± standard deviation across the 5 folds of each best model for each feature-selection (column) / classifier (row) pair, for filt_noglobal strategy, AAL atlas, and Dynamic connectivity (dFC).

	lgbm	rf	lr	lsvm
lr	0.81 ± 0.04	0.77 ± 0.03	0.83 ± 0.02	0.84 ± 0.02
lsvm	0.80 ± 0.04	0.76 ± 0.03	0.83 ± 0.03	0.85 ± 0.02
rf	0.79 ± 0.04	0.77 ± 0.02	0.83 ± 0.02	0.85 ± 0.02
svm	0.81 ± 0.04	0.77 ± 0.02	0.82 ± 0.04	0.83 ± 0.03
nn	0.74 ± 0.05	0.68 ± 0.02	0.68 ± 0.04	0.68 ± 0.04
lgbm	*NA: Failed*	0.67 ± 0.03	0.68 ± 0.03	0.66 ± 0.05

Table 20. Average ± standard deviation across the 5 folds of each best model for each feature-selection (column) / classifier (row) pair, for nofilt_global strategy, AAL atlas, and Dynamic connectivity (dFC).

	lgbm	rf	lr	lsvm
lr	0.82 ± 0.02	0.80 ± 0.01	0.83 ± 0.02	0.98 ± 0.01
lsvm	0.82 ± 0.02	0.80 ± 0.02	0.82 ± 0.02	0.99 ± 0.01
nn	0.83 ± 0.03	0.79 ± 0.06	0.80 ± 0.04	0.96 ± 0.02
svm	0.81 ± 0.01	0.79 ± 0.01	0.82 ± 0.03	0.99 ± 0.01
lgbm	0.78 ± 0.03	0.65 ± 0.03	0.64 ± 0.05	0.70 ± 0.02
rf	*NA: Failed*	0.69 ± 0.04	0.67 ± 0.05	0.71 ± 0.02

Table 21. Average ± standard deviation across the 5 folds of each best model for each feature-selection (column) / classifier (row) pair, for nofilt_noglobal strategy, AAL atlas, and Dynamic connectivity (dFC).

	lgbm	rf	lr	**lsvm**
lsvm	0.78 ± 0.02	0.76 ± 0.04	0.87 ± 0.02	**0.95 ± 0.03**
lr	0.77 ± 0.01	0.75 ± 0.04	0.85 ± 0.04	**0.91 ± 0.03**
svm	0.80 ± 0.01	0.75 ± 0.03	0.87 ± 0.03	**0.94 ± 0.02**
nn	0.78 ± 0.02	0.76 ± 0.03	0.85 ± 0.02	**0.88 ± 0.02**
rf	0.71 ± 0.02	0.71 ± 0.06	0.67 ± 0.03	0.68 ± 0.04
lgbm	*0.75 ± 0.05*	0.74 ± 0.04	0.70 ± 0.05	0.71 ± 0.04

Table 22. Average ± standard deviation across the 5 folds of each best model for each feature-selection (column) / classifier (row) pair, for filt_global strategy, TT atlas, and Dynamic connectivity (dFC).

	lgbm	rf	lr	lsvm
lr	0.83 ± 0.04	0.80 ± 0.02	0.87 ± 0.01	0.86 ± 0.01
lsvm	0.83 ± 0.03	0.80 ± 0.02	0.88 ± 0.01	0.86 ± 0.00
rf	0.83 ± 0.02	0.80 ± 0.02	0.86 ± 0.01	0.86 ± 0.01
svm	0.83 ± 0.04	0.80 ± 0.03	0.86 ± 0.02	0.81 ± 0.08
nn	0.69 ± 0.02	0.66 ± 0.04	0.65 ± 0.05	0.67 ± 0.04
lgbm	0.68 ± 0.03	0.66 ± 0.03	0.64 ± 0.03	0.65 ± 0.03

Table 23. Average ± standard deviation across the 5 folds of each best model for each feature-selection (column) / classifier (row) pair, for filt_noglobal strategy, TT atlas, and Dynamic connectivity (dFC).

	lgbm	rf	lr	lsvm
lr	0.77 ± 0.03	0.75 ± 0.02	0.81 ± 0.03	0.89 ± 0.03
lsvm	0.77 ± 0.02	0.76 ± 0.01	0.79 ± 0.02	**0.91 ± 0.02**
svm	0.67 ± 0.02	0.67 ± 0.02	0.67 ± 0.02	0.68 ± 0.01
nn	0.68 ± 0.02	0.66 ± 0.03	0.64 ± 0.02	0.68 ± 0.02
lgbm	*NA: Failed*	0.77 ± 0.03	0.81 ± 0.02	**0.92 ± 0.02**
rf	*NA: Failed*	0.75 ± 0.02	0.79 ± 0.04	0.86 ± 0.06

Table 24. Average ± standard deviation across the 5 folds of each best model for each feature-selection (column) / classifier (row) pair, for nofilt_global strategy, TT atlas, and Dynamic connectivity (dFC).

	lgbm	rf	lr	lsvm
lr	0.80 ± 0.02	0.76 ± 0.02	0.82 ± 0.03	0.79 ± 0.04
lsvm	0.79 ± 0.02	0.76 ± 0.03	0.81 ± 0.04	0.78 ± 0.04
nn	0.79 ± 0.01	0.76 ± 0.02	0.81 ± 0.03	0.78 ± 0.03
svm	0.80 ± 0.03	0.72 ± 0.08	0.83 ± 0.04	0.80 ± 0.02
lgbm	0.72 ± 0.01	0.64 ± 0.03	0.68 ± 0.02	0.66 ± 0.03
rf	0.73 ± 0.04	0.63 ± 0.02	0.67 ± 0.02	0.64 ± 0.03

Table 25. Average ± standard deviation across the 5 folds of each best model for each feature-selection (column) / classifier (row) pair, for nofilt_noglobal strategy, TT atlas, and Dynamic connectivity (dFC).

	lgbm	rf	lr	lsvm
lsvm	0.78 ± 0.04	0.70 ± 0.02	0.89 ± 0.02	0.96 ± 0.01
lr	0.77 ± 0.04	0.71 ± 0.03	0.89 ± 0.01	0.92 ± 0.02
svm	0.77 ± 0.04	0.71 ± 0.04	0.88 ± 0.03	0.96 ± 0.01
nn	0.78 ± 0.05	0.68 ± 0.04	0.74 ± 0.03	0.73 ± 0.02
rf	0.74 ± 0.02	0.67 ± 0.03	0.71 ± 0.04	0.68 ± 0.02
lgbm	0.79 ± 0.05	0.70 ± 0.05	0.90 ± 0.02	0.92 ± 0.02

Table 26. Average ± standard deviation across the 5 folds of each best model for each feature-selection (column) / classifier (row) pair, for filt_global strategy, AAL atlas, and functional connectivity (FC).

	lgbm	rf	lr	lsvm
lr	0.74 ± 0.03	0.66 ± 0.04	0.77 ± 0.03	0.98 ± 0.01
lsvm	0.77 ± 0.03	0.70 ± 0.05	0.76 ± 0.02	0.93 ± 0.02
rf	0.77 ± 0.02	0.72 ± 0.03	0.78 ± 0.03	0.98 ± 0.01
svm	0.74 ± 0.01	0.68 ± 0.02	0.69 ± 0.01	0.71 ± 0.02
nn	0.74 ± 0.03	0.69 ± 0.04	0.77 ± 0.02	0.93 ± 0.02
lgbm	0.74 ± 0.03	0.68 ± 0.02	0.69 ± 0.02	0.75 ± 0.04

Table 27. Average ± standard deviation across the 5 folds of each best model for each feature-selection (column) / classifier (row) pair, for filt_noglobal strategy, AAL atlas, and functional connectivity (FC).

	lgbm	rf	lr	lsvm
lr	0.73 ± 0.04	0.70 ± 0.04	0.84 ± 0.04	0.73 ± 0.02
lsvm	0.74 ± 0.02	0.70 ± 0.04	0.83 ± 0.03	0.73 ± 0.02
svm	0.73 ± 0.02	0.70 ± 0.01	0.73 ± 0.02	0.69 ± 0.02
nn	0.74 ± 0.03	0.72 ± 0.04	0.83 ± 0.04	0.73 ± 0.03
lgbm	0.75 ± 0.02	0.71 ± 0.04	0.75 ± 0.04	0.68 ± 0.03
rf	0.73 ± 0.03	0.69 ± 0.03	0.84 ± 0.04	0.72 ± 0.03

Table 28. Average ± standard deviation across the 5 folds of each best model for each feature-selection (column) / classifier (row) pair, for nofilt_global strategy, AAL atlas, and functional connectivity (FC).

	lgbm	rf	lr	lsvm
lr	0.76 ± 0.04	0.72 ± 0.03	0.71 ± 0.04	0.82 ± 0.03
lsvm	0.76 ± 0.03	0.72 ± 0.04	0.72 ± 0.03	0.80 ± 0.02
nn	0.75 ± 0.03	0.73 ± 0.01	0.73 ± 0.03	0.82 ± 0.03
svm	0.72 ± 0.01	0.69 ± 0.03	0.69 ± 0.02	0.68 ± 0.03
lgbm	0.75 ± 0.03	0.73 ± 0.05	0.72 ± 0.05	0.78 ± 0.04
rf	0.73 ± 0.03	0.69 ± 0.02	0.69 ± 0.04	0.70 ± 0.03

Table 29. Average ± standard deviation across the 5 folds of each best model for each feature-selection (column) / classifier (row) pair, for nofilt_noglobal strategy, AAL atlas, and functional connectivity (FC).

	lgbm	rf	lr	lsvm
lsvm	0.70 ± 0.03	0.70 ± 0.03	0.83 ± 0.01	0.75 ± 0.04
lr	0.72 ± 0.03	0.70 ± 0.03	0.83 ± 0.01	0.75 ± 0.03
svm	0.72 ± 0.05	0.72 ± 0.03	0.81 ± 0.02	0.74 ± 0.04
nn	0.69 ± 0.02	0.68 ± 0.02	0.71 ± 0.03	0.67 ± 0.03
rf	0.72 ± 0.04	0.71 ± 0.06	0.82 ± 0.02	0.75 ± 0.04
lgbm	0.69 ± 0.04	0.69 ± 0.05	0.75 ± 0.04	0.72 ± 0.04

Table 30. Average ± standard deviation across the 5 folds of each best model for each feature-selection (column) / classifier (row) pair, for filt_global strategy, TT atlas, and functional connectivity (FC).

	lgbm	rf	lr	lsvm
lr	0.75 ± 0.03	0.71 ± 0.04	0.82 ± 0.01	0.81 ± 0.02
lsvm	0.74 ± 0.04	0.69 ± 0.02	0.81 ± 0.02	0.83 ± 0.02
rf	0.76 ± 0.03	0.71 ± 0.02	0.81 ± 0.02	0.84 ± 0.02
svm	0.73 ± 0.04	0.68 ± 0.04	0.72 ± 0.04	0.72 ± 0.03
nn	0.74 ± 0.03	0.70 ± 0.03	0.71 ± 0.02	0.71 ± 0.02
lgbm	0.75 ± 0.03	0.71 ± 0.03	0.81 ± 0.02	0.80 ± 0.04

Table 31. Average ± standard deviation across the 5 folds of each best model for each feature-selection (column) / classifier (row) pair, for filt_noglobal strategy, TT atlas, and functional connectivity (FC).

	lgbm	rf	lr	lsvm
lr	0.72 ± 0.02	0.71 ± 0.02	0.75 ± 0.02	0.84 ± 0.03
lsvm	0.70 ± 0.03	0.68 ± 0.03	0.75 ± 0.03	**0.89 ± 0.03**
svm	0.70 ± 0.02	0.68 ± 0.01	0.68 ± 0.03	0.67 ± 0.03
nn	0.73 ± 0.02	0.70 ± 0.03	0.76 ± 0.01	0.88 ± 0.04
lgbm	0.70 ± 0.04	0.68 ± 0.05	0.69 ± 0.03	0.70 ± 0.02
rf	0.74 ± 0.03	0.70 ± 0.03	0.76 ± 0.04	0.78 ± 0.03

Table 32. Average ± standard deviation across the 5 folds of each best model for each feature-selection (column) / classifier (row) pair, for nofilt_global strategy, TT atlas, and functional connectivity (FC).

	lgbm	rf	lr	lsvm
lr	0.71 ± 0.03	0.68 ± 0.02	0.75 ± 0.03	0.84 ± 0.03
lsvm	0.73 ± 0.03	0.69 ± 0.02	0.75 ± 0.03	0.79 ± 0.03
nn	0.73 ± 0.02	0.70 ± 0.01	0.77 ± 0.02	0.84 ± 0.03
svm	0.69 ± 0.04	0.67 ± 0.02	0.68 ± 0.01	0.68 ± 0.02
lgbm	0.72 ± 0.02	0.69 ± 0.03	0.70 ± 0.03	0.70 ± 0.02
rf	0.72 ± 0.03	0.69 ± 0.03	0.75 ± 0.02	0.79 ± 0.03

Table 33. Average ± standard deviation across the 5 folds of each best model for each feature-selection (column) / classifier (row) pair, for nofilt_noglobal strategy, TT atlas, and functional connectivity (FC).

	lgbm	rf	lr	lsvm
lsvm	0.71 ± 0.02	0.69 ± 0.03	0.77 ± 0.03	0.74 ± 0.02
lr	0.70 ± 0.02	0.67 ± 0.04	0.77 ± 0.02	0.76 ± 0.01
svm	0.71 ± 0.02	0.69 ± 0.03	0.76 ± 0.02	0.75 ± 0.02
nn	0.71 ± 0.02	0.68 ± 0.02	0.76 ± 0.03	0.70 ± 0.04
rf	0.68 ± 0.04	0.66 ± 0.04	0.68 ± 0.04	0.66 ± 0.03
lgbm	*NA: Failed*	0.67 ± 0.04	0.69 ± 0.04	0.67 ± 0.04

Table 34. Average of average accuracies over all runs, for each ML classifier.

ML	average
lsvm	0.79016
lr	0.7925
svm	0.7675
rf	0.71578
nn	0.75813
lgbm	0.72563

Table 35. Average of average accuracies over all runs, for each ML classifier.

FS	average
lgbm	0.752594
rf	0.716458
lr	0.770625
lsvm	0.794271

configuration (preprocessing, feature representation, atlas, feature selection, classifier, and found best parameters) is elected as the best classifier and is investigated more in the following subsections. The original dFC input was 13340 features, from which the lsvm-based feature selection elected 840 features, which are used in further processing. The best model was cloned, and 5-fold cross-validation using a new random split was made to ensure that the results were not specific to the previous k-fold run. Table 36 shows the resulted accuracy, sensitivity, specificity, and balanced accuracy ± standard deviations.

Table 36. Cross-validated test results of the best configuration-model

Metric	Accuracy	Sensitivity	Specificity	Balanced Accuracy
5-fold value	0.988 ± 0.004	0.987 ± 0.008	0.989 ± 0.007	0.988 ± 0.004

Table 37. Summary of first 10 selected features, as well as the top frequent brain regions in this selected list, from S4

index	First selected features	Top frequent region names	Frequency
1	Precentral_L__Rolandic_Oper_R_wk	Temporal_Sup_L	24
2	Precentral_L__Supp_Motor_Area_L_st	Postcentral_R	23
3	Precentral_L__Fusiform_L_wk	Frontal_Sup_Medial_R	22
4	Precentral_L__Parietal_Inf_L_wk	Precuneus_R	22
5	Precentral_L__SupraMarginal_R_st	SupraMarginal_R	21
6	Precentral_L__Precuneus_R_wk	Frontal_Sup_R	21
7	Precentral_L__Temporal_Sup_L_wk	Cingulum_Ant_R	21
8	Precentral_L__Temporal_Pole_Sup_R_wk	Supp_Motor_Area_L	21
9	Precentral_L__Cerebelum_Crus2_R_wk	Angular_R	21
10	Precentral_R__Frontal_Inf_Tri_L_wk	Hippocampus_R	21

Identified brain areas:

Appendix C provides the full list of the selected features that lead to the best model performance. An especially interesting finding is that identifying the weak/ under-connectivity between brain areas is far more important than the very strong correlations, with a percentage of wk features $= \mathbf{81.9\%}$, and strong correlations contributing only to the rest 18.1% of the selected features. We highlight the first 10 used features, as well as the top frequent brain regions in this selected list in Table 37, while the full list is available in Appendix C.

4 Chapter Discussion

We found a striking overlap between the top brain regions associated with ASD in this work with those identified in other fMRI studies. For example, in [213], left sup temporal (Temporal_Sup_L) were found regions of great contribution to ASD classification. Researchers in [214] also reported superior temporal cortex activation in autistic patients. Several regions of the cingulum have been associated with social cognition and language [215], which is a common deficiency in autistic subjects. Effective Connectivity of areas Postcentral_L, Frontal_Sup_Medial_R, Precuneus_R, SupraMarginal_R, Supp_Motor_Area_L, and Hippocampus_R, were identified to play important role in distinguishing between Individuals With autism and controls [216]. Regions Temporal_Sup_L, Postcentral_R, Frontal_Sup_Medial_R, Precuneus_R, Cingulum_Ant_R, and Hippocampus_R were among ASD-related regions highlighted by Chen. et. al [217]. Children with ASD also showed decreased functional connectivity in the right angular gyrus [218], as part of the cognition network. The same overlap with the selected brain regions can be seen with many other studies [97, 219–221].

A comparison of the experimental results of some other existing classification systems in the last five years can be found in Table 38. Our results are clearly above most literature for ABIDE-I dataset, taking into consideration that some are only on part of the dataset (not all sites). The added value of this work not only establishes

a better accuracy on a large dataset but also shows comprehensive experimentation of different blocks along the pipeline. Moreover, the 'average' performance across our novel dynamic connectivity feature *dFC* across all configurations, including other atlas and inferior strategies, is still above most literature (**78.09% Accuracy**, see Table 17). This is a powerful indication of the potential of our proposed work.

Table 38. Results summary of some existing ASD classification methods using ABIDE-I dataset.

Article	Used Classifier	Achieved accuracy
Abraham et al., 2017 [118]	SVM	67.0%
Guo et al., 2017 [120]	Deep neural networks with feature selection (DNN-FS)	86.4%
Kam et al., 2017 [122]	Discriminative restricted Boltzmann machines (DRBM)	80.8%
Spera et al., 2019 [142]	SVM	71.0%
Tang et al., 2019 [143]	SVM	62.6%
Wang et al., 2020 [222]	MLP and a voting strategy	74.5%
Rakić et al., 2020 [221]	Ensemble of classifiers	85.0%
Subah et al., 2021 [223]	DNN	87.0%
Al-Hiyali et al., 2021 [162]	SVM, KNN	85.9%
Yin et al., 2021 [164]	Autoencoders, CNN, DNN	79.2%
Chu et al., 2022 [165]	Multi-scale graph convolutional network (GCN)	79.5%
Yang et al., 2022 [166]	LR, SVM, DNN	69.4%

Several objectives were achieved through the framework presented. It can be used to determine the factors that contribute to the development of ASD in addition to providing an accurate diagnosis based on a publicly available dataset. As part of the framework's diagnosis, these spotted brain areas can be reported to the doctor early in order to help him or her make an informed decision. An important aspect of the work is gaining a better understanding of the abnormalities of the brain associated with autism. Additionally, the comprehensive experiments carried out in this study will allow future researchers to study the impact of different decisions in their ML pipeline on the output, thus filling an important knowledge gap that will enable the development of these CAD solutions to move forward more quickly. The system also has the advantage of being easily scalable: if a greater number of subjects are preprocessed, their features can be calculated independently, and if an additional imaging mode over a subject is required, such as structural magnetic resonance imaging, then it can be incorporated into the feature selection process.

CHAPTER VI

CONCLUSIONS AND FUTURE WORK

This dissertation introduces a couple of novel, fully-automated CAD systems, that can accurately detect ASD based on different magnetic resonance imaging modalities: DTI and rs-fMRI. The introduced CAD systems consist mainly of four primary stages: i) preprocessing, ii) feature calculation/ extraction, iii) feature engineering (feature representation, feature selection, ...etc) iv) classification using ML. The work tested different preprocessing strategies, different feature engineering methods, and different classification frameworks. The proposed models and techniques developed in this dissertation show promising overall results, as well as investigational results on alternative approaches. Following, the main contributions of each module are presented.

1 Summary of contributions

DTI-based ASD Diagnosis

In summary, the proposed diagnosis frameworks accomplish many objectives:

- Both imaging modalities used can be acquired at an early stage (for early children), and in one session, with no need for length repetitive exams, that best align with later stages.

- The presented algorithms provide automated quantitative measures of autism assessment, with no human bias as alternative techniques.

- The models provide high state-of-the-art balanced accuracies on a public dataset, with moderately large sample sizes (263 subjects for DTI, 884 for fMRI), which is in the upper range of those similar studies reported in the literature.

- Besides accomplishing a high diagnostic accuracy, it preserves interpretability: it has identified pairs of white matter areas that exhibit relative differences in ASD, as opposed to considering microstructural changes within contiguous WM regions, not only providing an ASD/TD diagnosis but also what areas contribute to such classification.
  Those spotted brain areas can be early reported with the framework diagnosis to the physician, who can now make a better-informed judgment. Providing for another way of looking at ASD as a disorder of brain connectivity, which should in turn lead to a better understanding of an autistic individual's behavior and the predictability of disorder development for those at risk. We believe that this is an important aspect that would lead to a better understanding of brain abnormalities associated with autism.

- We introduce a new feature representation, inspired by fMRI studies, that enhances the diagnostic accuracy of the classification. The new feature representation makes use of various WM information (FA, MD, AD, ...), and focuses more on the relational information, not the absolute one as in most previous studies. We were able to show the promise of this representation.

- The feature selection approach used in our system is also scalable: adding more subjects that can be preprocessed and feature calculated independently, and fusion of an extra modality, such as structural MRI features or resting-state functional MRI for the same subject, or even non-image data, can be easily integrated separately or jointly.

fMRI based ASD Diagnosis

As a result of the framework presented, a number of objectives were achieved.

- In addition to providing an accurate state-of-the-art diagnosis of ASD based on a public dataset, it can also be used for identifying the factors that contribute to such a diagnosis.

- In conjunction with the framework's diagnosis, these spotted brain areas can be reported to the physician early on, so that he or she may make a more informed decision in the future. Having a better understanding of the brain abnormalities associated with autism is one of the key aspects of this work.

- Moreover, the comprehensive experiments made in this work pave the way for the next researchers to understand the effect of different choices in their ML pipeline on the output, filling an important gap in knowledge that would help to speed the development of such CAD solutions.

- A further advantage of the system is that it easily scales up: more subjects can be preprocessed and their features calculated independently, and the addition of an additional mode of imaging over the same subject, such as structural MRI, can be incorporated into the feature selection stages.

2   Future Avenues

On the other hand, we stress that robust results were obtained and validated using only one publicly available dataset. Adding different datasets to the same model should guarantee the generalizability of our proposed frameworks, which can be an intriguing avenue for future research.

In conjunction with using one imaging modality, incorporating other modalities, with different aspects (shape, functionality, connectivity) to the classification framework is believed to provide more accurate and specific results, progressing towards an integrated system for autism assessment providing better interpretation and understanding of the underlying personalized diagnosis.

Moreover, more sophisticated medical interpretation is needed not only to map those affected brain areas to TD vs ASD, but also to correlate findings to different severity of ASD. In order to better understand and assess autism spectrum disorders, one way we believe in is combining behavior reports with the results of this study.

With new interpretable deep learning algorithms presented to the research community, a specially interesting future direction is to try to employ such new AI frameworks, in collaboration with its inventors, to ASD imaging dataset. It will require extra computation capabilities, but the venues it would open could be promising.

In addition, we used heterogeneous data in terms of age, to make use of the largest-possible number of subjects for efficient learning. We were able to deploy more sophisticated models on fMRI dataset, but not the same for DTI. We believe age can be an important factor affecting the heterogeneity in findings, and that segmenting the age population, focusing only on one age group for each model, would filter out the prominent effect for each age group and boost both the generalizability and accuracy of the algorithm.

Another important stratification is among different severity groups, while we provided a one-for-all solution across the whole spectrum, a careful dissecting of the autism spectrum (with ADOS or similar scores) may provide a better-tailored interpretability and understanding of the different traits of the autism phenotypes, allowing more distinction per scored module.

It is anticipated that further development of MRI imaging-based AI approaches will enhance subjectivity in the clinical information available for ASD diagnosis in the future, enabling more accurate and expedient diagnoses to be made, enhancing our understanding of the underlying diagnoses of autism and moving us towards an automated system for an autism assessment.

REFERENCES

[1]   U. Frith and F. Happé, "Autism spectrum disorder," Current biology **15**, R786–R790 (2005).

[2]   American Psychiatric Association, *Diagnostic and statistical manual of mental disorders, fifth edition (DSM-5)* (American Psychiatric Association, Arlington, 2013).

[3]   M. F. Casanova, A. El-Baz, and J. S. Suri, *Autism Imaging and Devices* (CRC Press, 2017).

[4]   M. Ismail, R. Keynton, M. Mostapha, A. ElTanboly, M. Casanova, G. Gimel'farb, and A. El-Baz, "Studying autism spectrum disorder with structural and diffusion magnetic resonance imaging: a survey," Frontiers in human neuroscience **10** (2016).

[5]   J. P. Leigh and J. Du, "Brief report: Forecasting the economic burden of autism in 2015 and 2025 in the united states," Journal of autism and developmental disorders **45**, 4135–4139 (2015).

[6]   R. Muhle, S. V. Trentacoste, and I. Rapin, "The genetics of autism," Pediatrics **113**, e472–e486 (2004).

[7]   S. Brieber, S. Neufang, N. Bruning, I. Kamp-Becker, H. Remschmidt, B. Herpertz-Dahlmann, G. R. Fink, and K. Konrad, "Structural brain abnormalities in adolescents with autism spectrum disorder and patients with attention deficit/hyperactivity disorder," Journal of Child Psychology and Psychiatry **48**, 1251–1258 (2007).

[8]   O. Dekhil, M. Ali, R. Haweel, Y. Elnakib, M. Ghazal, H. Hajjdiab, L. Fraiwan, A. Shalaby, A. Soliman, A. Mahmoud *et al.*, "A comprehensive framework for differentiating autism spectrum disorder from neurotypicals by fusing structural mri and resting state functional mri," in "Seminars in Pediatric Neurology," (Elsevier, 2020), p. 100805.

[9]   M. Noriuchi *et al.*, "Altered white matter fractional anisotropy and social impairment in children with autism spectrum disorder," Brain research **1362**, 141–149 (2010).

[10]   Y. ElNakieb, M. T. Ali, A. Elnakib, A. Shalaby, A. Soliman, A. Mahmoud, M. Ghazal, G. N. Barnes, and A. El-Baz, "The role of diffusion tensor mr imaging (dti) of the brain in diagnosing autism spectrum disorder: Promising results," Sensors **21**, 8171 (2021).

[11] F. Rafiee, R. Rezvani Habibabadi, M. Motaghi, D. M. Yousem, and I. J. Yousem, "Brain mri in autism spectrum disorder: Narrative review and recent advances," Journal of Magnetic Resonance Imaging **55**, 1613–1624 (2022).

[12] D.-Y. Song, C.-C. Topriceanu, D. C. Ilie-Ablachim, M. Kinali, and S. Bisdas, "Machine learning with neuroimaging data to identify autism spectrum disorder: a systematic review and meta-analysis," Neuroradiology **63**, 2057–2072 (2021).

[13] C. Lord, S. Risi, L. Lambrecht, E. H. Cook, B. L. Leventhal, P. C. DiLavore, A. Pickles, and M. Rutter, "The autism diagnostic observation schedule—generic: A standard measure of social and communication deficits associated with the spectrum of autism," Journal of autism and developmental disorders **30**, 205–223 (2000).

[14] C. Lord, M. Rutter, and A. Le Couteur, "Autism diagnostic interview-revised: a revised version of a diagnostic interview for caregivers of individuals with possible pervasive developmental disorders," Journal of autism and developmental disorders **24**, 659–685 (1994).

[15] T. Falkmer, K. Anderson, M. Falkmer, and C. Horlin, "Diagnostic procedures in autism spectrum disorders: a systematic literature review," European child & adolescent psychiatry **22**, 329–340 (2013).

[16] J. Hayes, T. Ford, R. McCabe, and G. Russell, "Autism diagnosis as a social process," Autism p. 13623613211030392 (2021).

[17] K. Gotham, A. Pickles, and C. Lord, "Trajectories of autism severity in children using standardized ados scores," Pediatrics **130**, e1278–e1284 (2012).

[18] P. Moridian, N. Ghassemi, M. Jafari, S. Salloum-Asfar, D. Sadeghi, M. Khodatars, A. Shoeibi, A. Khosravi, S. H. Ling, A. Subasi *et al.*, "Automatic autism spectrum disorder detection using artificial intelligence methods with mri neuroimaging: A review," arXiv preprint arXiv:2206.11233 (2022).

[19] A. Shoeibi, N. Ghassemi, M. Khodatars, P. Moridian, A. Khosravi, A. Zare, J. M. Gorriz, A. H. Chale-Chale, A. Khadem, and U. R. Acharya, "Automatic diagnosis of schizophrenia and attention deficit hyperactivity disorder in rsfmri modality using convolutional autoencoder model and interval type-2 fuzzy regression," arXiv preprint arXiv:2205.15858 (2022).

[20] D. Li, H.-O. Karnath, and X. Xu, "Candidate biomarkers in children with autism spectrum disorder: a review of mri studies," Neuroscience bulletin **33**, 219–237 (2017).

[21] A. L. Alexander *et al.*, "Diffusion tensor imaging of the brain," Neurotherapeutics **4**, 316–329 (2007).

[22] V. Rajagopalan, Z. Jiang, J. Stojanovic-Radic, G. Yue, E. P. Pioro, G. Wylie, and A. Das, "A basic introduction to diffusion tensor imaging mathematics and image processing steps," Brain Disord Ther **6**, 2 (2017).

[23] A. A. K. A. Razek, K. A. Baky, and E. Helmy, "Diffusion tensor imaging in characterization of mediastinal lymphadenopathy," Academic Radiology **29**, S165–S172 (2022).

[24] A. A. K. A. Razek, E. M. Helmy, H. Maher, and M. A. Kasem, "Diffusion tensor imaging of the lateral rectus muscle in duane retraction syndrome," Journal of computer assisted tomography **43**, 467–471 (2019).

[25] M. Lazar, L. M. Miles, J. S. Babb, and J. B. Donaldson, "Axonal deficits in young adults with high functioning autism and their impact on processing speed," NeuroImage: Clinical **4**, 417–425 (2014).

[26] M. Hrdlicka, J. Sanda, T. Urbanek, M. Kudr, I. Dudova, S. Kickova, L. Pospisilova, M. Mohaplova, A. Maulisova, P. Krsek *et al.*, "Diffusion tensor imaging and tractography in autistic, dysphasic, and healthy control children," Neuropsychiatric Disease and Treatment **15**, 2843 (2019).

[27] C. Lord, M. Elsabbagh, G. Baird, and J. Veenstra-Vanderweele, "Autism spectrum disorder," The lancet **392**, 508–520 (2018).

[28] S. S. Joudar, A. Albahri, and R. A. Hamid, "Triage and priority-based healthcare diagnosis using artificial intelligence for autism spectrum disorder and gene contribution: A systematic review," Computers in Biology and Medicine p. 105553 (2022).

[29] M. Xu, V. Calhoun, R. Jiang, W. Yan, and J. Sui, "Brain imaging-based machine learning in autism spectrum disorder: methods and applications," Journal of neuroscience methods **361**, 109271 (2021).

[30] R. Bellman, "Dynamic programming," Science **153**, 34–37 (1966).

[31] B. Sen, N. C. Borle, R. Greiner, and M. R. Brown, "A general prediction model for the detection of adhd and autism using structural and functional mri," PloS one **13** (2018).

[32] S. Haar, S. Berman, M. Behrmann, and I. Dinstein, "Anatomical abnormalities in autism?" Cerebral cortex **26**, 1440–1452 (2016).

[33] A. S. Heinsfeld, A. R. Franco, R. C. Craddock, A. Buchweitz, and F. Meneguzzi, "Identification of autism spectrum disorder using deep learning and the abide dataset," NeuroImage: Clinical **17**, 16–23 (2018).

[34] K. Polat and S. Güneş, "A new feature selection method on classification of medical datasets: Kernel f-score feature selection," Expert Systems with Applications **36**, 10367–10373 (2009).

[35] I. Guyon, S. Gunn, M. Nikravesh, and L. A. Zadeh, *Feature extraction: foundations and applications*, vol. 207 (Springer, 2008).

[36] C. Elkan, "The foundations of cost-sensitive learning," in "International joint conference on artificial intelligence," , vol. 17 (Lawrence Erlbaum Associates Ltd, 2001), vol. 17, pp. 973–978.

[37] M. Wasikowski and X.-w. Chen, "Combating the small sample class imbalance problem using feature selection," IEEE Transactions on knowledge and data engineering **22**, 1388–1400 (2009).

[38] N. S. Escanilla, L. Hellerstein, R. Kleiman, Z. Kuang, J. Shull, and D. Page, "Recursive feature elimination by sensitivity testing," in "2018 17th IEEE International Conference on Machine Learning and Applications (ICMLA)," (IEEE, 2018), pp. 40–47.

[39] M.-L. Huang, Y.-H. Hung, W. Lee, R.-K. Li, and B.-R. Jiang, "Svm-rfe based feature selection and taguchi parameters optimization for multiclass svm classifier," The Scientific World Journal **2014** (2014).

[40] J. Sui, R. Jiang, J. Bustillo, and V. Calhoun, "Neuroimaging-based individualized prediction of cognition and behavior for mental disorders and health: methods and promises," Biological psychiatry **88**, 818–828 (2020).

[41] H. S. Nogay and H. Adeli, "Machine learning (ml) for the diagnosis of autism spectrum disorder (asd) using brain imaging," Reviews in the Neurosciences **1** (2020).

[42] M. N. Parikh, H. Li, and L. He, "Enhancing diagnosis of autism with optimized machine learning models and personal characteristic data," Frontiers in computational neuroscience **13**, 9 (2019).

[43] S. Mori and J. Zhang, "Principles of diffusion tensor imaging and its applications to basic neuroscience research," Neuron **51**, 527–539 (2006).

[44] P. Hagmann, L. Jonasson, P. Maeder, J.-P. Thiran, V. J. Wedeen, and R. Meuli, "Understanding diffusion mr imaging techniques: from scalar diffusion-weighted imaging to diffusion tensor imaging and beyond," Radiographics **26**, S205–S223 (2006).

[45] L. J. O'Donnell and C.-F. Westin, "An introduction to diffusion tensor image analysis," Neurosurgery Clinics **22**, 185–196 (2011).

[46] D. K. Shukla *et al.*, "Tract-specific analyses of diffusion tensor imaging show widespread white matter compromise in autism spectrum disorder," Journal of Child Psychology and Psychiatry **52**, 286–295 (2011).

[47] P. J. Basser, "New histological and physiological stains derived from diffusion-tensor mr images," Annals of the New York Academy of Sciences **820**, 123–138 (1997).

[48] N. Barnea-Goraly *et al.*, "White matter structure in autism: preliminary evidence from diffusion tensor imaging," Biological Psychiatry **55**, 323–326 (2004).

[49] A. L. Alexander, J. E. Lee, M. Lazar, R. Boudos, M. B. DuBray, T. R. Oakes, J. N. Miller, J. Lu, E.-K. Jeong, W. M. McMahon *et al.*, "Diffusion tensor imaging of the corpus callosum in autism," Neuroimage **34**, 61–73 (2007).

[50] J. E. Lee *et al.*, "Diffusion tensor imaging of white matter in the superior temporal gyrus and temporal stem in autism," Neuroscience Letters **424**, 127–132 (2007).

[51] S. K. Sundaram *et al.*, "Diffusion tensor imaging of frontal lobe in autism spectrum disorder," Cerebral Cortex **18**, 2659–2665 (2008).

[52] W. B. Groen, J. K. Buitelaar, R. J. Van Der Gaag, and M. P. Zwiers, "Pervasive microstructural abnormalities in autism: a dti study," Journal of psychiatry & neuroscience: JPN **36**, 32 (2011).

[53] B. G. Travers, N. Adluru, C. Ennis, D. P. Tromp, D. Destiche, S. Doran, E. D. Bigler, N. Lange, J. E. Lainhart, and A. L. Alexander, "Diffusion tensor imaging in autism spectrum disorder: a review," Autism Research **5**, 289–313 (2012).

[54] Y. Aoki, O. Abe, Y. Nippashi, and H. Yamasue, "Comparison of white matter integrity between autism spectrum disorder subjects and typically developing individuals: a meta-analysis of diffusion tensor imaging tractography studies," Molecular autism **4**, 25 (2013).

[55] M. Mostapha *et al.*, "Towards non-invasive image-based early diagnosis of autism," in "International Conference on Medical Image Computing and Computer-Assisted Intervention," (Springer, 2015), pp. 160–168.

[56] R. A. Vasa, S. H. Mostofsky, and J. B. Ewen, "The disrupted connectivity hypothesis of autism spectrum disorders: time for the next phase in research," Biological Psychiatry: Cognitive Neuroscience and Neuroimaging **1**, 245–252 (2016).

[57] M. Kuno, Y. Hirano, A. Nakagawa, K. Asano, F. Oshima, S. Nagaoka, K. Matsumoto, Y. Masuda, M. Iyo, and E. Shimizu, "White matter features associated with autistic traits in obsessive-compulsive disorder," Frontiers in psychiatry **9**, 216 (2018).

[58] M. Jung, Y. Tu, C. A. Lang, A. Ortiz, J. Park, K. Jorgenson, X.-J. Kong, and J. Kong, "Decreased structural connectivity and resting-state brain activity in the lateral occipital cortex is associated with social communication deficits in boys with autism spectrum disorder," Neuroimage **190**, 205–212 (2019).

[59] T. Yamasaki, T. Maekawa, T. Fujita, and S. Tobimatsu, "Connectopathy in autism spectrum disorders: a review of evidence from visual evoked potentials

and diffusion magnetic resonance imaging," Frontiers in neuroscience **11**, 627 (2017).

[60] P. Rane, D. Cochran, S. M. Hodge, C. Haselgrove, D. Kennedy, and J. A. Frazier, "Connectivity in autism: a review of mri connectivity studies," Harvard review of psychiatry **23**, 223 (2015).

[61] M. Valenti, M. C. Pino, M. Mazza, G. Panzarino, C. Di Paolantonio, and A. Verrotti, "Abnormal structural and functional connectivity of the corpus callosum in autism spectrum disorders: A review," Review Journal of Autism and Developmental Disorders **7**, 46–62 (2020).

[62] K. McLaughlin, B. G. Travers, O. I. Dadalko, D. C. Dean III, D. Tromp, N. Adluru, D. Destiche, A. Freeman, M. D. Prigge, A. Froehlich *et al.*, "Longitudinal development of thalamic and internal capsule microstructure in autism spectrum disorder," Autism Research **11**, 450–462 (2018).

[63] S. Saaybi, N. AlArab, S. Hannoun, M. Saade, R. Tutunji, C. Zeeni, R. Shbarou, R. Hourani, and R.-M. Boustany, "Pre-and post-therapy assessment of clinical outcomes and white matter integrity in autism spectrum disorder: pilot study," Frontiers in neurology **10**, 877 (2019).

[64] V. Vogan, B. Morgan, R. Leung, E. Anagnostou, K. Doyle-Thomas, and M. Taylor, "Widespread white matter differences in children and adolescents with autism spectrum disorder," Journal of autism and developmental disorders **46**, 2138–2147 (2016).

[65] L. Zhang, R. Ma, Y. Yuan, D. Lian, X. Qi, N. Zheng, and K. Li, "The value of diffusion tensor imaging for differentiating autism spectrum disorder with language delay from developmental language disorder among toddlers," Medicine **98** (2019).

[66] S. Solso, R. Xu, J. Proudfoot, D. J. Hagler Jr, K. Campbell, V. Venkatraman, C. C. Barnes, C. Ahrens-Barbeau, K. Pierce, A. Dale *et al.*, "Diffusion tensor imaging provides evidence of possible axonal overconnectivity in frontal lobes in autism spectrum disorder toddlers," Biological psychiatry **79**, 676–684 (2016).

[67] M. Ouyang, H. Cheng, V. Mishra, G. Gong, M. W. Mosconi, J. Sweeney, Y. Peng, and H. Huang, "Atypical age-dependent effects of autism on white matter microstructure in children of 2–7 years," Human brain mapping **37**, 819–832 (2016).

[68] A. Thompson, A. Shahidiani, A. Fritz, J. O'Muircheartaigh, L. Walker, V. D'Almeida, C. Murphy, E. Daly, D. Murphy, S. Williams *et al.*, "Age-related differences in white matter diffusion measures in autism spectrum condition," Molecular autism **11**, 1–10 (2020).

[69] V. J. Schmithorst, M. Wilke, B. J. Dardzinski, and S. K. Holland, "Correlation of white matter diffusivity and anisotropy with age during childhood and adolescence: a cross-sectional diffusion-tensor mr imaging study," Radiology **222**, 212 (2002).

[70] S. Payabvash, E. M. Palacios, J. P. Owen, M. B. Wang, T. Tavassoli, M. Gerdes, A. Brandes-Aitken, D. Cuneo, E. J. Marco, and P. Mukherjee, "White matter connectome edge density in children with autism spectrum disorders: potential imaging biomarkers using machine-learning models," Brain connectivity **9**, 209–220 (2019).

[71] M. Ingalhalikar, D. Parker, L. Bloy, T. P. Roberts, and R. Verma, "Diffusion based abnormality markers of pathology: toward learned diagnostic prediction of asd," Neuroimage **57**, 918–927 (2011).

[72] H. Li, Z. Xue, T. M. Ellmore, R. E. Frye, and S. T. Wong, "Identification of faulty dti-based sub-networks in autism using network regularized svm," in "2012 9th IEEE International Symposium on Biomedical Imaging (ISBI)," (IEEE, 2012), pp. 550–553.

[73] Y. Jin, C.-Y. Wee, F. Shi, K.-H. Thung, D. Ni, P.-T. Yap, and D. Shen, "Identification of infants at high-risk for autism spectrum disorder using multiparameter multiscale white matter connectivity networks," Human brain mapping **36**, 4880–4896 (2015).

[74] F. Zhang, P. Savadjiev, W. Cai, Y. Song, Y. Rathi, B. Tunç, D. Parker, T. Kapur, R. T. Schultz, N. Makris *et al.*, "Whole brain white matter connectivity analysis using machine learning: an application to autism," NeuroImage **172**, 826–837 (2018).

[75] B. Qin, L. Wang, Y. Zhang, J. Cai, J. Chen, and T. Li, "Enhanced topological network efficiency in preschool autism spectrum disorder: a diffusion tensor imaging study," Frontiers in Psychiatry **9**, 278 (2018).

[76] M. Saad and S. M. R. Islam, "Brain connectivity network analysis and classifications from diffusion tensor imaging," in "2019 International Conference on Robotics, Electrical and Signal Processing Techniques (ICREST)," (IEEE, 2019), pp. 422–427.

[77] N. Adluru, C. Hinrichs, M. K. Chung, J.-E. Lee, V. Singh, E. D. Bigler, N. Lange, J. E. Lainhart, and A. L. Alexander, "Classification in dti using shapes of white matter tracts," in "2009 Annual International Conference of the IEEE Engineering in Medicine and Biology Society," (IEEE, 2009), pp. 2719–2722.

[78] M. Khosla, K. Jamison, A. Kuceyeski, and M. R. Sabuncu, "3d convolutional neural networks for classification of functional connectomes," in "Deep Learning in Medical Image Analysis and Multimodal Learning for Clinical Decision Support," (Springer, 2018), pp. 137–145.

[79] M. An, H. P. Ho, L. Staib, K. Pelphrey, and J. Duncan, "Multimodal mri analysis of brain subnetworks in autism using multi-view em," in "2010 Conference Record of the Forty Fourth Asilomar Conference on Signals, Systems and Computers," (IEEE, 2010), pp. 786–789.

[80] O. Dekhil, M. Ali, Y. El-Nakieb, A. Shalaby, A. Soliman, A. Switala, A. Mahmoud, M. Ghazal, H. Hajjdiab, M. F. Casanova *et al.*, "A personalized autism diagnosis cad system using a fusion of structural mri and resting-state functional mri data," Frontiers in Psychiatry **10** (2019).

[81] G. Deshpande, L. E. Libero, K. R. Sreenivasan, H. D. Deshpande, and R. K. Kana, "Identification of neural connectivity signatures of autism using machine learning," Frontiers in human neuroscience **7**, 670 (2013).

[82] A. Crimi, L. Dodero, V. Murino, and D. Sona, "Case-control discrimination through effective brain connectivity," in "2017 IEEE 14th International Symposium on Biomedical Imaging (ISBI 2017)," (Ieee, 2017), pp. 970–973.

[83] N. S. Dsouza, M. B. Nebel, D. Crocetti, J. Robinson, S. Mostofsky, and A. Venkataraman, "M-gcn: A multimodal graph convolutional network to integrate functional and structural connectomics data to predict multidimensional phenotypic characterizations," in "Medical Imaging with Deep Learning," (PMLR, 2021), pp. 119–130.

[84] A. Irimia, X. Lei, C. M. Torgerson, Z. J. Jacokes, S. Abe, and J. D. Van Horn, "Support vector machines, multidimensional scaling and magnetic resonance imaging reveal structural brain abnormalities associated with the interaction between autism spectrum disorder and sex," Frontiers in Computational Neuroscience **12**, 93 (2018).

[85] A. Eill, A. Jahedi, Y. Gao, J. S. Kohli, C. H. Fong, S. Solders, R. A. Carper, F. Valafar, B. A. Bailey, and R.-A. Müller, "Functional connectivities are more informative than anatomical variables in diagnostic classification of autism," Brain connectivity **9**, 604–612 (2019).

[86] T.-H. Pham, J. Vicnesh, J. K. E. Wei, S. L. Oh, N. Arunkumar, E. W. Abdulhay, E. J. Ciaccio, and U. R. Acharya, "Autism spectrum disorder diagnostic system using hos bispectrum with eeg signals," International journal of environmental research and public health **17**, 971 (2020).

[87] D. M. Cole, S. M. Smith, and C. F. Beckmann, "Advances and pitfalls in the analysis and interpretation of resting-state fmri data," Frontiers in systems neuroscience p. 8 (2010).

[88] R. Haweel, A. Shalaby, A. Mahmoud, N. Seada, S. Ghoniemy, M. Ghazal, M. F. Casanova, G. N. Barnes, and A. El-Baz, "A robust dwt–cnn-based cad system for early diagnosis of autism using task-based fmri," Medical physics **48**, 2315–2326 (2021).

[89] M. Khodatars, A. Shoeibi, D. Sadeghi, N. Ghaasemi, M. Jafari, P. Moridian, A. Khadem, R. Alizadehsani, A. Zare, Y. Kong *et al.*, "Deep learning for neuroimaging-based diagnosis and rehabilitation of autism spectrum disorder: a review," Computers in Biology and Medicine **139**, 104949 (2021).

[90] R.-A. Müller and I. Fishman, "Brain connectivity and neuroimaging of social networks in autism," Trends in cognitive sciences **22**, 1103–1116 (2018).

[91] G. S. Dichter, "Functional magnetic resonance imaging of autism spectrum disorders," Dialogues in clinical neuroscience (2022).

[92] K. Pierce and E. Redcay, "Fusiform function in children with an autism spectrum disorder is a matter of "who"," Biological psychiatry **64**, 552–560 (2008).

[93] J. D. Herrington, C. Nymberg, and R. T. Schultz, "Biological motion task performance predicts superior temporal sulcus activity," Brain and cognition **77**, 372–381 (2011).

[94] S.-J. Weng, M. Carrasco *et al.*, "Neural activation to emotional faces in adolescents with autism spectrum disorders," Journal of Child Psychology and Psychiatry **52**, 296–305 (2011).

[95] S.-V. Zeeland, A. Ashley, M. Dapretto, D. G. Ghahremani, R. A. Poldrack, and S. Y. Bookheimer, "Reward processing in autism," Autism Research **3**, 53–67 (2010).

[96] K. E. Lawrence, L. M. Hernandez, J. Eilbott, A. Jack, E. Aylward, N. Gaab, J. D. Van Horn, R. A. Bernier, D. H. Geschwind, J. C. McPartland *et al.*, "Neural responsivity to social rewards in autistic female youth," Translational psychiatry **10**, 1–12 (2020).

[97] R. C. Philip, M. R. Dauvermann, H. C. Whalley, K. Baynham, S. M. Lawrie, and A. C. Stanfield, "A systematic review and meta-analysis of the fmri investigation of autism spectrum disorders," Neuroscience & Biobehavioral Reviews **36**, 901–942 (2012).

[98] W. K. Lau, M.-K. Leung, and B. W. Lau, "Resting-state abnormalities in autism spectrum disorders: a meta-analysis," Scientific reports **9**, 1–8 (2019).

[99] J.-W. Sun, R. Fan, Q. Wang, Q.-Q. Wang, X.-Z. Jia, and H.-B. Ma, "Identify abnormal functional connectivity of resting state networks in autism spectrum disorder and apply to machine learning-based classification," Brain Research **1757**, 147299 (2021).

[100] C. He, Y. Chen, T. Jian, H. Chen, X. Guo, J. Wang, L. Wu, H. Chen, and X. Duan, "Dynamic functional connectivity analysis reveals decreased variability of the default-mode network in developing autistic brain," Autism Research **11**, 1479–1493 (2018).

[101] J.-C. Weng, N. Y. Wang, C.-J. Li, and H.-L. S. Wang, "Resting-state functional connectivity within default mode network in chinese-speaking children with specific learning disabilities," Neuropsychiatry (2018).

[102] S. Nair, R. J. Jao Keehn, M. M. Berkebile, J. O. Maximo, N. Witkowska, and R.-A. Müller, "Local resting state functional connectivity in autism: site and cohort variability and the effect of eye status," Brain Imaging and Behavior **12**, 168–179 (2018).

[103] J. Wang, X. Wang, R. Wang, X. Duan, H. Chen, C. He, J. Zhai, L. Wu, and H. Chen, "Atypical resting-state functional connectivity of intra/inter-sensory networks is related to symptom severity in young boys with autism spectrum disorder," Frontiers in Physiology **12**, 626338 (2021).

[104] J.-J. Paakki *et al.*, "Alterations in regional homogeneity of resting-state brain activity in autism spectrum disorders," Brain research **1321**, 169–179 (2010).

[105] L. Q. Uddin *et al.*, "Salience network–based classification and prediction of symptom severity in children with autism," JAMA psychiatry **70**, 869–879 (2013).

[106] T. Itahashi, T. Yamada, H. Watanabe, M. Nakamura, D. Jimbo, S. Shioda, K. Toriizuka, N. Kato, and R. Hashimoto, "Altered network topologies and hub organization in adults with autism: a resting-state fmri study," PloS one **9**, e94115 (2014).

[107] M. A. Just, V. L. Cherkassky, T. A. Keller, and N. J. Minshew, "Cortical activation and synchronization during sentence comprehension in high-functioning autism: evidence of underconnectivity," Brain **127**, 1811–1821 (2004).

[108] K. Alaerts *et al.*, "Sex differences in autism: a resting-state fmri investigation of functional brain connectivity in males and females," Social cognitive and affective neuroscience **11**, 1002–1016 (2016).

[109] A. Rausch, W. Zhang, K. V. Haak, M. Mennes, E. J. Hermans, E. van Oort, G. van Wingen, C. F. Beckmann, J. K. Buitelaar, and W. B. Groen, "Altered functional connectivity of the amygdaloid input nuclei in adolescents and young adults with autism spectrum disorder: a resting state fmri study," Molecular autism **7**, 1–13 (2016).

[110] J. M. Tyszka, D. P. Kennedy, L. K. Paul, and R. Adolphs, "Largely typical patterns of resting-state functional connectivity in high-functioning adults with autism," Cerebral cortex **24**, 1894–1905 (2013).

[111] M. Plitt, K. A. Barnes, and A. Martin, "Functional connectivity classification of autism identifies highly predictive brain features but falls short of biomarker standards," NeuroImage: Clinical **7**, 359–366 (2015).

[112] J. O. Maximo, C. L. Keown, A. Nair, and R.-A. Müller, "Approaches to local connectivity in autism using resting state functional connectivity mri," Frontiers in human neuroscience **7**, 605 (2013).

[113] K. Jann, L. M. Hernandez, D. Beck-Pancer, R. McCarron, R. X. Smith, M. Dapretto, and D. J. Wang, "Altered resting perfusion and functional connectivity of default mode network in youth with autism spectrum disorder," Brain and behavior **5**, e00358 (2015).

[114] N. M. Kleinhans, M. A. Reiter, E. Neuhaus, G. Pauley, N. Martin, S. Dager, and A. Estes, "Subregional differences in intrinsic amygdala hyperconnectivity and hypoconnectivity in autism spectrum disorder," Autism Research **9**, 760–772 (2016).

[115] A. Hahamy, M. Behrmann, and R. Malach, "The idiosyncratic brain: distortion of spontaneous connectivity patterns in autism spectrum disorder," Nature neuroscience **18**, 302–309 (2015).

[116] A. Di Martino, C.-G. Yan, Q. Li, E. Denio, F. X. Castellanos, K. Alaerts, J. S. Anderson, M. Assaf, S. Y. Bookheimer, M. Dapretto *et al.*, "The autism brain imaging data exchange: towards a large-scale evaluation of the intrinsic brain architecture in autism," Molecular psychiatry **19**, 659–667 (2014).

[117] K. Supekar, L. Q. Uddin, A. Khouzam, J. Phillips, W. D. Gaillard, L. E. Kenworthy, B. E. Yerys, C. J. Vaidya, and V. Menon, "Brain hyperconnectivity in children with autism and its links to social deficits," Cell reports **5**, 738–747 (2013).

[118] A. Abraham, M. P. Milham, A. Di Martino, R. C. Craddock, D. Samaras, B. Thirion, and G. Varoquaux, "Deriving reproducible biomarkers from multi-site resting-state data: An autism-based example," NeuroImage **147**, 736–745 (2017).

[119] R. W. Emerson *et al.*, "Functional neuroimaging of high-risk 6-month-old infants predicts a diagnosis of autism at 24 months of age," Science translational medicine **9**, eaag2882 (2017).

[120] X. Guo, K. C. Dominick, A. A. Minai, H. Li, C. A. Erickson, and L. J. Lu, "Diagnosing autism spectrum disorder from brain resting-state functional connectivity patterns using a deep neural network with a novel feature selection method," Frontiers in neuroscience **11**, 460 (2017).

[121] A. Jahedi, C. A. Nasamran, B. Faires, J. Fan, and R.-A. Müller, "Distributed intrinsic functional connectivity patterns predict diagnostic status in large autism cohort," Brain connectivity **7**, 515–525 (2017).

[122] T.-E. Kam, H.-I. Suk, and S.-W. Lee, "Multiple functional networks modeling for autism spectrum disorder diagnosis," Human brain mapping **38**, 5804–5821 (2017).

[123] M. Sadeghi, R. Khosrowabadi, F. Bakouie, H. Mahdavi, C. Eslahchi, and H. Pouretemad, "Screening of autism based on task-free fmri using graph theoretical approach," Psychiatry Research: Neuroimaging **263**, 48–56 (2017).

[124] V. Subbaraju, M. B. Suresh, S. Sundaram, and S. Narasimhan, "Identifying differences in brain activities and an accurate detection of autism spectrum disorder using resting state functional-magnetic resonance imaging: A spatial filtering approach," Medical image analysis **35**, 375–389 (2017).

[125] R. Tejwani, A. Liska, H. You, J. Reinen, and P. Das, "Autism classification using brain functional connectivity dynamics and machine learning," arXiv preprint arXiv:1712.08041 (2017).

[126] X.-a. Bi, Y. Wang, Q. Shu, Q. Sun, and Q. Xu, "Classification of autism spectrum disorder using random support vector machine cluster," Frontiers in genetics **9**, 18 (2018).

[127] A. J. Fredo, A. Jahedi, M. Reiter, and R.-A. Müller, "Diagnostic classification of autism using resting-state fmri data and conditional random forest," Age (years) **12**, 6–41 (2018).

[128] X. Li, N. C. Dvornek, J. Zhuang, P. Ventola, and J. S. Duncan, "Brain biomarker interpretation in asd using deep learning and fmri," in "International conference on medical image computing and computer-assisted intervention," (Springer, 2018), pp. 206–214.

[129] A. Bernas, A. P. Aldenkamp, and S. Zinger, "Wavelet coherence-based classifier: A resting-state functional mri study on neurodynamics in adolescents with high-functioning autism," Computer methods and programs in biomedicine **154**, 143–151 (2018).

[130] R. Bhaumik, A. Pradhan, S. Das, and D. K. Bhaumik, "Predicting autism spectrum disorder using domain-adaptive cross-site evaluation," Neuroinformatics **16**, 197–205 (2018).

[131] O. Dekhil, H. Hajjdiab, A. Shalaby, M. T. Ali, B. Ayinde, A. Switala, A. Elshamekh, M. Ghazal, R. Keynton, G. Barnes *et al.*, "Using resting state functional mri to build a personalized autism diagnosis system," PloS one **13**, e0206351 (2018).

[132] Z. Xiao, C. Wang, N. Jia, and J. Wu, "Sae-based classification of school-aged children with autism spectrum disorders using functional magnetic resonance imaging," Multimedia Tools and Applications **77**, 22809–22820 (2018).

[133] X. Yang, M. S. Islam, and A. A. Khaled, "Functional connectivity magnetic resonance imaging classification of autism spectrum disorder using the multisite abide dataset," in "2019 IEEE EMBS International Conference on Biomedical & Health Informatics (BHI)," (IEEE, 2019), pp. 1–4.

[134] C. Wang, Z. Xiao, B. Wang, and J. Wu, "Identification of autism based on svm-rfe and stacked sparse auto-encoder," Ieee Access **7**, 118030–118036 (2019).

[135] C. Wang, Z. Xiao, and J. Wu, "Functional connectivity-based classification of autism and control using svm-rfecv on rs-fmri data," Physica Medica **65**, 99–105 (2019).

[136] M. A. Aghdam, A. Sharifi, and M. M. Pedram, "Diagnosis of autism spectrum disorders in young children based on resting-state functional magnetic resonance imaging data using convolutional neural networks," Journal of digital imaging **32**, 899–918 (2019).

[137] H. Huang, X. Liu, Y. Jin, S.-W. Lee, C.-Y. Wee, and D. Shen, "Enhancing the representation of functional connectivity networks by fusing multi-view information for autism spectrum disorder diagnosis," Human brain mapping **40**, 833–854 (2019).

[138] E. Jun, E. Kang, J. Choi, and H.-I. Suk, "Modeling regional dynamics in low-frequency fluctuation and its application to autism spectrum disorder diagnosis," NeuroImage **184**, 669–686 (2019).

[139] T. Eslami, V. Mirjalili, A. Fong, A. R. Laird, and F. Saeed, "Asd-diagnet: a hybrid learning approach for detection of autism spectrum disorder using fmri data," Frontiers in neuroinformatics **13**, 70 (2019).

[140] S. Mostafa, L. Tang, and F.-X. Wu, "Diagnosis of autism spectrum disorder based on eigenvalues of brain networks," Ieee Access **7**, 128474–128486 (2019).

[141] Y. Song, T. M. Epalle, and H. Lu, "Characterizing and predicting autism spectrum disorder by performing resting-state functional network community pattern analysis," Frontiers in human neuroscience **13**, 203 (2019).

[142] G. Spera, A. Retico, P. Bosco, E. Ferrari, L. Palumbo, P. Oliva, F. Muratori, and S. Calderoni, "Evaluation of altered functional connections in male children with autism spectrum disorders on multiple-site data optimized with machine learning," Frontiers in psychiatry **10**, 620 (2019).

[143] L. Tang, S. Mostafa, B. Liao, and F.-X. Wu, "A network clustering based feature selection strategy for classifying autism spectrum disorder," BMC medical genomics **12**, 1–10 (2019).

[144] B. Yamagata, T. Itahashi, J. Fujino, H. Ohta, M. Nakamura, N. Kato, M. Mimura, R.-i. Hashimoto, and Y. Aoki, "Machine learning approach to identify a resting-state functional connectivity pattern serving as an endophenotype of autism spectrum disorder," Brain imaging and behavior **13**, 1689–1698 (2019).

[145] N. Chaitra, P. Vijaya, and G. Deshpande, "Diagnostic prediction of autism spectrum disorder using complex network measures in a machine learning framework," Biomedical Signal Processing and Control **62**, 102099 (2020).

[146] G. Fan, Y. Chen, Y. Chen, M. Yang, J. Wang, C. Li, Y. Li, and T. Liu, "Abnormal brain regions in two-group cross-location dynamics model of autism," Ieee Access **8**, 94526–94534 (2020).

[147] Y. Liu, L. Xu, J. Li, J. Yu, and X. Yu, "Attentional connectivity-based prediction of autism using heterogeneous rs-fmri data from cc200 atlas," Experimental Neurobiology **29**, 27 (2020).

[148] J. Hu, L. Cao, T. Li, B. Liao, S. Dong, and P. Li, "Interpretable learning approaches in resting-state functional connectivity analysis: the case of autism spectrum disorder," Computational and Mathematical Methods in Medicine **2020** (2020).

[149] Z. Sherkatghanad, M. Akhondzadeh, S. Salari, M. Zomorodi-Moghadam, M. Abdar, U. R. Acharya, R. Khosrowabadi, and V. Salari, "Automated detection of autism spectrum disorder using a convolutional neural network," Frontiers in neuroscience **13**, 1325 (2020).

[150] R. M. Thomas, S. Gallo, L. Cerliani, P. Zhutovsky, A. El-Gazzar, and G. Van Wingen, "Classifying autism spectrum disorder using the temporal statistics of resting-state functional mri data with 3d convolutional neural networks," Frontiers in psychiatry **11**, 440 (2020).

[151] Z. Jiao, H. Li, and Y. Fan, "Improving diagnosis of autism spectrum disorder and disentangling its heterogeneous functional connectivity patterns using capsule networks," in "2020 IEEE 17th International Symposium on Biomedical Imaging (ISBI)," (IEEE, 2020), pp. 1331–1334.

[152] W. Liu, M. Liu, D. Yang, M. Wang, and T. Tao, "Automatic diagnosis of autism based on functional magnetic resonance imaging and elastic net," in "2020 IEEE 5th Information Technology and Mechatronics Engineering Conference (ITOEC)," (IEEE, 2020), pp. 104–108.

[153] J. Liu, Y. Sheng, W. Lan, R. Guo, Y. Wang, and J. Wang, "Improved asd classification using dynamic functional connectivity and multi-task feature selection," Pattern Recognition Letters **138**, 82–87 (2020).

[154] L. Zhang, X.-H. Wang, and L. Li, "Diagnosing autism spectrum disorder using brain entropy: A fast entropy method," Computer Methods and Programs in Biomedicine **190**, 105240 (2020).

[155] J. F. A. Ronicko, J. Thomas, P. Thangavel, V. Koneru, G. Langs, and J. Dauwels, "Diagnostic classification of autism using resting-state fmri data improves with full correlation functional brain connectivity compared to partial correlation," Journal of Neuroscience Methods **345**, 108884 (2020).

[156] N. A. Khan, S. A. Waheeb, A. Riaz, and X. Shang, "A three-stage teacher, student neural networks and sequential feed forward selection-based feature selection approach for the classification of autism spectrum disorder," Brain sciences **10**, 754 (2020).

[157] M. A. Reiter, A. Jahedi, A. Fredo, I. Fishman, B. Bailey, and R.-A. Müller, "Performance of machine learning classification models of autism using resting-state fmri is contingent on sample heterogeneity," Neural Computing and Applications **33**, 3299–3310 (2021).

[158] K. Devika and V. R. M. Oruganti, "A machine learning approach for diagnosing neurological disorders using longitudinal resting-state fmri," in "2021 11th International Conference on Cloud Computing, Data Science & Engineering (Confluence)," (IEEE, 2021), pp. 494–499.

[159] M. S. Ahammed, S. Niu, M. R. Ahmed, J. Dong, X. Gao, and Y. Chen, "Bag-of-features model for asd fmri classification using svm," in "2021 Asia-Pacific Conference on Communications Technology and Computer Science (ACCTCS)," (IEEE, 2021), pp. 52–57.

[160] M. S. Ahammed, S. Niu, M. R. Ahmed, J. Dong, X. Gao, and Y. Chen, "Dark-asdnet: Classification of asd on functional mri using deep neural network," Frontiers in Neuroinformatics **15**, 635657 (2021).

[161] M. Graña and M. Silva, "Impact of machine learning pipeline choices in autism prediction from functional connectivity data," International journal of neural systems **31**, 2150009 (2021).

[162] M. I. Al-Hiyali, N. Yahya, I. Faye, Z. Khan, and K. Alsaih, "Classification of bold fmri signals using wavelet transform and transfer learning for detection of autism spectrum disorder," in "2020 IEEE-EMBS Conference on Biomedical Engineering and Sciences (IECBES)," (IEEE, 2021), pp. 94–98.

[163] M. Pominova, E. Kondrateva, M. Sharaev, A. Bernstein, and E. Burnaev, "Fader networks for domain adaptation on fmri: abide-ii study," in "Thirteenth International Conference on Machine Vision," , vol. 11605 (SPIE, 2021), vol. 11605, pp. 570–577.

[164] W. Yin, S. Mostafa, and F.-X. Wu, "Diagnosis of autism spectrum disorder based on functional brain networks with deep learning," Journal of Computational Biology **28**, 146–165 (2021).

[165] Y. Chu, G. Wang, L. Cao, L. Qiao, and M. Liu, "Multi-scale graph representation learning for autism identification with functional mri," Frontiers in Neuroinformatics **15**, 802305 (2022).

[166] X. Yang, N. Zhang, and P. Schrader, "A study of brain networks for autism spectrum disorder classification using resting-state functional connectivity," Machine Learning with Applications **8**, 100290 (2022).

[167] Y. A. Elnakieb, M. T. Ali, A. Soliman, A. H. Mahmoud, A. M. Shalaby, N. S. Alghamdi, M. Ghazal, A. Khalil, A. Switala, R. S. Keynton *et al.*, "Computer aided autism diagnosis using diffusion tensor imaging," IEEE Access **8**, 191298–191308 (2020).

[168] J. J. Wolff, H. Gu, G. Gerig, J. T. Elison, M. Styner, S. Gouttard, K. N. Botteron, S. R. Dager, G. Dawson, A. M. Estes *et al.*, "Differences in white matter fiber tract development present from 6 to 24 months in infants with autism," American Journal of Psychiatry **169**, 589–600 (2012).

[169] N. Yahata, J. Morimoto, R. Hashimoto, G. Lisi, K. Shibata, Y. Kawakubo, H. Kuwabara, M. Kuroda, T. Yamada, F. Megumi *et al.*, "A small number of abnormal brain connections predicts adult autism spectrum disorder," Nature communications **7**, 11254 (2016).

[170] A. Kunimatsu *et al.*, "The optimal trackability threshold of fractional anisotropy for diffusion tensor tractography of the corticospinal tract," Magnetic Resonance in Medical Sciences **3**, 11–17 (2004).

[171] N. Bodammer *et al.*, "Eddy current correction in diffusion-weighted imaging using pairs of images acquired with opposite diffusion gradient polarity," Magnetic Resonance in Medicine **51**, 188–193 (2004).

[172] S. M. Smith, "Fast robust automated brain extraction," Human Brain Mapping **17**, 143–155 (2002).

[173] A. Alansary *et al.*, "Infant brain extraction in T1-weighted MR images using BET and refinement using LCDG and MGRF models," IEEE Journal of Biomedical and Health Informatics **20**, 925–935 (2016).

[174] S. Mori *et al.*, *MRI atlas of human white matter* (Elsevier, Amsterdam, 2005).

[175] Y. Wang, A. Gupta, Z. Liu, H. Zhang, M. L. Escolar, J. H. Gilmore, S. Gouttard, P. Fillard, E. Maltbie, G. Gerig *et al.*, "Dti registration in atlas based fiber analysis of infantile krabbe disease," Neuroimage **55**, 1577–1586 (2011).

[176] "National Institutes of Health. National Database for Autism Research (NDAR): https://ndar.nih.gov/edit_collection.html?id=2021," .

[177] S. S. Panesar, F.-C. Yeh, C. P. Deibert, D. Fernandes-Cabral, V. Rowthu, P. Celtikci, E. Celtikci, W. D. Hula, S. Pathak, and J. C. Fernández-Miranda, "A diffusion spectrum imaging-based tractographic study into the anatomical subdivision and cortical connectivity of the ventral external capsule: uncinate and inferior fronto-occipital fascicles," Neuroradiology **59**, 971–987 (2017).

[178] S. E. Urger, M. D. De Bellis, S. R. Hooper, D. P. Woolley, S. D. Chen, and J. Provenzale, "The superior longitudinal fasciculus in typically developing children and adolescents: diffusion tensor imaging and neuropsychological correlates," Journal of Child Neurology **30**, 9–20 (2015).

[179] Ž. Krsnik, V. Majić, L. Vasung, H. Huang, and I. Kostović, "Growth of thalamocortical fibers to the somatosensory cortex in the human fetal brain," Frontiers in Neuroscience **11**, 233 (2017).

[180] J. R. Pryweller, K. B. Schauder, A. W. Anderson, J. L. Heacock, J. H. Foss-Feig, C. R. Newsom, W. A. Loring, and C. J. Cascio, "White matter correlates of sensory processing in autism spectrum disorders," NeuroImage: Clinical **6**, 379–387 (2014).

[181] A. Kushki, E. Drumm, M. P. Mobarak, N. Tanel, A. Dupuis, T. Chau, and E. Anagnosou, "Investigating the autonomic nervous system response to anxiety in children with autism spectrum disorders," PLoS One **8**, e59730 (2013).

[182] A. J. Barkovich and D. Norman, "Anomalies of the corpus callosum: correlation with further anomalies of the brain," AJR **151**, 171–179 (1988).

[183] L. Lu, T. Chen, Y. Chen, M. Yuan, M. Gerstein, T. Li, H. Liang, and T. Froehlich, "Towards developing a practical artificial intelligence tool for diagnosing and evaluating autism spectrum disorder: A study using multicenter abide ii datasets." Jmir Medical Informatics (2020).

[184] H. Farooq, Y. Chen, T. T. Georgiou, A. Tannenbaum, and C. Lenglet, "Network curvature as a hallmark of brain structural connectivity," Nature communications **10**, 1–11 (2019).

[185] I. Guyon, J. Weston, S. Barnhill, and V. Vapnik, "Gene selection for cancer classification using support vector machines," Machine learning **46**, 389–422 (2002).

[186] F. Pedregosa, G. Varoquaux, A. Gramfort, V. Michel, B. Thirion, O. Grisel, M. Blondel, P. Prettenhofer, R. Weiss, V. Dubourg, J. Vanderplas, A. Passos, D. Cournapeau, M. Brucher, M. Perrot, and E. Duchesnay, "sklearn.feature_selection.rfecv¶," .

[187] A. Di Martino, D. O'connor, B. Chen, K. Alaerts, J. S. Anderson, M. Assaf, J. H. Balsters, L. Baxter, A. Beggiato, S. Bernaerts *et al.*, "Enhancing studies of the connectome in autism using the autism brain imaging data exchange ii," Scientific data **4**, 1–15 (2017).

[188] N. M. Kleinhans, G. Pauley, T. Richards, E. Neuhaus, N. Martin, N. M. Corrigan, D. W. Shaw, A. Estes, and S. R. Dager, "Age-related abnormalities in white matter microstructure in autism spectrum disorders," Brain Research **1479**, 1–16 (2012).

[189] D. B. Bashat, V. Kronfeld-Duenias, D. A. Zachor, P. M. Ekstein, T. Hendler, R. Tarrasch, A. Even, Y. Levy, and L. B. Sira, "Accelerated maturation of white matter in young children with autism: a high b value dwi study," Neuroimage **37**, 40–47 (2007).

[190] D. K. Shukla, B. Keehn, A. J. Lincoln, and R.-A. Müller, "White matter compromise of callosal and subcortical fiber tracts in children with autism spectrum disorder: a diffusion tensor imaging study," Journal of the American Academy of Child & Adolescent Psychiatry **49**, 1269–1278 (2010).

[191] B. Yamagata, T. Itahashi, M. Nakamura, M. Mimura, R.-I. Hashimoto, N. Kato, and Y. Aoki, "White matter endophenotypes and correlates for the clinical diagnosis of autism spectrum disorder," Social cognitive and affective neuroscience **13**, 765–773 (2018).

[192] A. R. Brito, M. M. Vasconcelos, R. C. Domingues, L. C. Hygino da Cruz Jr, L. d. S. Rodrigues, E. L. Gasparetto, and C. A. B. P. Calçada, "Diffusion tensor imaging findings in school-aged autistic children," Journal of Neuroimaging **19**, 337–343 (2009).

[193] L. Sivaswamy, A. Kumar, D. Rajan, M. Behen, O. Muzik, D. Chugani, and H. Chugani, "A diffusion tensor imaging study of the cerebellar pathways in children with autism spectrum disorder," Journal of child neurology **25**, 1223–1231 (2010).

[194] Y. Cheng, K.-H. Chou, I.-Y. Chen, Y.-T. Fan, J. Decety, and C.-P. Lin, "Atypical development of white matter microstructure in adolescents with autism spectrum disorders," Neuroimage **50**, 873–882 (2010).

[195] N. Barnea-Goraly, L. J. Lotspeich, and A. L. Reiss, "Similar white matter aberrations in children with autism and their unaffected siblings: a diffusion tensor imaging study using tract-based spatial statistics," Archives of general psychiatry **67**, 1052–1060 (2010).

[196] S. W. Lee, A. Lee, T. K. Choi, B. Kim, K.-S. Lee, M. Bang, and S.-H. Lee, "White matter abnormalities of the tapetum and their associations with duration of untreated psychosis and symptom severity in first-episode psychosis." Schizophrenia research **201**, 437–438 (2018).

[197] F. I. Karahanoğlu, B. Baran, Q. T. H. Nguyen, D.-E. Meskaldji, A. Yendiki, M. Vangel, S. L. Santangelo, and D. S. Manoach, "Diffusion-weighted imaging evidence of altered white matter development from late childhood to early adulthood in autism spectrum disorder," NeuroImage: Clinical **19**, 840–847 (2018).

[198] T. Itahashi, T. Yamada, M. Nakamura, H. Watanabe, B. Yamagata, D. Jimbo, S. Shioda, M. Kuroda, K. Toriizuka, N. Kato *et al.*, "Linked alterations in gray and white matter morphology in adults with high-functioning autism spectrum disorder: a multimodal brain imaging study," NeuroImage: Clinical **7**, 155–169 (2015).

[199] V. L. Cherkassky, R. K. Kana, T. A. Keller, and M. A. Just, "Functional connectivity in a baseline resting-state network in autism," Neuroreport **17**, 1687–1690 (2006).

[200] O. Dekhil, M. Ismail, A. Shalaby, A. Switala, A. Elmaghraby, R. Keynton, G. Gimel'farb, G. Barnes, and A. El-Baz, "A novel cad system for autism diagnosis using structural and functional mri," in "Biomedical Imaging (ISBI 2017)," (2017).

[201] H.-I. Suk, S.-W. Lee, D. Shen, A. D. N. Initiative et al., "Latent feature representation with stacked auto-encoder for ad/mci diagnosis," Brain Structure and Function **220**, 841–859 (2015).

[202] J. Kim, V. D. Calhoun, E. Shim, and J.-H. Lee, "Deep neural network with weight sparsity control and pre-training extracts hierarchical features and enhances classification performance: Evidence from whole-brain resting-state functional connectivity patterns of schizophrenia," Neuroimage **124**, 127–146 (2016).

[203] J. D. Rudie et al., "Altered functional and structural brain network organization in autism," NeuroImage: clinical **2**, 79–94 (2013).

[204] J. V. Hull, L. B. Dokovna, Z. J. Jacokes, C. M. Torgerson, A. Irimia, and J. D. Van Horn, "Resting-state functional connectivity in autism spectrum disorders: a review," Frontiers in psychiatry **7**, 205 (2017).

[205] Q. Zhou, L. Zhang, J. Feng, and C.-Y. Z. Lo, "Tracking the main states of dynamic functional connectivity in resting state," Frontiers in neuroscience **13**, 685 (2019).

[206] M. Filippi, E. G. Spinelli, C. Cividini, and F. Agosta, "Resting state dynamic functional connectivity in neurodegenerative conditions: a review of magnetic resonance imaging findings," Frontiers in neuroscience **13**, 657 (2019).

[207] R. Hindriks, M. H. Adhikari, Y. Murayama, M. Ganzetti, D. Mantini, N. K. Logothetis, and G. Deco, "Can sliding-window correlations reveal dynamic functional connectivity in resting-state fmri?" Neuroimage **127**, 242–256 (2016).

[208] C. Chang and G. H. Glover, "Time–frequency dynamics of resting-state brain connectivity measured with fmri," Neuroimage **50**, 81–98 (2010).

[209] M. A. Lindquist, Y. Xu, M. B. Nebel, and B. S. Caffo, "Evaluating dynamic bivariate correlations in resting-state fmri: a comparison study and a new approach," NeuroImage **101**, 531–546 (2014).

[210] C. Craddock, Y. Benhajali, C. Chu, F. Chouinard, A. Evans, A. Jakab, B. S. Khundrakpam, J. D. Lewis, Q. Li, M. Milham et al., "The neuro bureau preprocessing initiative: open sharing of preprocessed neuroimaging data and derivatives," Frontiers in Neuroinformatics **7**, 27 (2013).

[211] C. Craddock, S. Sikka, B. Cheung, R. Khanuja, S. S. Ghosh, C. Yan, Q. Li, D. Lurie, J. Vogelstein, R. Burns et al., "Towards automated analysis of connectomes: The configurable pipeline for the analysis of connectomes (c-pac)," Front Neuroinform **42**, 10–3389 (2013).

[212] Y. ElNakieb and M. Ali, "rs-fMRI-paper-code: https://github.com/ynakieb/rs-fMRI-paper," (2022).

[213] H. Chen, X. Duan, F. Liu, F. Lu, X. Ma, Y. Zhang, L. Q. Uddin, and H. Chen, "Multivariate classification of autism spectrum disorder using frequency-specific resting-state functional connectivity—a multi-center study," Progress in Neuro-Psychopharmacology and Biological Psychiatry **64**, 1–9 (2016).

[214] N. Boddaert, P. Belin, N. Chabane, J.-B. Poline, C. Barthélémy, M.-C. Mouren-Simeoni, F. Brunelle, Y. Samson, and M. Zilbovicius, "Perception of complex sounds: abnormal pattern of cortical activation in autism," American Journal of Psychiatry **160**, 2057–2060 (2003).

[215] S.-J. Blakemore, "The social brain in adolescence," Nature Reviews Neuroscience **9**, 267–277 (2008).

[216] E. T. Rolls, Y. Zhou, W. Cheng, M. Gilson, G. Deco, and J. Feng, "Effective connectivity in autism," Autism Research **13**, 32–44 (2020).

[217] T. Chen, Y. Chen, M. Yuan, M. Gerstein, T. Li, H. Liang, T. Froehlich, L. Lu *et al.*, "The development of a practical artificial intelligence tool for diagnosing and evaluating autism spectrum disorder: multicenter study," JMIR medical informatics **8**, e15767 (2020).

[218] S. Xu, M. Li, C. Yang, X. Fang, M. Ye, L. Wei, J. Liu, B. Li, Y. Gan, B. Yang *et al.*, "Altered functional connectivity in children with low-function autism spectrum disorders," Frontiers in Neuroscience **13**, 806 (2019).

[219] M. Schulte-Rüther, E. Greimel, H. J. Markowitsch, I. Kamp-Becker, H. Remschmidt, G. R. Fink, and M. Piefke, "Dysfunctions in brain networks supporting empathy: an fmri study in adults with autism spectrum disorders," Social neuroscience **6**, 1–21 (2011).

[220] S.-Y. Kim, U.-S. Choi, S.-Y. Park, S.-H. Oh, H.-W. Yoon, Y.-J. Koh, W.-Y. Im, J.-I. Park, D.-H. Song, K.-A. Cheon *et al.*, "Abnormal activation of the social brain network in children with autism spectrum disorder: an fmri study," Psychiatry investigation **12**, 37 (2015).

[221] M. Rakić, M. Cabezas, K. Kushibar, A. Oliver, and X. Lladó, "Improving the detection of autism spectrum disorder by combining structural and functional mri information," NeuroImage: Clinical **25**, 102181 (2020).

[222] Y. Wang, J. Wang, F.-X. Wu, R. Hayrat, and J. Liu, "Aimafe: Autism spectrum disorder identification with multi-atlas deep feature representation and ensemble learning," Journal of neuroscience methods **343**, 108840 (2020).

[223] F. Z. Subah, K. Deb, P. K. Dhar, and T. Koshiba, "A deep learning approach to predict autism spectrum disorder using multisite resting-state fmri," Applied Sciences **11**, 3636 (2021).

APPENDIX A: COMMONLY USED ABBREVIATIONS

ρ - Pearson correlation coefficient
AAL - automated anatomical labeling atlas
ABIDE - Autism Brain Imaging Data Exchange
ADHD - Attention deficit hyperactivity disorder
ADI-R - Autism Diagnostic Interview-Revised
ADOS - Autism Diagnostic Observation Schedule
ANOVA - Analysis of variance
ASD - Autism spectrum disorder
AUC - Area Under Curve
BOLD - blood-oxygen-level-dependent signal
CAD - Computer-Aided Diagnosis
CNN - Convolutional Neural Networks
CSF - Cerebrospinal fluid
dFC - dynamic functional connectivity
DTI - Diffusion Tensor Imaging
dwMRI | DWI - Diffusion-weighted MRI
F1 Score - Harmonic Precision-Recall Mean
FA - Fractional Anisotropy
FC - functional connectivity matrix
fMRI - Functional MRI
FS - Feature Selection
GAN - Generative Adversarial Network
GM - gray matter
GMM - Gaussian mixture model
HMMs - Hidden Markov Models
IQ - intelligence quotient
JHU - Johns Hopkins University white matter atlas
LDA - linear discriminant analysis
lr - logistic regression
lsvm - linear support vector machine
ML - Machine Learning
MLE - Maximum Likelihood Estimation
MRI - Magnetic resonance imaging
MSE - mean standard error
NDAR - National Database of Autism Research
NMR nuclear magnetic resonance
nn - neural networks
NPV - Negative Predictive Value
PCA - principal component analysis

PPV - Positive predictive value
ReLU - Rectified Linear Unit
rf - random forest
RFE - recursive feature elimination
RFE-CV - RFE with cross-validation
rs-fMRI - Resting-State functional MRI
SD - standard deviation
SGD - Stochastic Gradient Descent
sMRI - Structural MRI
SRS - Social Responsiveness Scale
TE - echo time
T-fMRI - Task-based functional MRI
TR - repetition time
TT - Talaraich and Tournoux atlas
WM - white matter

APPENDIX B: FMRI BEST MODEL SELECTED FEATURES

The following table lists all the selected features used in the best-performing model (AAl atlas, dFC feature representation, linear SVM), for reference.

Table 1. Full List of Selected dFC features

0	Precentral_L__Rolandic_Oper_R_wk
1	Precentral_L__Supp_Motor_Area_L_st
2	Precentral_L__Fusiform_L_wk
3	Precentral_L__Parietal_Inf_L_wk
4	Precentral_L__SupraMarginal_R_st
5	Precentral_L__Precuneus_R_wk
6	Precentral_L__Temporal_Sup_L_wk
7	Precentral_L__Temporal_Pole_Sup_R_wk
8	Precentral_L__Cerebelum_Crus2_R_wk
9	Precentral_R__Frontal_Inf_Tri_L_wk
10	Precentral_R__Frontal_Inf_Orb_R_wk
11	Precentral_R__Frontal_Sup_Medial_L_wk
12	Precentral_R__Insula_R_st
13	Precentral_R__Cingulum_Ant_R_wk
14	Precentral_R__Cingulum_Post_R_wk
15	Precentral_R__Calcarine_R_wk
16	Precentral_R__Fusiform_R_wk
17	Precentral_R__Caudate_L_st
18	Precentral_R__Pallidum_L_wk
19	Precentral_R__Temporal_Pole_Sup_L_st
20	Precentral_R__Temporal_Pole_Mid_R_wk
21	Precentral_R__Cerebelum_8_L_wk
22	Precentral_R__Vermis_1_2_wk
23	Frontal_Sup_L__Frontal_Mid_L_st
24	Frontal_Sup_L__Frontal_Inf_Tri_L_wk
25	Frontal_Sup_L__Frontal_Inf_Orb_L_wk
26	Frontal_Sup_L__Supp_Motor_Area_L_st
27	Frontal_Sup_L__Frontal_Sup_Medial_L_wk
28	Frontal_Sup_L__Frontal_Med_Orb_L_wk
29	Frontal_Sup_L__Frontal_Med_Orb_L_st
30	Frontal_Sup_L__Frontal_Med_Orb_R_st
31	Frontal_Sup_L__Rectus_R_wk
32	Frontal_Sup_L__Insula_R_wk
33	Frontal_Sup_L__ParaHippocampal_R_wk
34	Frontal_Sup_L__Cuneus_L_wk

Full List of Selected dFC features (continued)

index	feat_name
35	Frontal_Sup_L__Lingual_R_st
36	Frontal_Sup_L__Occipital_Sup_R_st
37	Frontal_Sup_L__Temporal_Mid_R_wk
38	Frontal_Sup_L__Temporal_Pole_Mid_L_wk
39	Frontal_Sup_L__Vermis_4_5_st
40	Frontal_Sup_R__Frontal_Mid_R_st
41	Frontal_Sup_R__Frontal_Mid_Orb_R_st
42	Frontal_Sup_R__Frontal_Inf_Oper_R_st
43	Frontal_Sup_R__Frontal_Inf_Tri_R_wk
44	Frontal_Sup_R__Frontal_Inf_Orb_R_st
45	Frontal_Sup_R__Rolandic_Oper_L_wk
46	Frontal_Sup_R__Frontal_Sup_Medial_R_st
47	Frontal_Sup_R__Frontal_Med_Orb_L_wk
48	Frontal_Sup_R__Rectus_R_wk
49	Frontal_Sup_R__Rectus_R_st
50	Frontal_Sup_R__Insula_R_st
51	Frontal_Sup_R__ParaHippocampal_L_wk
52	Frontal_Sup_R__Cuneus_L_wk
53	Frontal_Sup_R__Fusiform_R_st
54	Frontal_Sup_R__Angular_L_wk
55	Frontal_Sup_R__Angular_R_st
56	Frontal_Sup_R__Putamen_L_wk
57	Frontal_Sup_R__Temporal_Pole_Sup_L_st
58	Frontal_Sup_R__Temporal_Mid_R_st
59	Frontal_Sup_R__Cerebelum_Crus2_L_wk
60	Frontal_Sup_R__Cerebelum_Crus2_L_st
61	Frontal_Sup_Orb_L__Frontal_Mid_Orb_L_wk
62	Frontal_Sup_Orb_L__Supp_Motor_Area_L_wk
63	Frontal_Sup_Orb_L__Frontal_Sup_Medial_R_wk
64	Frontal_Sup_Orb_L__Frontal_Sup_Medial_R_st
65	Frontal_Sup_Orb_L__Cingulum_Mid_R_wk
66	Frontal_Sup_Orb_L__ParaHippocampal_R_wk
67	Frontal_Sup_Orb_L__Occipital_Mid_L_wk
68	Frontal_Sup_Orb_L__Occipital_Mid_L_st
69	Frontal_Sup_Orb_L__Temporal_Mid_L_wk
70	Frontal_Sup_Orb_L__Cerebelum_6_R_wk
71	Frontal_Sup_Orb_L__Vermis_6_wk
72	Frontal_Sup_Orb_R__Frontal_Inf_Orb_L_wk
73	Frontal_Sup_Orb_R__Olfactory_R_wk
74	Frontal_Sup_Orb_R__Rectus_L_wk
75	Frontal_Sup_Orb_R__Rectus_R_wk
76	Frontal_Sup_Orb_R__Insula_R_wk

Full List of Selected dFC features (continued)

index	feat_name
77	Frontal_Sup_Orb_R__Calcarine_R_wk
78	Frontal_Sup_Orb_R__Parietal_Inf_R_wk
79	Frontal_Sup_Orb_R__Temporal_Pole_Sup_R_wk
80	Frontal_Sup_Orb_R__Cerebelum_Crus2_L_wk
81	Frontal_Sup_Orb_R__Cerebelum_8_R_wk
82	Frontal_Mid_L__Frontal_Inf_Oper_R_wk
83	Frontal_Mid_L__Rolandic_Oper_L_wk
84	Frontal_Mid_L__Supp_Motor_Area_L_st
85	Frontal_Mid_L__Frontal_Sup_Medial_R_wk
86	Frontal_Mid_L__Cingulum_Ant_R_wk
87	Frontal_Mid_L__Amygdala_R_wk
88	Frontal_Mid_L__Occipital_Sup_L_st
89	Frontal_Mid_L__Occipital_Mid_R_wk
90	Frontal_Mid_L__Occipital_Inf_L_wk
91	Frontal_Mid_L__Parietal_Inf_R_wk
92	Frontal_Mid_L__Precuneus_L_wk
93	Frontal_Mid_L__Precuneus_L_st
94	Frontal_Mid_L__Heschl_L_wk
95	Frontal_Mid_L__Heschl_R_wk
96	Frontal_Mid_L__Temporal_Inf_R_wk
97	Frontal_Mid_R__Frontal_Inf_Oper_R_wk
98	Frontal_Mid_R__Frontal_Inf_Tri_L_wk
99	Frontal_Mid_R__Frontal_Inf_Orb_R_st
100	Frontal_Mid_R__Frontal_Sup_Medial_L_st
101	Frontal_Mid_R__Frontal_Sup_Medial_R_wk
102	Frontal_Mid_R__Frontal_Sup_Medial_R_st
103	Frontal_Mid_R__Hippocampus_L_wk
104	Frontal_Mid_R__Amygdala_R_wk
105	Frontal_Mid_R__Fusiform_L_wk
106	Frontal_Mid_R__Paracentral_Lobule_R_st
107	Frontal_Mid_R__Thalamus_R_wk
108	Frontal_Mid_R__Cerebelum_6_R_wk
109	Frontal_Mid_R__Cerebelum_8_L_wk
110	Frontal_Mid_R__Vermis_6_wk
111	Frontal_Mid_Orb_L__Frontal_Inf_Orb_L_wk
112	Frontal_Mid_Orb_L__Supp_Motor_Area_L_wk
113	Frontal_Mid_Orb_L__Frontal_Sup_Medial_L_wk
114	Frontal_Mid_Orb_L__Hippocampus_L_wk
115	Frontal_Mid_Orb_L__Cuneus_R_st
116	Frontal_Mid_Orb_L__Postcentral_L_wk
117	Frontal_Mid_Orb_L__Parietal_Inf_L_wk
118	Frontal_Mid_Orb_L__SupraMarginal_L_wk

Full List of Selected dFC features (continued)

index	feat_name
119	Frontal_Mid_Orb_L__Temporal_Pole_Mid_R_wk
120	Frontal_Mid_Orb_L__Vermis_10_wk
121	Frontal_Mid_Orb_R__Supp_Motor_Area_L_wk
122	Frontal_Mid_Orb_R__Frontal_Sup_Medial_L_wk
123	Frontal_Mid_Orb_R__Frontal_Sup_Medial_R_st
124	Frontal_Mid_Orb_R__Cingulum_Post_L_wk
125	Frontal_Mid_Orb_R__ParaHippocampal_L_wk
126	Frontal_Mid_Orb_R__ParaHippocampal_R_wk
127	Frontal_Mid_Orb_R__Occipital_Inf_R_wk
128	Frontal_Mid_Orb_R__Fusiform_L_wk
129	Frontal_Mid_Orb_R__Heschl_R_wk
130	Frontal_Mid_Orb_R__Temporal_Mid_L_st
131	Frontal_Mid_Orb_R__Vermis_3_wk
132	Frontal_Mid_Orb_R__Vermis_6_wk
133	Frontal_Inf_Oper_L__Supp_Motor_Area_L_st
134	Frontal_Inf_Oper_L__Amygdala_L_wk
135	Frontal_Inf_Oper_L__Occipital_Mid_R_wk
136	Frontal_Inf_Oper_L__Parietal_Sup_L_wk
137	Frontal_Inf_Oper_L__Thalamus_L_wk
138	Frontal_Inf_Oper_L__Heschl_L_wk
139	Frontal_Inf_Oper_L__Temporal_Sup_R_st
140	Frontal_Inf_Oper_L__Temporal_Pole_Sup_L_wk
141	Frontal_Inf_Oper_L__Cerebelum_4_5_L_wk
142	Frontal_Inf_Oper_R__Frontal_Inf_Tri_L_wk
143	Frontal_Inf_Oper_R__Frontal_Inf_Orb_R_wk
144	Frontal_Inf_Oper_R__Supp_Motor_Area_R_wk
145	Frontal_Inf_Oper_R__Cingulum_Mid_R_wk
146	Frontal_Inf_Oper_R__Hippocampus_R_wk
147	Frontal_Inf_Oper_R__Occipital_Inf_L_st
148	Frontal_Inf_Oper_R__Fusiform_R_st
149	Frontal_Inf_Oper_R__Angular_R_wk
150	Frontal_Inf_Oper_R__Pallidum_L_wk
151	Frontal_Inf_Oper_R__Pallidum_R_wk
152	Frontal_Inf_Oper_R__Temporal_Sup_L_st
153	Frontal_Inf_Oper_R__Temporal_Inf_L_wk
154	Frontal_Inf_Oper_R__Cerebelum_3_L_wk
155	Frontal_Inf_Oper_R__Vermis_6_wk
156	Frontal_Inf_Tri_L__Supp_Motor_Area_L_wk
157	Frontal_Inf_Tri_L__Frontal_Med_Orb_R_wk
158	Frontal_Inf_Tri_L__Cingulum_Ant_R_wk
159	Frontal_Inf_Tri_L__Cingulum_Ant_R_st
160	Frontal_Inf_Tri_L__Cuneus_R_wk

Full List of Selected dFC features (continued)

index	feat_name
161	Frontal_Inf_Tri_L__Occipital_Sup_R_wk
162	Frontal_Inf_Tri_L__Parietal_Inf_R_wk
163	Frontal_Inf_Tri_L__Heschl_L_wk
164	Frontal_Inf_Tri_L__Temporal_Sup_L_st
165	Frontal_Inf_Tri_L__Cerebelum_Crus1_R_wk
166	Frontal_Inf_Tri_L__Cerebelum_3_L_wk
167	Frontal_Inf_Tri_L__Cerebelum_4_5_R_wk
168	Frontal_Inf_Tri_L__Vermis_1_2_wk
169	Frontal_Inf_Tri_R__Frontal_Med_Orb_R_wk
170	Frontal_Inf_Tri_R__ParaHippocampal_R_wk
171	Frontal_Inf_Tri_R__Occipital_Inf_L_st
172	Frontal_Inf_Tri_R__Postcentral_R_wk
173	Frontal_Inf_Tri_R__SupraMarginal_R_wk
174	Frontal_Inf_Tri_R__Precuneus_R_wk
175	Frontal_Inf_Tri_R__Caudate_L_wk
176	Frontal_Inf_Tri_R__Heschl_R_wk
177	Frontal_Inf_Tri_R__Temporal_Pole_Mid_L_wk
178	Frontal_Inf_Tri_R__Cerebelum_Crus2_R_wk
179	Frontal_Inf_Tri_R__Cerebelum_4_5_L_st
180	Frontal_Inf_Tri_R__Vermis_4_5_wk
181	Frontal_Inf_Orb_L__Insula_L_wk
182	Frontal_Inf_Orb_L__Amygdala_R_wk
183	Frontal_Inf_Orb_L__Cuneus_L_wk
184	Frontal_Inf_Orb_L__Cuneus_R_wk
185	Frontal_Inf_Orb_L__Lingual_R_wk
186	Frontal_Inf_Orb_L__Occipital_Inf_L_wk
187	Frontal_Inf_Orb_L__Angular_R_wk
188	Frontal_Inf_Orb_L__Caudate_L_wk
189	Frontal_Inf_Orb_L__Heschl_L_wk
190	Frontal_Inf_Orb_L__Heschl_R_wk
191	Frontal_Inf_Orb_L__Temporal_Mid_L_wk
192	Frontal_Inf_Orb_L__Cerebelum_Crus1_L_wk
193	Frontal_Inf_Orb_L__Cerebelum_4_5_R_wk
194	Frontal_Inf_Orb_L__Vermis_1_2_wk
195	Frontal_Inf_Orb_L__Vermis_6_wk
196	Frontal_Inf_Orb_R__Supp_Motor_Area_R_wk
197	Frontal_Inf_Orb_R__Rectus_R_wk
198	Frontal_Inf_Orb_R__Cingulum_Ant_R_wk
199	Frontal_Inf_Orb_R__Fusiform_L_wk
200	Frontal_Inf_Orb_R__Parietal_Inf_L_wk
201	Frontal_Inf_Orb_R__SupraMarginal_L_wk
202	Frontal_Inf_Orb_R__Thalamus_R_wk

Full List of Selected dFC features (continued)

index	feat_name
203	Frontal_Inf_Orb_R__Temporal_Inf_L_wk
204	Frontal_Inf_Orb_R__Temporal_Inf_R_wk
205	Frontal_Inf_Orb_R__Cerebelum_3_R_wk
206	Frontal_Inf_Orb_R__Cerebelum_9_R_wk
207	Frontal_Inf_Orb_R__Vermis_8_wk
208	Rolandic_Oper_L__Rolandic_Oper_R_st
209	Rolandic_Oper_L__Olfactory_L_wk
210	Rolandic_Oper_L__Frontal_Sup_Medial_L_wk
211	Rolandic_Oper_L__Frontal_Med_Orb_R_wk
212	Rolandic_Oper_L__Hippocampus_L_wk
213	Rolandic_Oper_L__SupraMarginal_R_wk
214	Rolandic_Oper_L__Heschl_R_wk
215	Rolandic_Oper_L__Temporal_Sup_R_wk
216	Rolandic_Oper_L__Temporal_Mid_R_wk
217	Rolandic_Oper_L__Cerebelum_Crus2_L_wk
218	Rolandic_Oper_L__Cerebelum_4_5_L_st
219	Rolandic_Oper_L__Cerebelum_4_5_R_wk
220	Rolandic_Oper_L__Cerebelum_9_R_st
221	Rolandic_Oper_L__Vermis_1_2_wk
222	Rolandic_Oper_L__Vermis_7_wk
223	Rolandic_Oper_R__Olfactory_L_st
224	Rolandic_Oper_R__Frontal_Med_Orb_L_wk
225	Rolandic_Oper_R__Insula_L_wk
226	Rolandic_Oper_R__Calcarine_L_wk
227	Rolandic_Oper_R__SupraMarginal_R_wk
228	Rolandic_Oper_R__Heschl_L_wk
229	Rolandic_Oper_R__Heschl_L_st
230	Rolandic_Oper_R__Temporal_Sup_L_wk
231	Rolandic_Oper_R__Temporal_Sup_L_st
232	Rolandic_Oper_R__Temporal_Pole_Sup_R_wk
233	Rolandic_Oper_R__Temporal_Inf_L_wk
234	Rolandic_Oper_R__Cerebelum_4_5_R_wk
235	Supp_Motor_Area_L__Cingulum_Ant_L_wk
236	Supp_Motor_Area_L__Cingulum_Mid_R_wk
237	Supp_Motor_Area_L__Hippocampus_R_wk
238	Supp_Motor_Area_L__Lingual_L_wk
239	Supp_Motor_Area_L__Occipital_Sup_R_wk
240	Supp_Motor_Area_L__SupraMarginal_R_wk
241	Supp_Motor_Area_L__Angular_R_st
242	Supp_Motor_Area_L__Putamen_L_wk
243	Supp_Motor_Area_L__Temporal_Pole_Sup_L_wk
244	Supp_Motor_Area_L__Temporal_Pole_Sup_R_wk

Full List of Selected dFC features (continued)

index	feat_name
245	Supp_Motor_Area_L__Temporal_Mid_L_wk
246	Supp_Motor_Area_L__Cerebelum_8_L_wk
247	Supp_Motor_Area_L__Cerebelum_9_L_wk
248	Supp_Motor_Area_R__Olfactory_L_wk
249	Supp_Motor_Area_R__Rectus_R_wk
250	Supp_Motor_Area_R__Cingulum_Mid_L_wk
251	Supp_Motor_Area_R__Cingulum_Post_R_st
252	Supp_Motor_Area_R__Hippocampus_L_wk
253	Supp_Motor_Area_R__ParaHippocampal_R_wk
254	Supp_Motor_Area_R__Occipital_Inf_R_st
255	Supp_Motor_Area_R__Parietal_Sup_L_wk
256	Supp_Motor_Area_R__Angular_L_st
257	Supp_Motor_Area_R__Temporal_Inf_L_wk
258	Supp_Motor_Area_R__Cerebelum_4_5_L_wk
259	Supp_Motor_Area_R__Vermis_4_5_wk
260	Supp_Motor_Area_R__Vermis_9_wk
261	Olfactory_L__Olfactory_R_wk
262	Olfactory_L__Olfactory_R_st
263	Olfactory_L__Frontal_Sup_Medial_R_wk
264	Olfactory_L__Rectus_L_st
265	Olfactory_L__Insula_R_wk
266	Olfactory_L__Cingulum_Mid_L_wk
267	Olfactory_L__Hippocampus_R_wk
268	Olfactory_L__Postcentral_R_wk
269	Olfactory_L__Heschl_L_wk
270	Olfactory_L__Heschl_R_wk
271	Olfactory_L__Temporal_Sup_R_wk
272	Olfactory_L__Temporal_Pole_Mid_R_wk
273	Olfactory_L__Cerebelum_3_L_wk
274	Olfactory_L__Cerebelum_4_5_R_wk
275	Olfactory_L__Vermis_4_5_wk
276	Olfactory_R__Cingulum_Mid_L_wk
277	Olfactory_R__ParaHippocampal_R_wk
278	Olfactory_R__Cuneus_R_st
279	Olfactory_R__Occipital_Inf_R_wk
280	Olfactory_R__SupraMarginal_R_st
281	Olfactory_R__Pallidum_L_wk
282	Olfactory_R__Temporal_Mid_L_wk
283	Olfactory_R__Temporal_Mid_R_wk
284	Olfactory_R__Temporal_Inf_R_wk
285	Olfactory_R__Temporal_Inf_R_st
286	Frontal_Sup_Medial_L__Rectus_R_wk

Full List of Selected dFC features (continued)

index	feat_name
287	Frontal_Sup_Medial_L__ParaHippocampal_L_wk
288	Frontal_Sup_Medial_L__Fusiform_L_st
289	Frontal_Sup_Medial_L__Fusiform_R_wk
290	Frontal_Sup_Medial_L__Heschl_L_wk
291	Frontal_Sup_Medial_L__Temporal_Pole_Sup_R_wk
292	Frontal_Sup_Medial_L__Temporal_Pole_Sup_R_st
293	Frontal_Sup_Medial_L__Temporal_Pole_Mid_R_wk
294	Frontal_Sup_Medial_L__Cerebelum_Crus1_R_wk
295	Frontal_Sup_Medial_L__Cerebelum_Crus2_L_st
296	Frontal_Sup_Medial_L__Vermis_1_2_wk
297	Frontal_Sup_Medial_R__Rectus_R_wk
298	Frontal_Sup_Medial_R__Cingulum_Ant_R_wk
299	Frontal_Sup_Medial_R__Lingual_L_wk
300	Frontal_Sup_Medial_R__Postcentral_R_wk
301	Frontal_Sup_Medial_R__SupraMarginal_L_wk
302	Frontal_Sup_Medial_R__SupraMarginal_R_wk
303	Frontal_Sup_Medial_R__Precuneus_R_wk
304	Frontal_Sup_Medial_R__Heschl_L_wk
305	Frontal_Sup_Medial_R__Temporal_Sup_R_wk
306	Frontal_Sup_Medial_R__Temporal_Mid_R_st
307	Frontal_Sup_Medial_R__Cerebelum_Crus1_R_wk
308	Frontal_Sup_Medial_R__Cerebelum_Crus2_R_st
309	Frontal_Sup_Medial_R__Cerebelum_3_R_wk
310	Frontal_Sup_Medial_R__Vermis_6_wk
311	Frontal_Med_Orb_L__Cingulum_Post_R_wk
312	Frontal_Med_Orb_L__ParaHippocampal_R_wk
313	Frontal_Med_Orb_L__Amygdala_L_wk
314	Frontal_Med_Orb_L__Lingual_R_st
315	Frontal_Med_Orb_L__Occipital_Sup_L_wk
316	Frontal_Med_Orb_L__Parietal_Sup_L_wk
317	Frontal_Med_Orb_L__Parietal_Sup_L_st
318	Frontal_Med_Orb_L__Heschl_R_wk
319	Frontal_Med_Orb_L__Temporal_Sup_L_wk
320	Frontal_Med_Orb_L__Temporal_Pole_Mid_R_wk
321	Frontal_Med_Orb_L__Cerebelum_3_R_wk
322	Frontal_Med_Orb_L__Vermis_10_wk
323	Frontal_Med_Orb_R__Cingulum_Post_L_wk
324	Frontal_Med_Orb_R__Hippocampus_R_wk
325	Frontal_Med_Orb_R__Amygdala_R_wk
326	Frontal_Med_Orb_R__Postcentral_R_wk
327	Frontal_Med_Orb_R__Parietal_Sup_R_wk
328	Frontal_Med_Orb_R__Parietal_Inf_R_wk

Full List of Selected dFC features (continued)

index	feat_name
329	Frontal_Med_Orb_R__Precuneus_R_st
330	Frontal_Med_Orb_R__Paracentral_Lobule_R_wk
331	Frontal_Med_Orb_R__Temporal_Sup_L_wk
332	Frontal_Med_Orb_R__Temporal_Pole_Mid_R_wk
333	Frontal_Med_Orb_R__Cerebelum_9_L_wk
334	Rectus_L__Cingulum_Post_L_wk
335	Rectus_L__Calcarine_L_wk
336	Rectus_L__Occipital_Sup_R_st
337	Rectus_L__Parietal_Inf_R_wk
338	Rectus_L__Angular_R_wk
339	Rectus_L__Temporal_Pole_Mid_R_wk
340	Rectus_L__Temporal_Inf_L_wk
341	Rectus_R__Hippocampus_L_wk
342	Rectus_R__Occipital_Mid_R_wk
343	Rectus_R__Parietal_Inf_R_wk
344	Rectus_R__SupraMarginal_L_wk
345	Rectus_R__SupraMarginal_R_wk
346	Rectus_R__Cerebelum_6_L_wk
347	Rectus_R__Vermis_4_5_wk
348	Rectus_R__Vermis_10_wk
349	Insula_L__Cingulum_Ant_L_wk
350	Insula_L__Cingulum_Post_R_wk
351	Insula_L__ParaHippocampal_L_wk
352	Insula_L__Cuneus_L_wk
353	Insula_L__Lingual_L_wk
354	Insula_L__Postcentral_R_wk
355	Insula_L__SupraMarginal_L_wk
356	Insula_L__SupraMarginal_R_wk
357	Insula_L__SupraMarginal_R_st
358	Insula_L__Precuneus_R_wk
359	Insula_L__Precuneus_R_st
360	Insula_L__Paracentral_Lobule_L_wk
361	Insula_L__Pallidum_R_wk
362	Insula_L__Temporal_Sup_R_wk
363	Insula_L__Temporal_Pole_Mid_L_wk
364	Insula_L__Cerebelum_4_5_R_wk
365	Insula_R__Cingulum_Post_L_st
366	Insula_R__Occipital_Sup_R_wk
367	Insula_R__Occipital_Inf_R_wk
368	Insula_R__Postcentral_L_wk
369	Insula_R__Angular_L_wk
370	Insula_R__Precuneus_L_st

Full List of Selected dFC features (continued)

index	feat_name
371	Insula_R__Caudate_L_wk
372	Insula_R__Temporal_Mid_L_wk
373	Insula_R__Temporal_Inf_L_st
374	Insula_R__Cerebelum_6_L_wk
375	Insula_R__Cerebelum_6_R_wk
376	Insula_R__Vermis_3_wk
377	Insula_R__Vermis_7_wk
378	Insula_R__Vermis_8_wk
379	Cingulum_Ant_L__Cingulum_Ant_R_st
380	Cingulum_Ant_L__Cingulum_Mid_R_wk
381	Cingulum_Ant_L__Lingual_L_wk
382	Cingulum_Ant_L__Occipital_Inf_L_wk
383	Cingulum_Ant_L__Occipital_Inf_L_st
384	Cingulum_Ant_L__Occipital_Inf_R_wk
385	Cingulum_Ant_L__Thalamus_L_wk
386	Cingulum_Ant_L__Temporal_Sup_L_wk
387	Cingulum_Ant_L__Temporal_Inf_L_st
388	Cingulum_Ant_L__Cerebelum_4_5_L_wk
389	Cingulum_Ant_L__Vermis_4_5_wk
390	Cingulum_Ant_R__Cingulum_Mid_R_st
391	Cingulum_Ant_R__Calcarine_R_wk
392	Cingulum_Ant_R__Cuneus_L_wk
393	Cingulum_Ant_R__Fusiform_R_wk
394	Cingulum_Ant_R__SupraMarginal_L_wk
395	Cingulum_Ant_R__Thalamus_R_wk
396	Cingulum_Ant_R__Temporal_Mid_R_wk
397	Cingulum_Ant_R__Cerebelum_Crus2_R_wk
398	Cingulum_Ant_R__Cerebelum_3_R_wk
399	Cingulum_Ant_R__Cerebelum_4_5_L_wk
400	Cingulum_Ant_R__Cerebelum_6_R_wk
401	Cingulum_Ant_R__Vermis_3_wk
402	Cingulum_Ant_R__Vermis_6_wk
403	Cingulum_Ant_R__Vermis_8_wk
404	Cingulum_Mid_L__Hippocampus_R_wk
405	Cingulum_Mid_L__Cuneus_R_wk
406	Cingulum_Mid_L__Occipital_Sup_L_wk
407	Cingulum_Mid_L__Occipital_Mid_R_wk
408	Cingulum_Mid_L__Fusiform_R_wk
409	Cingulum_Mid_L__Parietal_Inf_R_wk
410	Cingulum_Mid_L__Pallidum_R_wk
411	Cingulum_Mid_L__Heschl_L_wk
412	Cingulum_Mid_L__Temporal_Sup_L_wk

Full List of Selected dFC features (continued)

index	feat_name
413	Cingulum_Mid_L__Cerebelum_3_R_wk
414	Cingulum_Mid_R__Cingulum_Post_R_wk
415	Cingulum_Mid_R__Hippocampus_L_wk
416	Cingulum_Mid_R__ParaHippocampal_L_wk
417	Cingulum_Mid_R__Occipital_Inf_R_wk
418	Cingulum_Mid_R__Postcentral_L_wk
419	Cingulum_Mid_R__Precuneus_L_wk
420	Cingulum_Mid_R__Putamen_L_wk
421	Cingulum_Mid_R__Cerebelum_10_L_st
422	Cingulum_Mid_R__Vermis_6_wk
423	Cingulum_Mid_R__Vermis_10_wk
424	Cingulum_Post_L__ParaHippocampal_L_wk
425	Cingulum_Post_L__Amygdala_L_wk
426	Cingulum_Post_L__Calcarine_L_wk
427	Cingulum_Post_L__Lingual_R_wk
428	Cingulum_Post_L__Occipital_Sup_L_wk
429	Cingulum_Post_L__SupraMarginal_R_wk
430	Cingulum_Post_L__Angular_R_wk
431	Cingulum_Post_L__Paracentral_Lobule_L_wk
432	Cingulum_Post_L__Temporal_Sup_L_wk
433	Cingulum_Post_L__Temporal_Pole_Sup_R_wk
434	Cingulum_Post_L__Cerebelum_10_R_wk
435	Cingulum_Post_L__Vermis_3_wk
436	Cingulum_Post_R__Postcentral_L_st
437	Cingulum_Post_R__Parietal_Sup_L_wk
438	Cingulum_Post_R__SupraMarginal_R_wk
439	Cingulum_Post_R__Thalamus_R_wk
440	Cingulum_Post_R__Cerebelum_3_L_wk
441	Cingulum_Post_R__Cerebelum_3_R_st
442	Cingulum_Post_R__Cerebelum_9_L_wk
443	Cingulum_Post_R__Vermis_3_wk
444	Cingulum_Post_R__Vermis_4_5_wk
445	Hippocampus_L__Hippocampus_R_st
446	Hippocampus_L__Fusiform_L_wk
447	Hippocampus_L__Postcentral_R_wk
448	Hippocampus_L__SupraMarginal_L_wk
449	Hippocampus_L__Angular_R_wk
450	Hippocampus_L__Thalamus_R_wk
451	Hippocampus_L__Heschl_L_wk
452	Hippocampus_L__Temporal_Pole_Mid_L_wk
453	Hippocampus_L__Cerebelum_Crus1_R_wk
454	Hippocampus_L__Cerebelum_3_L_wk

Full List of Selected dFC features (continued)

index	feat_name
455	Hippocampus_L__Cerebelum_4_5_L_st
456	Hippocampus_L__Cerebelum_6_R_wk
457	Hippocampus_L__Cerebelum_8_R_wk
458	Hippocampus_R__Cuneus_L_wk
459	Hippocampus_R__Fusiform_L_st
460	Hippocampus_R__SupraMarginal_R_wk
461	Hippocampus_R__Angular_L_wk
462	Hippocampus_R__Angular_R_wk
463	Hippocampus_R__Paracentral_Lobule_R_wk
464	Hippocampus_R__Temporal_Sup_R_wk
465	Hippocampus_R__Temporal_Pole_Sup_L_st
466	Hippocampus_R__Temporal_Pole_Sup_R_wk
467	Hippocampus_R__Temporal_Mid_L_wk
468	Hippocampus_R__Temporal_Pole_Mid_R_wk
469	Hippocampus_R__Cerebelum_4_5_L_wk
470	Hippocampus_R__Cerebelum_7b_R_st
471	Hippocampus_R__Cerebelum_8_R_wk
472	Hippocampus_R__Cerebelum_9_L_wk
473	ParaHippocampal_L__Lingual_R_wk
474	ParaHippocampal_L__Occipital_Mid_L_wk
475	ParaHippocampal_L__Parietal_Sup_R_wk
476	ParaHippocampal_L__Angular_R_wk
477	ParaHippocampal_L__Precuneus_R_wk
478	ParaHippocampal_L__Paracentral_Lobule_L_wk
479	ParaHippocampal_L__Paracentral_Lobule_R_wk
480	ParaHippocampal_L__Putamen_L_wk
481	ParaHippocampal_L__Temporal_Sup_L_wk
482	ParaHippocampal_L__Temporal_Pole_Sup_R_wk
483	ParaHippocampal_L__Temporal_Pole_Mid_L_wk
484	ParaHippocampal_L__Temporal_Inf_L_wk
485	ParaHippocampal_L__Cerebelum_4_5_L_wk
486	ParaHippocampal_L__Vermis_6_wk
487	ParaHippocampal_R__Amygdala_R_wk
488	ParaHippocampal_R__Amygdala_R_st
489	ParaHippocampal_R__Cuneus_R_wk
490	ParaHippocampal_R__Occipital_Mid_L_wk
491	ParaHippocampal_R__Temporal_Pole_Sup_R_wk
492	ParaHippocampal_R__Cerebelum_Crus1_L_wk
493	ParaHippocampal_R__Cerebelum_3_L_wk
494	ParaHippocampal_R__Cerebelum_4_5_R_wk
495	ParaHippocampal_R__Cerebelum_6_R_wk
496	ParaHippocampal_R__Vermis_6_wk

Full List of Selected dFC features (continued)

index	feat_name
497	Amygdala_L__Occipital_Sup_L_st
498	Amygdala_L__Fusiform_L_wk
499	Amygdala_L__Parietal_Inf_L_wk
500	Amygdala_L__Temporal_Mid_R_wk
501	Amygdala_L__Cerebelum_Crus2_R_wk
502	Amygdala_L__Vermis_3_wk
503	Amygdala_R__SupraMarginal_R_wk
504	Amygdala_R__Caudate_L_wk
505	Amygdala_R__Putamen_R_wk
506	Amygdala_R__Cerebelum_Crus1_L_wk
507	Amygdala_R__Cerebelum_Crus1_R_wk
508	Amygdala_R__Cerebelum_Crus2_R_wk
509	Amygdala_R__Cerebelum_3_L_st
510	Amygdala_R__Vermis_9_wk
511	Calcarine_L__Cuneus_L_st
512	Calcarine_L__Occipital_Sup_R_st
513	Calcarine_L__Occipital_Mid_R_st
514	Calcarine_L__Parietal_Sup_R_st
515	Calcarine_L__Caudate_R_wk
516	Calcarine_L__Pallidum_L_wk
517	Calcarine_L__Vermis_7_wk
518	Calcarine_L__Vermis_8_wk
519	Calcarine_R__Cuneus_L_wk
520	Calcarine_R__Cuneus_R_wk
521	Calcarine_R__Cuneus_R_st
522	Calcarine_R__Occipital_Sup_R_wk
523	Calcarine_R__Occipital_Mid_R_wk
524	Calcarine_R__Postcentral_L_wk
525	Calcarine_R__Parietal_Inf_R_wk
526	Calcarine_R__Thalamus_L_wk
527	Calcarine_R__Cerebelum_Crus2_L_wk
528	Calcarine_R__Vermis_3_wk
529	Cuneus_L__Lingual_R_wk
530	Cuneus_L__Occipital_Mid_R_wk
531	Cuneus_L__Postcentral_L_wk
532	Cuneus_L__Precuneus_R_wk
533	Cuneus_L__Paracentral_Lobule_L_wk
534	Cuneus_L__Pallidum_R_wk
535	Cuneus_L__Temporal_Pole_Sup_L_wk
536	Cuneus_L__Temporal_Mid_R_wk
537	Cuneus_L__Temporal_Inf_R_st
538	Cuneus_L__Cerebelum_4_5_R_wk

Full List of Selected dFC features (continued)

index	feat_name
539	Cuneus_L__Vermis_1_2_wk
540	Cuneus_R__Occipital_Sup_R_wk
541	Cuneus_R__Postcentral_L_wk
542	Cuneus_R__Postcentral_R_wk
543	Cuneus_R__Caudate_R_wk
544	Cuneus_R__Putamen_L_wk
545	Cuneus_R__Temporal_Pole_Sup_L_wk
546	Cuneus_R__Temporal_Mid_R_wk
547	Cuneus_R__Cerebelum_6_R_st
548	Cuneus_R__Cerebelum_8_L_wk
549	Cuneus_R__Cerebelum_9_L_wk
550	Cuneus_R__Cerebelum_10_R_wk
551	Lingual_L__Postcentral_L_st
552	Lingual_L__Heschl_L_wk
553	Lingual_L__Vermis_7_wk
554	Lingual_R__Thalamus_R_wk
555	Lingual_R__Vermis_3_st
556	Occipital_Sup_L__Paracentral_Lobule_L_wk
557	Occipital_Sup_L__Temporal_Mid_R_wk
558	Occipital_Sup_L__Cerebelum_8_L_wk
559	Occipital_Sup_L__Cerebelum_9_R_wk
560	Occipital_Sup_L__Vermis_3_wk
561	Occipital_Sup_R__Postcentral_R_wk
562	Occipital_Sup_R__Pallidum_L_wk
563	Occipital_Sup_R__Pallidum_R_wk
564	Occipital_Sup_R__Temporal_Pole_Sup_L_wk
565	Occipital_Sup_R__Temporal_Pole_Sup_R_wk
566	Occipital_Sup_R__Temporal_Inf_R_wk
567	Occipital_Sup_R__Vermis_7_wk
568	Occipital_Mid_L__Occipital_Mid_R_st
569	Occipital_Mid_L__Parietal_Inf_R_st
570	Occipital_Mid_L__Precuneus_L_wk
571	Occipital_Mid_L__Caudate_R_wk
572	Occipital_Mid_L__Temporal_Pole_Mid_L_wk
573	Occipital_Mid_L__Cerebelum_4_5_L_wk
574	Occipital_Mid_L__Vermis_10_wk
575	Occipital_Mid_R__Occipital_Inf_R_wk
576	Occipital_Mid_R__Fusiform_L_wk
577	Occipital_Mid_R__Postcentral_R_wk
578	Occipital_Mid_R__Precuneus_L_wk
579	Occipital_Mid_R__Temporal_Sup_L_wk
580	Occipital_Mid_R__Temporal_Mid_R_wk

Full List of Selected dFC features (continued)

index	feat_name
581	Occipital_Mid_R__Temporal_Inf_R_st
582	Occipital_Mid_R__Cerebelum_6_L_wk
583	Occipital_Mid_R__Vermis_6_wk
584	Occipital_Inf_L__Postcentral_L_wk
585	Occipital_Inf_L__Postcentral_L_st
586	Occipital_Inf_L__Postcentral_R_wk
587	Occipital_Inf_L__Precuneus_L_st
588	Occipital_Inf_L__Precuneus_R_st
589	Occipital_Inf_L__Pallidum_L_wk
590	Occipital_Inf_L__Temporal_Pole_Sup_R_wk
591	Occipital_Inf_L__Temporal_Pole_Sup_R_st
592	Occipital_Inf_L__Cerebelum_Crus2_L_wk
593	Occipital_Inf_L__Cerebelum_3_R_wk
594	Occipital_Inf_L__Cerebelum_4_5_L_st
595	Occipital_Inf_L__Cerebelum_9_R_wk
596	Occipital_Inf_R__Precuneus_R_wk
597	Occipital_Inf_R__Thalamus_L_wk
598	Occipital_Inf_R__Thalamus_R_wk
599	Occipital_Inf_R__Cerebelum_9_L_wk
600	Occipital_Inf_R__Vermis_3_wk
601	Occipital_Inf_R__Vermis_6_wk
602	Fusiform_L__Parietal_Sup_R_wk
603	Fusiform_L__Precuneus_L_st
604	Fusiform_L__Temporal_Pole_Mid_R_wk
605	Fusiform_L__Temporal_Inf_L_st
606	Fusiform_L__Cerebelum_3_R_st
607	Fusiform_L__Cerebelum_8_R_wk
608	Fusiform_L__Vermis_10_wk
609	Fusiform_R__SupraMarginal_R_wk
610	Fusiform_R__Precuneus_L_wk
611	Fusiform_R__Precuneus_R_wk
612	Fusiform_R__Temporal_Mid_L_wk
613	Fusiform_R__Temporal_Pole_Mid_R_wk
614	Fusiform_R__Cerebelum_6_L_wk
615	Postcentral_L__Postcentral_R_st
616	Postcentral_L__Parietal_Sup_R_wk
617	Postcentral_L__Angular_R_st
618	Postcentral_L__Paracentral_Lobule_R_wk
619	Postcentral_L__Thalamus_R_wk
620	Postcentral_L__Heschl_R_wk
621	Postcentral_L__Temporal_Inf_R_st
622	Postcentral_L__Cerebelum_Crus1_L_wk

Full List of Selected dFC features (continued)

index	feat_name
623	Postcentral_L__Cerebelum_4_5_R_st
624	Postcentral_L__Vermis_4_5_wk
625	Postcentral_R__Parietal_Sup_L_wk
626	Postcentral_R__Angular_L_wk
627	Postcentral_R__Angular_R_wk
628	Postcentral_R__Paracentral_Lobule_L_st
629	Postcentral_R__Putamen_L_wk
630	Postcentral_R__Temporal_Sup_L_st
631	Postcentral_R__Temporal_Sup_R_wk
632	Postcentral_R__Temporal_Mid_R_wk
633	Postcentral_R__Temporal_Pole_Mid_L_wk
634	Postcentral_R__Cerebelum_Crus1_L_wk
635	Postcentral_R__Cerebelum_Crus2_L_st
636	Postcentral_R__Cerebelum_3_R_st
637	Parietal_Sup_L__Angular_R_st
638	Parietal_Sup_L__Temporal_Mid_L_wk
639	Parietal_Sup_L__Temporal_Pole_Mid_L_wk
640	Parietal_Sup_L__Temporal_Inf_L_wk
641	Parietal_Sup_L__Cerebelum_6_R_wk
642	Parietal_Sup_L__Cerebelum_8_R_wk
643	Parietal_Sup_L__Vermis_7_wk
644	Parietal_Sup_L__Vermis_9_wk
645	Parietal_Sup_R__SupraMarginal_L_wk
646	Parietal_Sup_R__SupraMarginal_L_st
647	Parietal_Sup_R__Pallidum_R_wk
648	Parietal_Sup_R__Cerebelum_4_5_L_wk
649	Parietal_Sup_R__Vermis_6_wk
650	Parietal_Inf_L__Parietal_Inf_R_wk
651	Parietal_Inf_L__Precuneus_R_wk
652	Parietal_Inf_L__Heschl_L_wk
653	Parietal_Inf_L__Temporal_Sup_L_wk
654	Parietal_Inf_L__Temporal_Pole_Mid_L_wk
655	Parietal_Inf_R__Angular_L_wk
656	Parietal_Inf_R__Heschl_L_wk
657	Parietal_Inf_R__Heschl_R_wk
658	Parietal_Inf_R__Temporal_Sup_L_wk
659	Parietal_Inf_R__Temporal_Sup_R_wk
660	Parietal_Inf_R__Cerebelum_Crus1_L_wk
661	Parietal_Inf_R__Cerebelum_Crus1_R_wk
662	Parietal_Inf_R__Cerebelum_Crus2_L_st
663	Parietal_Inf_R__Cerebelum_4_5_L_wk
664	Parietal_Inf_R__Cerebelum_6_R_wk

Full List of Selected dFC features (continued)

index	feat_name
665	SupraMarginal_L__Angular_L_wk
666	SupraMarginal_L__Precuneus_R_wk
667	SupraMarginal_L__Pallidum_L_wk
668	SupraMarginal_L__Heschl_R_wk
669	SupraMarginal_L__Heschl_R_st
670	SupraMarginal_L__Temporal_Mid_R_wk
671	SupraMarginal_L__Temporal_Pole_Mid_L_st
672	SupraMarginal_L__Temporal_Pole_Mid_R_wk
673	SupraMarginal_R__Putamen_L_st
674	SupraMarginal_R__Pallidum_L_wk
675	SupraMarginal_R__Pallidum_L_st
676	SupraMarginal_R__Temporal_Sup_L_wk
677	SupraMarginal_R__Temporal_Sup_L_st
678	SupraMarginal_R__Cerebelum_Crus1_R_wk
679	Angular_L__Precuneus_R_st
680	Angular_L__Caudate_L_wk
681	Angular_L__Putamen_L_wk
682	Angular_L__Temporal_Pole_Sup_L_wk
683	Angular_L__Temporal_Mid_L_wk
684	Angular_L__Cerebelum_3_L_wk
685	Angular_L__Cerebelum_6_L_wk
686	Angular_L__Vermis_4_5_wk
687	Angular_R__Precuneus_L_wk
688	Angular_R__Precuneus_R_st
689	Angular_R__Heschl_R_wk
690	Angular_R__Temporal_Pole_Mid_L_wk
691	Angular_R__Temporal_Pole_Mid_L_st
692	Angular_R__Temporal_Inf_R_wk
693	Angular_R__Cerebelum_Crus1_R_wk
694	Angular_R__Cerebelum_3_R_wk
695	Angular_R__Vermis_3_wk
696	Precuneus_L__Thalamus_L_wk
697	Precuneus_L__Heschl_R_wk
698	Precuneus_L__Temporal_Pole_Mid_L_wk
699	Precuneus_L__Cerebelum_3_R_wk
700	Precuneus_L__Vermis_1_2_wk
701	Precuneus_L__Vermis_4_5_wk
702	Precuneus_R__Putamen_L_wk
703	Precuneus_R__Pallidum_L_st
704	Precuneus_R__Temporal_Mid_R_wk
705	Precuneus_R__Temporal_Pole_Mid_L_wk
706	Precuneus_R__Cerebelum_4_5_L_st

Full List of Selected dFC features (continued)

index	feat_name
707	Precuneus_R__Vermis_4_5_wk
708	Precuneus_R__Vermis_4_5_st
709	Paracentral_Lobule_L__Paracentral_Lobule_R_wk
710	Paracentral_Lobule_L__Paracentral_Lobule_R_st
711	Paracentral_Lobule_L__Temporal_Pole_Sup_L_wk
712	Paracentral_Lobule_L__Cerebelum_Crus2_R_wk
713	Paracentral_Lobule_L__Cerebelum_8_L_wk
714	Paracentral_Lobule_L__Cerebelum_10_R_wk
715	Paracentral_Lobule_L__Vermis_4_5_wk
716	Paracentral_Lobule_R__Cerebelum_10_R_wk
717	Paracentral_Lobule_R__Cerebelum_10_R_st
718	Paracentral_Lobule_R__Vermis_4_5_wk
719	Caudate_L__Pallidum_L_wk
720	Caudate_L__Thalamus_R_wk
721	Caudate_L__Heschl_L_wk
722	Caudate_L__Cerebelum_9_R_wk
723	Caudate_L__Vermis_9_wk
724	Caudate_R__Pallidum_L_wk
725	Caudate_R__Temporal_Inf_R_wk
726	Caudate_R__Cerebelum_6_R_wk
727	Caudate_R__Cerebelum_9_L_wk
728	Putamen_L__Pallidum_R_wk
729	Putamen_L__Temporal_Inf_L_wk
730	Putamen_L__Cerebelum_Crus1_R_wk
731	Putamen_L__Cerebelum_6_R_wk
732	Putamen_L__Vermis_4_5_wk
733	Putamen_L__Vermis_10_wk
734	Putamen_R__Cerebelum_Crus1_L_wk
735	Putamen_R__Cerebelum_7b_L_wk
736	Pallidum_L__Heschl_R_wk
737	Pallidum_L__Temporal_Inf_R_wk
738	Pallidum_L__Cerebelum_9_R_wk
739	Pallidum_L__Vermis_1_2_wk
740	Pallidum_L__Vermis_8_wk
741	Pallidum_R__Thalamus_L_wk
742	Pallidum_R__Temporal_Mid_L_wk
743	Pallidum_R__Cerebelum_4_5_L_wk
744	Pallidum_R__Cerebelum_6_L_wk
745	Pallidum_R__Cerebelum_9_R_wk
746	Thalamus_L__Thalamus_R_wk
747	Thalamus_L__Thalamus_R_st
748	Thalamus_L__Temporal_Mid_R_wk

index	feat_name
749	Thalamus_L__Cerebelum_3_R_wk
750	Thalamus_L__Cerebelum_6_R_wk
751	Thalamus_L__Vermis_7_wk
752	Thalamus_R__Temporal_Inf_L_wk
753	Thalamus_R__Cerebelum_Crus1_R_wk
754	Thalamus_R__Cerebelum_6_L_wk
755	Thalamus_R__Vermis_1_2_st
756	Thalamus_R__Vermis_6_wk
757	Heschl_L__Cerebelum_8_L_wk
758	Heschl_R__Temporal_Pole_Mid_L_wk
759	Heschl_R__Cerebelum_Crus2_L_wk
760	Heschl_R__Cerebelum_3_R_wk
761	Heschl_R__Vermis_7_wk
762	Heschl_R__Vermis_10_wk
763	Temporal_Sup_L__Temporal_Sup_R_st
764	Temporal_Sup_L__Cerebelum_Crus1_L_wk
765	Temporal_Sup_L__Cerebelum_Crus1_R_wk
766	Temporal_Sup_L__Cerebelum_Crus2_R_wk
767	Temporal_Sup_L__Cerebelum_8_L_wk
768	Temporal_Sup_L__Vermis_4_5_wk
769	Temporal_Sup_L__Vermis_10_wk
770	Temporal_Sup_R__Cerebelum_4_5_R_wk
771	Temporal_Sup_R__Vermis_3_wk
772	Temporal_Sup_R__Vermis_9_wk
773	Temporal_Sup_R__Vermis_10_wk
774	Temporal_Pole_Sup_L__Cerebelum_Crus2_L_wk
775	Temporal_Pole_Sup_L__Cerebelum_4_5_R_wk
776	Temporal_Pole_Sup_R__Cerebelum_3_R_wk
777	Temporal_Pole_Sup_R__Cerebelum_4_5_L_wk
778	Temporal_Mid_L__Temporal_Pole_Mid_R_wk
779	Temporal_Mid_L__Cerebelum_Crus1_L_wk
780	Temporal_Mid_L__Cerebelum_6_L_wk
781	Temporal_Mid_L__Cerebelum_6_R_wk
782	Temporal_Mid_L__Cerebelum_8_L_wk
783	Temporal_Mid_L__Vermis_4_5_wk
784	Temporal_Mid_L__Vermis_7_wk
785	Temporal_Mid_R__Cerebelum_Crus1_L_wk
786	Temporal_Mid_R__Cerebelum_9_L_wk
787	Temporal_Pole_Mid_L__Temporal_Inf_L_wk
788	Temporal_Pole_Mid_R__Cerebelum_9_L_wk
789	Temporal_Pole_Mid_R__Vermis_3_wk
790	Temporal_Inf_L__Cerebelum_Crus1_R_wk

Full List of Selected dFC features (continued)

index	feat_name
791	Temporal_Inf_L__Cerebelum_7b_L_st
792	Temporal_Inf_L__Vermis_7_wk
793	Temporal_Inf_R__Cerebelum_7b_R_wk
794	Temporal_Inf_R__Cerebelum_8_R_wk
795	Temporal_Inf_R__Vermis_3_wk
796	Cerebelum_Crus1_L__Cerebelum_Crus1_R_wk
797	Cerebelum_Crus1_L__Cerebelum_Crus1_R_st
798	Cerebelum_Crus1_L__Cerebelum_4_5_R_st
799	Cerebelum_Crus1_L__Cerebelum_8_L_st
800	Cerebelum_Crus1_L__Cerebelum_8_R_st
801	Cerebelum_Crus1_L__Vermis_4_5_st
802	Cerebelum_Crus1_R__Cerebelum_Crus2_L_wk
803	Cerebelum_Crus1_R__Vermis_9_wk
804	Cerebelum_Crus2_L__Cerebelum_6_R_wk
805	Cerebelum_Crus2_L__Cerebelum_9_R_wk
806	Cerebelum_Crus2_L__Vermis_4_5_wk
807	Cerebelum_3_L__Cerebelum_4_5_R_st
808	Cerebelum_3_L__Vermis_3_wk
809	Cerebelum_3_R__Cerebelum_6_R_wk
810	Cerebelum_3_R__Cerebelum_8_R_wk
811	Cerebelum_3_R__Cerebelum_10_L_st
812	Cerebelum_3_R__Vermis_4_5_wk
813	Cerebelum_4_5_L__Cerebelum_8_R_wk
814	Cerebelum_4_5_L__Cerebelum_9_R_wk
815	Cerebelum_4_5_L__Vermis_10_wk
816	Cerebelum_6_L__Cerebelum_9_R_wk
817	Cerebelum_6_L__Vermis_1_2_wk
818	Cerebelum_6_R__Cerebelum_8_L_wk
819	Cerebelum_6_R__Cerebelum_9_L_wk
820	Cerebelum_6_R__Vermis_6_st
821	Cerebelum_6_R__Vermis_7_wk
822	Cerebelum_7b_L__Cerebelum_8_R_st
823	Cerebelum_8_L__Cerebelum_10_R_st
824	Cerebelum_8_L__Vermis_6_wk
825	Cerebelum_8_L__Vermis_9_wk
826	Cerebelum_8_L__Vermis_10_wk
827	Cerebelum_8_R__Cerebelum_10_L_wk
828	Cerebelum_8_R__Cerebelum_10_R_wk
829	Cerebelum_8_R__Vermis_7_wk
830	Cerebelum_8_R__Vermis_8_st
831	Cerebelum_8_R__Vermis_9_st
832	Cerebelum_9_L__Vermis_4_5_wk

Full List of Selected dFC features (continued)

index	feat_name
833	Cerebelum_9_L__Vermis_9_st
834	Cerebelum_9_L__Vermis_10_wk
835	Cerebelum_9_R__Vermis_9_wk
836	Cerebelum_10_L__Cerebelum_10_R_st
837	Cerebelum_10_R__Vermis_10_wk
838	Vermis_1_2__Vermis_3_st
839	Vermis_7__Vermis_9_wk

APPENDIX C: PERMISSIONS

- Article Title: Computer aided autism diagnosis using diffusion tensor imaging
  Journal: IEEE Access
  Volume: 8
  Pages: 191298–191308
  Year: 2020
  Publisher: IEEE
  Copyright: In reference to IEEE copyrighted material which is used with permission in this dissertation, the IEEE does not endorse any of University of Louisville's products or services. Internal or personal use of this material is permitted. If interested in reprinting/republishing IEEE copyrighted material for advertising or promotional purposes or for creating new collective works for resale or redistribution, please go to `http://www.ieee.org/publications_standards/publications/rights/rights_link.html` to learn how to obtain a License from RightsLink. If applicable, University Microfilms and/or Pro-Quest Library, or the Archives of Canada may supply single copies of the dissertation.

- Article Title: The Role of Diffusion Tensor MR Imaging (DTI) of the Brain in Diagnosing Autism Spectrum Disorder: Promising Results
  Journal: Sensors
  Volume: 21
  Pages: 8171
  Year: 2021
  Publisher: MDPI
  Copyright: No special permission is required to reuse all or part of article published by MDPI, including figures and tables. For articles published under an open access Creative Common CC BY license, any part of the article may be reused without permission provided that the original article is clearly cited. MDPI does not hold the copyright or the right to re-license the published material. The original copyright holder (usually the original publisher or authors), whether or not this material can be re-used.

CURRICULUM VITAE

Yaser Abdelrahman ElNakieb

Personal Information

E-mail: yasernakib@gmail.com
LinkedIn: https://www.linkedin.com/in/yaser-elnakieb/
GoogleScholar: https://scholar.google.com/citations?user=JYsmmx8AAAAJ

Education

Ph.D., BioEngineering, University of Louisville, Louisville, KY, Dec 2022

Post-Grad Courses, ECE, Virginia Polytechnic Institute and State University, Blacksburg, VA, May 2016

B.Sc., ECE, Mansoura University, Mansoura, Egypt, Aug 2011

Professional and Work Experience

Graduate Research Assistant in the University of Louisville, Jan2018-present (Part-Time)

Graduate Research Assistant in ZewailCity of Science and Technology, Feb2017–Oct2017 (Part-Time)

Research Assistant in SmartCI / VT-MENA, Aug2013-May2016 (Part-Time)

Systems Engineer in Ministry of Communications and Information Technology, Apr2013-Sep2017 (Part-Time)

Research Assistant in Wireless Intelligent Network Center –Nile University, Oct2011-Jan2013

Honors and Awards

- Best Graduate Student Peer-Reviewed Journal Paper from the School of Interdisciplinary and Graduate Studies, University of Louisville, 2022.

- Best Doctoral Journal Article Award from the School of Interdisciplinary and Graduate Studies, University of Louisville, 2021.

- Degree of Honor of Cumulative Academic Distinction, Mansoura University, 2011.

Publications and Presentations

Google Scholar ORCiD LOOP ResearchGate

1. "*Predicting the Level of Respiratory Support in COVID-19 Patients Using Machine Learning.*", Co-author, Bioengineering 9.10 (2022): 536.

2. "*Understanding the Role of Connectivity Dynamics of Resting-State Functional MRI in the Diagnosis of Autism Spectrum Disorder: A Comprehensive Study*", First author, submitted to Bioengineering (2022).

3. "*The Role of Structure MRI in Diagnosing Autism.*", **Equal Contribution**, Diagnostics 12.1 (2022): 165.

4. "*The Role of Diffusion Tensor MR Imaging (DTI) of the Brain in Diagnosing Autism Spectrum Disorder: Promising Results.*", First author, Sensors 2021, 21, 8171. https://doi.org/10.3390/s21248171.

5. "*Identifying brain pathological abnormalities of autism for classification using diffusion tensor imaging.*", Book Chapter, Neural Engineering Techniques for Autism Spectrum Disorder. Academic Press, 2021. 361-376.

6. "*Autism Classification Using SMRI: A Recursive Features Selection Based on Sampling from Multi-Level High Dimensional Spaces.*", Co-author, 2021 IEEE 18th International Symposium on Biomedical Imaging (ISBI).

7. "*A Personalized Autism Diagnosis CAD System Using a Fusion of Structural MRI and Resting-State Functional MRI Data.*", Co-author, Frontiers in psychiatry 10 (2021): 392.

8. "*Computer Aided Autism Diagnosis Using Diffusion Tensor Imaging.*", First author, IEEE Access 8 (2020), doi: 10.1109/ACCESS.2020.3032066.

9. "*A Comprehensive Framework for Differentiating Autism Spectrum Disorder from Neurotypicals by Fusing Structural MRI and Resting State Functional MRI.*", Co-author, Seminars in Pediatric Neurology, 2020.

10. "*Autism Spectrum Disorder Diagnosis framework using Diffusion Tensor Imaging.*", First author, 2019 IEEE International Conference on Imaging Systems and Techniques (IST).

11. "*Towards Accurate Personalized Autism Diagnosis Using different Imaging Modalities: sMRI, fMRI, and DTI.*", Co-author, IEEE International Symposium on Signal Processing and Information Technology (ISSPIT 2018).

12. "*Towards Personalized Autism Diagnosis: Promising Results.*", Co-author, IEEE Conference on Computer Vision and Pattern Recognition, (ICPR 2018).

13. "*CRC: Collaborative Research and Teaching Testbed for Wireless Communications and Networks.*", Co-author, 10th ACM international workshop on Wireless network testbeds, experimental evaluation and characterization. (WiNTECH 2016).

14. "*Genetic Algorithm-based Mapper to support Multiple Concurrent Users on Wireless Testbeds.*", First author, 2016 IEEE Wireless Communications and Networking Conference (WCNC 2016).

15. "*Proactive Scheduling for Content Pre-fetching in Mobile Networks.*", Co-author, (ICC2014) IEEE International Conference on Communications, June 2014.

16. *Ten abstracts accepted*, INSAR2022, four at INSAR2020, BMES2021, BMES2020, BMES2019, BMES2018, and NRSC 2016.

Extra-Curricular Activities and Memberships

- +**21** Verified Peer Reviews in many conferences and journals, see Web of Science.

- Three Udacity NanoDegrees in Data Science:
  Professional Data Analysis (2021), Advanced Data Analysis (2021), Machine Learning Cross-Skilling (2022).

- BMES (Biomedical Engineering Society) member.

- IEEE (Institute of Electrical and Electronics Engineers) member.

- EMBS (IEEE Engineering in Medicine and Biology Society) member.

- American Association for the Advancement of Science member.

- Society for Neuroscience Louisville chapter member.

- *TPC member* at European Conference on Networks and Communications Eu-CNC 2016.

- *TPC member* at European Conference on Networks and Communications Eu-CNC 2017.

- *Session chair* at IEEE Wireless Communications and Networking Conference WCNC 2016.